LBL-31071

Lawrence Berkeley Laboratory
UNIVERSITY OF CALIFORNIA

EARTH SCIENCES DIVISION

To be published as a chapter in *Heat and Mass Transport in Fractured Rocks,*
J. Bear, G. DeMarsily, and C.F. Tsang, Eds., Academic Press,
San Diego, CA, 1992

Unsaturated Flow in Fractured, Porous Media

J.S.Y. Wang and T.N. Narasimhan

July 1991

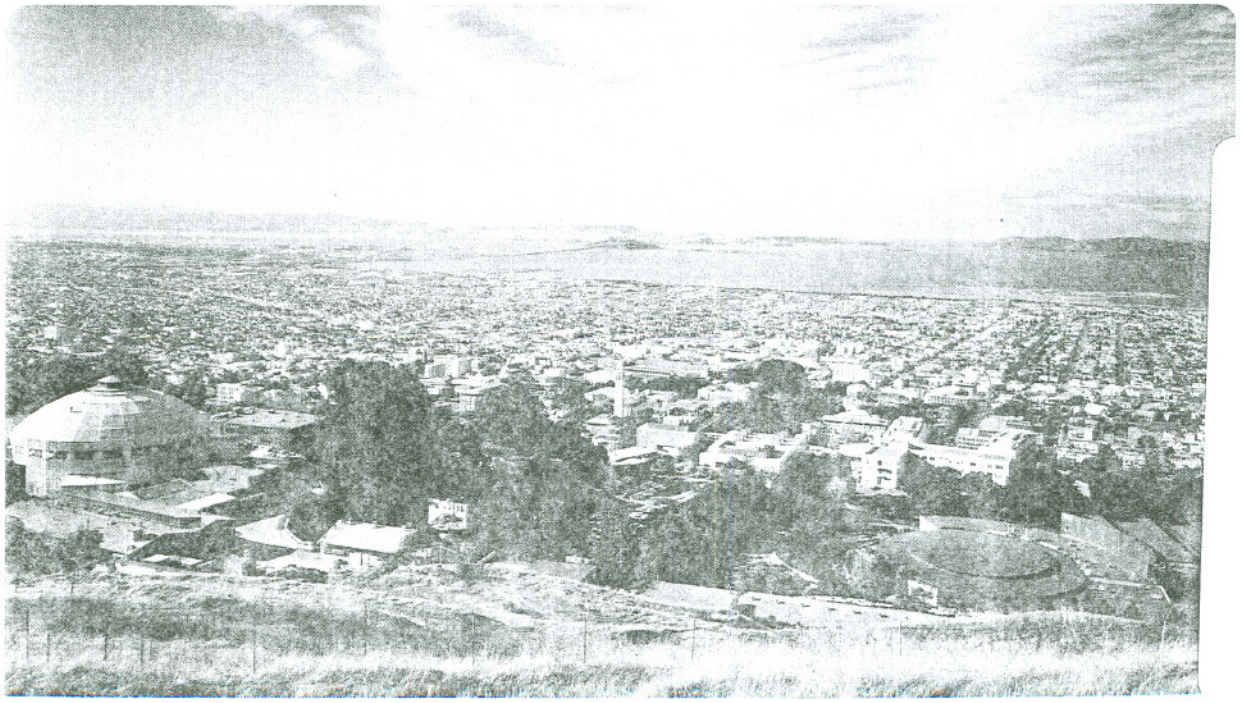

| LOAN COPY |
|Circulates |
|for 4 weeks| Bldg. 50 Library
LBL-31071
Copy 2

Prepared for the U.S. Department of Energy under Contract Number DE-AC03-76SF00098

DISCLAIMER

This document was prepared as an account of work sponsored by the United States Government. Neither the United States Government nor any agency thereof, nor The Regents of the University of California, nor any of their employees, makes any warranty, express or implied, or assumes any legal liability or responsibility for the accuracy, completeness, or usefulness of any information, apparatus, product, or process disclosed, or represents that its use would not infringe privately owned rights. Reference herein to any specific commercial product, process, or service by its trade name, trademark, manufacturer, or otherwise, does not necessarily constitute or imply its endorsement, recommendation, or favoring by the United States Government or any agency thereof, or The Regents of the University of California. The views and opinions of authors expressed herein do not necessarily state or reflect those of the United States Government or any agency thereof or The Regents of the University of California and shall not be used for advertising or product endorsement purposes.

Lawrence Berkeley Laboratory is an equal opportunity employer.

LBL-31071

Unsaturated Flow in Fractured, Porous Media

Joseph S. Y. Wang and T. N. Narasimhan

Earth Sciences Division
Lawrence Berkeley Laboratory
University of California
Berkeley, California 94720

July 1991

This work was supported by the Yucca Mountain Site Characterization Project, Sandia National Laboratories, under Document SNL 75-4347, through U.S. Department of Energy Contract DE-AC03-76SF00098.

Chapter for "Heat and Mass Transport in Fractured Rocks", edited by J. Bear, G. deMarsily, and C. F. Tsang, Academic Press.

UNSATURATED FLOW IN FRACTURED, POROUS MEDIA

Joseph S. Y. Wang and T. N. Narasimhan
Earth Sciences Division
Lawrence Berkeley Laboratory
University of California
Berkeley, California 94720

Abstract

Unsaturated flow through fractured tuff rock is one of the important hydrological issues in the assessment and characterization of the Yucca Mountain hydrologic system as a site for a high-level nuclear waste repository. This chapter reviews the major findings, motivation and rationale that have dictated the evolution of our Yucca Mountain studies between 1983 and 1989, and discusses the key issues remain to be resolved. In brief, the important inferences drawn from the conceptual analysis are as follow:

- Under ambient conditions, moisture movement in the unsaturated zone at Yucca Mountain is dominated by the tuff matrix.
- Hydrological parameters of fracture, such as permeability, saturation, and effective surface area, can be related to the surface roughness and aperture variation of fracture.
- Because of the dominance of capillary forces in the extremely fine pores, strong infiltration pulses tend to be damped out by near-surface welded and nonwelded units.
- If the Ghost Dance Fault at Yucca Mountain is assumed to be made up of highly permeable open fractures and hence is treatable as a seepage face, then the small eastward tilt of the stratigraphic units (approximately 6°) is not sufficient to greatly enhance lateral flow over vertical flow.
- Hydrological parameters, such as permeability and air entry pressure, are mutually correlated at least in a crude way and hence judicious constraints will have to be placed in choosing parameters for modeling exercises.
- Rough-walled fractures can be quantified using fractal theory and parameters of fractal theory can be advantageously related to parameters of geostatistics.

Table of Contents

Abstract i
List of Subject Indices iv
List of Figures vii
List of Tables ix
List of Abbreviations x
List of Symbols xi

1.0 Introduction 1
2.0 Conceptual Model for Moisture Movement in Fractured, Porous Tuff: *Fracture Flow vs. Matrix Flow* 4
2.1 Capillary Mechanism: *Preferential Saturation of Fine Pores* 4
2.2 Natural Fracture Model: *Importance of Wall Roughness* 5
2.3 Aperture Distribution: *Approach to Quantify a Rough Fracture* 6
2.4 Flow Across Fractures: *Importance of Effective Fracture Area* 11
2.5 Transport Properties of Fractured Tuff: *Contrast between Fracture and Matrix Characteristics* 13
3.0 Drainage Responses of a Fractured Tuff Column: *Dynamic Interaction between Discrete Fractures and Porous Matrix* 16
3.1 Fracture Description: *Adaptation of Field Data* 18
3.2 Discrete Fracture-Porous Matrix Model: *Nested Matrix Elements* 20
3.3 Tool of Analysis: *The TRUST Code* 20
3.4 Major Findings: *Flow Dominance by Matrix* 21
3.5 A Useful Corollary: *The Composite Model* 26
4.0 Vertical Infiltration through Welded-Nonwelded Units: *Maintenance of Unsaturated State* 27
4.1 Fracture and Matrix Data and Model: *Observational Basis* 27
4.2 Estimate of Ambient Infiltration Rate: *Observational Constraints* 28
4.3 Welded-Nonwelded Flow Interaction: *Effect of a Thick Unit on Thin Units* 32
4.4 Approximate Model for Steady-State Profiles: *Elementary Path Integration* 33
4.5 Response to Extreme Infiltration Pulses: *Damping by Near-Surface Units* 33
4.6 Ambient Infiltration: *An Estimate* 41
5.0 Distribution of Fluid Near a Fault Zone: *Possibility of Lateral Flow* 41

5.1 Unsaturated Fault: *Different Hydrological Possibilities* 41
5.2 How to Model the Fault: *The Seepage Face Idealization* 43
5.3 Stratigraphy, Fracture, Matrix Data: *An Update* 43
5.4 The Ghost Dance Fault: *A Column Profile* 44
5.5 Multi-Column Models: *Fluid Redistribution within the Tuff Formation* 49
5.6 Vertical and Lateral Flow: *Nonwelded Unit as Lateral Channel for Fluid Redistribution* 52
5.7 Onset of Seepage Flow: *A Hypothetical Nearly-Saturated System* 52
5.8 Ambient Flow Field: *Effect of Stratigraphic Tilting* 54
6.0 Statistical Analyses of Tuff and Soil Data: *Variability of Hydrological Parameters in Different Media* 55
6.1 Parameter Distributions: *Difference between Tight Tuff Matrix and Permeable Soil* 55
6.2 Parameter Correlations: *Relationship between Hydrological Parameters and Flow Geometry* 58
6.3 Fracture and Fault Parameters: *Physical Constraint* 62
6.4 Fractal Theory: *Spatial Correlations and Scaling of Rough-Walled Fractures* 64
7.0 Review and Summary

Acknowledgements 72
References 73

List of Subject Indices

Index	Section	Paragraph	Page
air entry radius	6.1	3	56
	6.2	2	58
air entry scaling factor	6.1	3	56
	6.3	3	64
ambient (matrix) saturation	3.4	1	21
	4.2	3	28
	4.2	4	32
	4.3	1	32
	5.4	1	44
aperture distribution function	2.3	1	9
	2.3	5	10
capillary equation	2.1	2	4
	6.1	3	56
capillary force/capillarity	2.1	1	4
	4.5	4	36
	4.5	5	36
	5.0	1	41
	5.1	1	41
	5.1	4	42
	5.1	5	42
	5.1	6	42
	5.2	1	43
	5.2	2	43
capillary limit/maximum capillary size	2.1	3	5
	4.5	2	34
composite medium model	3.0	1	16
	3.5	1	26
	4.5	8	39
contact area	2.2	2	6
	2.3	5	10
	2.4	1	11
	3.3	1	21
	3.4	4	22
contact cutoff aperture	2.3	5	10
discrete fracture-porous matrix model	3.2	1	20
	3.5	2	26
	4.5	1	34
effective (fracture-matrix) flow area	2.3	1	9
	2.4	2	13
	3.3	1	20
	3.4	4	22
	3.4	7	24

Index	Section	Paragraph	Page
effective medium model	3.0	1	18
	3.5	1	26
fault flow	5.0	1	41
	5.1	2	42
	5.1	6	43
fractal	6.4	1	64
	6.4	2	64
	6.4	4	67
fracture characteristic curve	2.3	6	10
	2.5	1	13
	6.3	1	62
fracture coating	2.4	1	11
	4.1	1	27
fracture continuum permeability	3.1	2	18
fracture flow	2.5	2	16
	3.4	4	22
	4.2	4	32
	4.5	9	39
	5.7	1	54
fracture-matrix interflow	3.2	1	20
	3.4	5	24
fracture-matrix pressure equilibrium	3.4	3	22
	3.5	1	26
fracture permeability	2.5	2	16
	3.3	1	21
fracture relative permeability	2.3	1	9
fracture saturation	2.3	1	9
	2.5	1	13
	3.4	4	22
fracture spacing	3.1	1	18
	4.1	1	27
gamma distribution function	2.3	4	10
infiltration	4.0	1	27
	4.2	1	28
	4.2	3	28
	4.5	2	34
	4.6	1	41
lateral flow	4.5	10	39
	5.0	1	41
	5.6	3	52
matrix characteristic curve	2.5	1	13
	4.3	1	32
	5.3	2	44
matrix flow	2.5	2	16
	3.4	4	22
matrix permeability	2.5	2	16

Index	Section	Paragraph	Page
matrix saturation	2.5	1	13
	4.5	5	36
	5.5	2	49
matrix-to-matrix flow	2.2	2	6
nested element	3.2	1	20
parameter correlation	6.0	1	55
	6.2	1	58
	6.3	3	62
parameter distribution	6.1	1	55
	6.4	3	64
path integration	3.3	2	21
	4.4	1	33
phase-constriction factor	2.3	2	9
	2.5	2	16
	3.4	3	22
pore-size distribution	4.3	1	32
	5.3	2	44
	6.1	3	56
pulse infiltration	4.5	3	34
	4.5	7	36
rough fracture	2.2	2	6
	6.4	1	64
saturation cutoff aperture	2.3	1	6
seepage boundary/flow	5.2	1	43
	5.7	1	54
spatial correlation	6.4	1	64
	6.4	3	67
travel time	2.2	1	6
	2.5	2	16
	4.0	1	27
	5.3	1	44
	5.6	1	52
	6.4	5	67
unsaturated zone	1.0	1	1
Yucca Mountain	1.0	1	1
	3.1	1	18
	5.0	1	41

List of Figures

		Page
Figure 1.1	Location map of the Yucca Mountain site, Nevada for a potential high-level nuclear waste repository.	2
Figure 1.2	Evolution of performance assessment task.	3
Figure 2.1	Schematic representation of water flow in a fractured porous medium.	7
Figure 2.2	Schematic plan view of a fracture plane showing asperities (solid circles), liquid water (gray) and air (blank).	8
Figure 2.3	Aperture distributions for the Topopah Spring welded tuff unit (distribution parameter: vertical fracture - $\beta_v = 10.4\ mm^{-1}$; horizontal fracture - $\beta_h = 8.04\ mm^{-1}$).	12
Figure 2.4	Effective flow area versus pressure head for flow across the fracture plane.	14
Figure 2.5	Saturation characteristic curves of fractures and tuff matrix.	15
Figure 2.6	Permeabilities of partially saturated fractures and tuff matrix.	17
Figure 3.1	Schematic representation of three fracture sets for the Topopah Spring welded tuff unit.	19
Figure 3.2	Unsaturated drainage in a tuff column: comparison of pressure changes for three different conceptualizations.	23
Figure 3.3	Unsaturated drainage in a tuff column: patterns of darcy velocities (sign convention: horizontal fracture - flow into fracture is positive; vertical fracture - upward is positive).	25
Figure 4.1	Nonuniform grids used for one-dimensional simulations.	29
Figure 4.2	Saturation profiles for 0.1-mm/yr steady-state infiltration.	30
Figure 4.3	Saturation profile for 0.5-mm/yr steady-state infiltration.	31
Figure 4.4	Three dimensional mesh used for studying column response to extreme infiltration pulses.	35

Figure 4.5	Horizontal saturation profiles within matrix block of Tiva Canyon welded tuff unit.	37
Figure 4.6	Saturation profiles for the first cycle of 500-*yr* × 0.1-*mm/yr* transient infiltration.	38
Figure 4.7	Response to 5,000-*yr* infiltration pulse: damping of fluxes within the Paintbrush nonwelded tuff unit.	40
Figure 5.1	Idealized cross section of Yucca Mountain.	45
Figure 5.2	Saturation profiles for 0.1-*mm/yr* steady-state infiltration for fine and coarse meshes at Ghost Dance Fault.	46
Figure 5.3	Two-dimensional grid for vertical and lateral flow model.	50
Figure 5.4	Potential distribution in a 645-*m* section west of Ghost Dance Fault.	51
Figure 5.5	Darcy velocity profiles for vertical and lateral flows with a 0.1-*mm/yr* steady-state infiltration.	53
Figure 6.1	Comparison of characteristic curve of the van Genuchten model and the Brooks-Corey model.	57
Figure 6.2	Distribution of air-entry scaling factor for natural soils and tuff matrix.	59
Figure 6.3	Distribution of saturated hydraulic conductivity for natural soils and tuff matrix.	60
Figure 6.4	Correlation between saturated hydraulic conductivity and air-entry scaling factor for natural soils and tuff matrix.	61
Figure 6.5	Correlation between saturated hydraulic conductivity and air-entry scaling factor for tuff fracture and fault models.	63
Figure 6.6	Steps involved in generating a rough fracture with fractal dimensions.	65
Figure 6.7	Representation of rough fractures with fractal surfaces.	66
Figure 6.8	Relation between variograms and fractal dimensions.	68
Figure 7.1	Framework of fundamental questions in performance assessment.	71

List of Tables

		Page
Table 2.1	Fracture Characteristic Curves	11
Table 5.1	Matrix Properties	47
Table 5.2	Fracture Properties	48

List of Abbreviations

Abbreviation	Expansion
BFw	Bullfrog welded tuff unit
CFUn	Crater Flat upper nonwelded tuff unit
CHnv	Calico Hill nonwelded, vitric tuff unit
CHnz	Calico Hill nonwelded, zeolitic tuff unit
DOE	United States Department of Energy
GDF	Ghost Dance Fault
HLW	High Level Nuclear Wastes
PPw	Pah Pass welded tuff unit
PTn	Paintbrush nonwelded tuff unit
RIB	Reference Information Base
SC	Solitario Canyon
SCP	Site Characterization Plan
SNL	Sandia National Laboratories
TCw	Tiva Canyon welded tuff unit
TSw	Topopah Spring welded tuff unit
USGS	United States Geological Survey
YMP	Yucca Mountain Site Characterization Project

List of Symbols

b	aperture	$[L]$
d	fracture spacing	$[L]$
D	fractal dimension	
$f(b)$	aperture distribution function	$[L^{-1}]$
g	gravitational constant	$[Lt^{-2}]$
h	pressure head	$[L]$
k	permeability	$[L^2]$
K	hydraulic conductivity	$[Lt^{-1}]$
L	fracture width	$[L^2]$
n	van Genuchten's parameter	
q	flow rate	$[Lt^{-1}]$
r	radius	$[L]$
S	saturation	
V	volume	$[L^3]$
W	width of flow channel	$[L]$
z	elevation	$[L]$
α	air entry scaling factor	$[L^{-1}]$
β	gamma distribution parameter	$[L^{-1}]$
γ	surface tension	$[Mt^{-2}]$
λ	pore-size distribution index	
ω	contact area fraction	
ϕ	porosity	
ρ	density	$[ML^{-3}]$
σ	effective flow area	
τ	phase-constriction factor	
θ	contact angle	

Subscript:

ae	air entry value
c	contact

e	effective value
f	fracture
h	horizontal
m	matrix
max	maximum value
r	relative or residual value
S	condition with saturation S
v	vertical
0	zero stress or zero elevation
1	condition with saturation $S = 1$

1.0 Introduction

That the thick unsaturated zone in the arid southwestern United States could be potentially suitable for the disposal of high-level radioactive waste (HLW) was originally suggested by Winograd (1981) of the United States Geological Survey (USGS). The Yucca Mountain site, on and adjacent to the Nevada Test Site in southern Nevada (Fig. 1.1), was initially considered as a potential site for HLW disposal on the basis of host rock conditions below the water table. Later, as knowledge of the mountain grew, it was recognized that not only will the unsaturated zone itself provide an excellent host for the wastes but that the repository will derive the benefits of both the unsaturated zone and the saturated zone. Accordingly, several scientists of the USGS jointly suggested in February 1982 to the U. S. Department of Energy (DOE) that the unsaturated zone at Yucca Mountain should potentially be a desirable site for HLW disposal. By 1982, the Yucca Mountain concept gradually passed the first phase of a broad preliminary assessment to the next phase of testing some of the ideas with more detailed analysis. This was also the time when the authors got actively involved with the Sandia National Laboratories' (SNL) hydrological performance assessment activities in the Yucca Mountain Site Characterization Project (YMP), administered by the Nevada Operation Office, DOE. The thoughts regarding the Yucca Mountain, as they emerged from the first phase of analysis, were summarized in Roseboom (1983) and Montazer and Wilson (1984). In December 1987, the U. S. Congress chose Yucca Mountain as the site for characterization as part of the program to provide the first HLW repository. A Site Characterization Plan for Yucca Mountain was published by DOE (1989).

Thus far the focus of our unsaturated flow study with SNL has been on understanding the mechanisms and on modeling the hydrological processes in partially saturated, fractured, porous tuff at Yucca Mountain. We started with a spatial resolution in the submillimeter range for the discrete fractures and extended consideration to kilometer scale for an east-west crosssection of Yucca Mountain. The time scale of interest ranged from minutes for the desaturation of fractures to thousands of years for infiltration through the partially saturated zones. The objective of performance assessment of the hydrological processes at Yucca Mountain is to predict the three-dimensional responses of the whole system from the repository to the accessible environment over thousands of years. Starting with the small scale, this study has gradually evolved to the large scale which is of ultimate interest for performance assessment. The broad pattern of this evolution can be summarized as shown in Fig. 1.2. After the sections on unsaturated flow processes in different scales, we discuss the parameter variations and correlations of tuff properties and

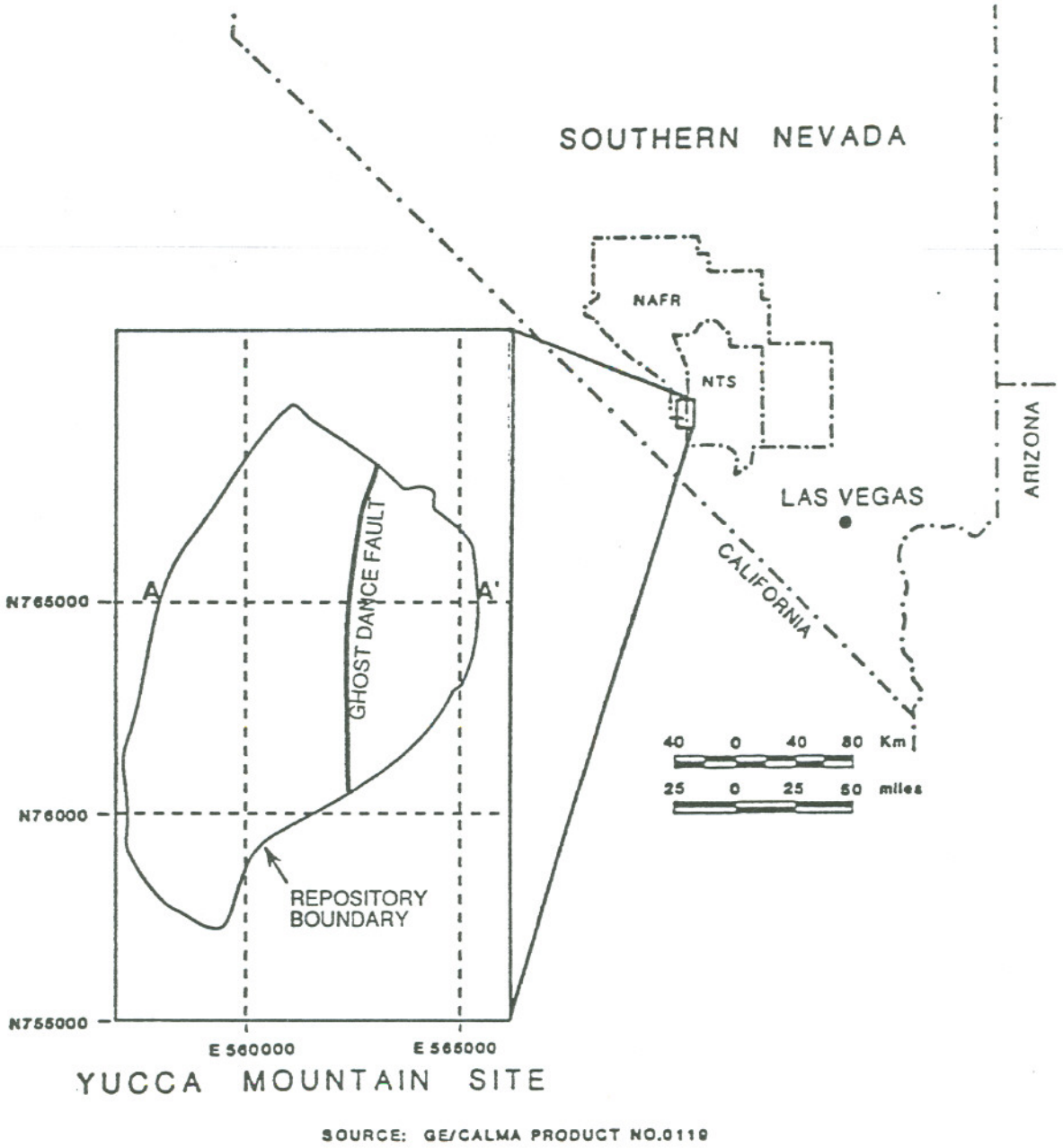

Figure 1.1 Location map of the Yucca Mountain site, Nevada for a potential high-level nuclear waste repository.

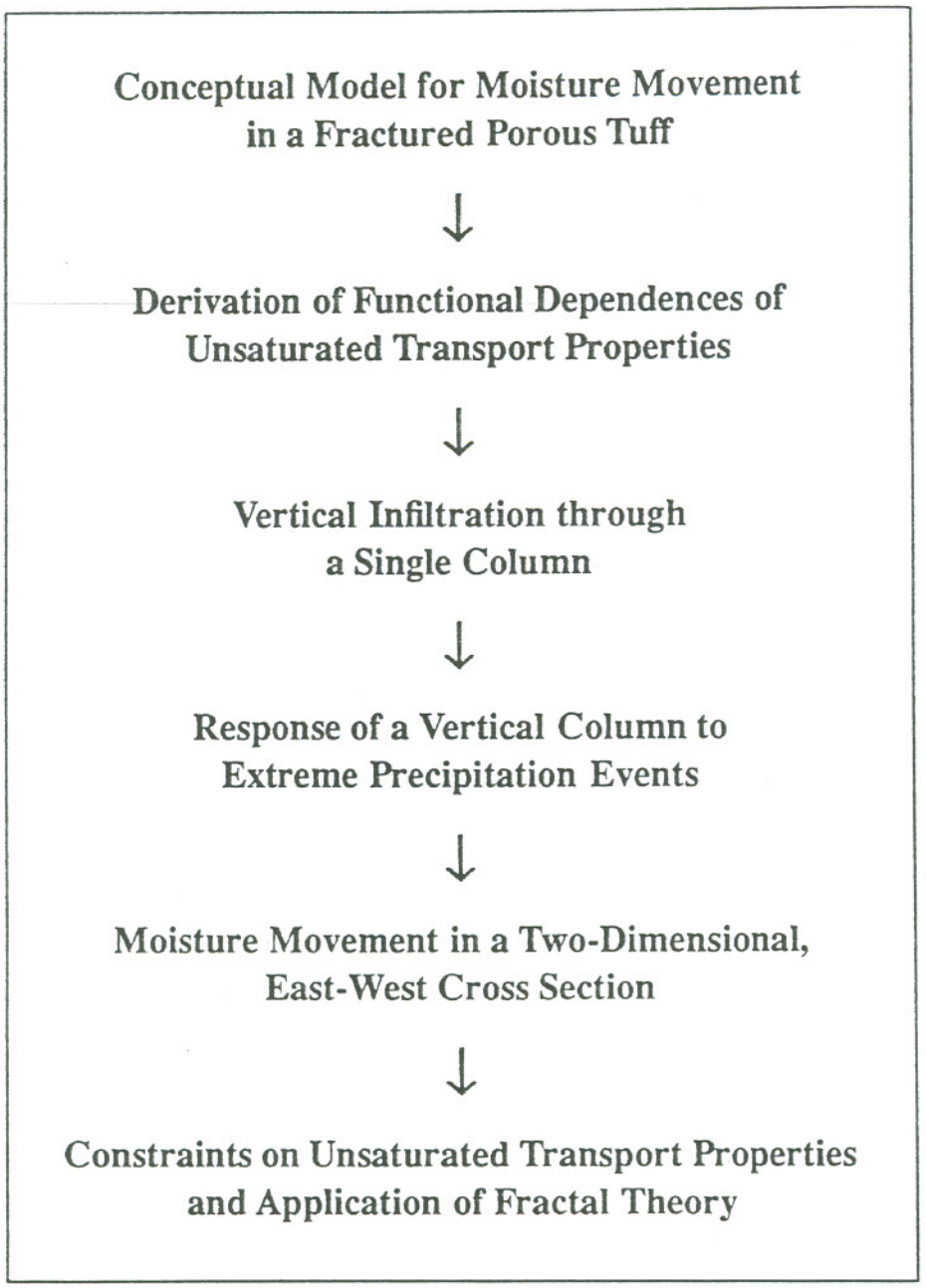

Figure 1.2 Evolution of performance assessment task.

the potential use of fractal geometry for future modeling studies. The chapter concludes with a brief discussion on general hydrological issues beyond our conceptual analysis of unsaturated flow in fractured, porous tuff (Narasimhan and Wang, 1991).

2.0 Conceptual Model for Moisture Movemnent in Fractured, Porous Tuff: *Fracture Flow vs. Matrix Flow*

During 1983, the first year, we focused on the development of a conceptual model to understand the hydrological mechanisms governing fluid flow in a partially saturated, fractured porous medium. The Topopah Spring welded tuff formation, the candidate host rock for the repository at Yucca Mountain, is highly fractured with tuff matrix blocks of sub-meter sizes surrounded by discrete fractures. The main question we addressed was whether water moves in the fractures or in the matrix under partially saturated conditions. This is one of the most important hydrological questions in determining the flow pattern and travel time through fractured, porous units. This single question will remain as one of the key issues to be resolved and quantified throughout the course of YMP investigations.

2.1 Capillary Mechanism: *Preferential Saturation of Fine Pores*

We recognize from the onset of this study that fractures with large apertures will drain relatively easily and water is likely to remain in the matrix. This intuition stems from the knowledge that large pores can not sustain large capillary suction forces. In a heterogeneous system where sand and clay coexist, the sand with large pores can be easily drained and the clay will remain wetter than the sand under partially saturated conditions. This can be readily explained by the nature of the capillary mechanism. When we insert a capillary tube into a beaker of water, the height of water rise along the capillary tube is inversely proportional to the radius of the tube. A dry towel with fine texture can soak up more water than a rag with coarse pores. With capillary theory, we anticipate that the larger pores will desaturate more easily than smaller pores. If this simple capillary model is valid, we can easily infer that fractures in a fractured porous medium will tend to remain dry under partially saturated conditions and the liquid water is held by capillarity in the finer pores of the matrix.

The well-known capillary equation for a tube with height of water rise $|h|$ and radius r,

$$|h| = \frac{2\,\gamma\, cos\,(\theta)}{r\,\rho g}, \tag{2.1}$$

is also applicable to a parallel-plate fracture with aperture b replacing the radius r. The surface tension γ is the surface energy per unit area, or equivalently, surface force per unit length. For a pair of parallel plate with width L much greater than the aperture b, the upward force component along two liquid-air-solid interfaces with contact angle θ is $\gamma \cos(\theta) \times (2L)$, and the downward weight of the liquid rise is $\rho g \times (Lb|h|)$. From force balance, we obtain the capillary equation relating the capillary rise $|h|$ with fracture aperture b.

Before we describe the response of fractured tuff with capillary theory, we must point out that the capillary mechanism has a limited range of validity. If the fracture aperture or capillary radius is large, the radius of curvature of the meniscus will be infinite and the capillary effect will be negligible. For a wetting fluid with contact angle $\theta = 0$, the hemispherical surface at top of the rise can no longer be defined when b or r is greater than the height $|h|$. Therefore the maximum capillary size (with $b = |h|$ or $r = |h|$ in Eq. 2.1) is

$$b_{\max} = r_{\max} = \left[\frac{2\gamma}{\rho g}\right]^{1/2} . \tag{2.2}$$

For $\gamma = 0.072\ kg/sec^2$, density $\rho = 1000\ kg/m^3$, and gravitational acceleration $g = 9.8\ m/sec^2$, the maximum capillary size is $3.83\ mm$. For fractures tens to hundreds of meters below the ground surface, we expect that a majority of fractures will be closed under over burden stress and have apertures less than this maximum capillary size. For fracture aperture and macropore radius greater than this size, a capillary-based conceptual model is not valid.

In capillary theory, we also ignore the small fraction of water molecules adsorbed by the solid wall above the meniscus. The slow movement of adsorbed water outside the liquid region may be important in extremely dry conditions. The capillary limit and adsorptive mechanism are two hydrological issues which may be important for studying the validity of capillarity-based conceptual model.

2.2 Natural Fracture Model: *Importance of Wall Roughness*

In quantifying the capillary mechanism in fractured tuff, we recognize that the parallel-plate model frequently used in saturated fracture flow studies is too crude and simplistic to represent natural fractures under partially saturated conditions. In a highly fractured formation such as the Topopah Spring welded tuff unit, the fractures divide the tuff matrix into blocks surrounded and bounded on all sides by the fractures. If the fractures are represented by parallel plates, then the fractures will either be completely filled

with liquid water or be completely drained. Liquid water within the porous blocks, isolated by the drained fractures, cannot flow from one matrix block to another. With parallel-plate fractures, liquid water in the matrix blocks cannot move and travel time will effectively be infinite under partially saturated conditions. This is simply too idealistic a model for performance assessment of flow and transport through a partially saturated, fractured porous formation.

Natural fractures are characterized by rough surfaces. In fractures at depth under compressional stress, the walls are pressed together, with a finite fraction of fracture surfaces in contact, such contacts being known as asperities. The aperture of a fracture will likely be smaller near the asperities and larger in the open channels within the fracture plane. As a fracture desaturates, the open region with larger apertures will be drained easily and liquid water will remain as pendular islands around the contact areas. The wetted regions centered around the contact areas provide the bridges for liquid water to flow across the fracture plane from one matrix block to its neighboring matrix blocks. Two schematic figures are used to illustrate the matrix-to-matrix flow pattern and fluid distribution in a fractured porous medium. Fig. 2.1 is in a cross section cut normal to the fracture plane showing the pores in matrix blocks and rough fractures with spatially varying apertures. Fig. 2.2 looks down on a fracture surface showing the distribution of contact areas and fluid configurations. With portions of fractures dry, liquid will tend to flow across fractures from one matrix block to another instead of flowing along the fractures. One may expect the flow lines to circumvent dry portions of the fractures as illustrated in Fig. 2.1. As a fracture desaturates, the liquid phase configuration will change from continuous phase at high saturation to discontinuous phase at low saturation with liquid forming rings around contact areas. With the idealized array of contact areas in Fig. 2.2, a sharp cutoff transition will separate the continuous liquid phase configuration from the discontinuous configuration.

Capillary theory, together with the rough fracture model, forms the basis of our conceptual model for a fractured porous medium under partially saturated conditions.

2.3 Aperture Distribution: *Approach to Quantify a Rough Fracture*

Mathematically, a rough fracture may be characterized by an aperture distribution function. As the fracture desaturates under a negative pressure head h, the portions of the fractures with aperture greater than the saturation cutoff aperture b_S,

$$b_S = -\frac{2\,\gamma\,cos\,(\theta)}{\rho g h}, \tag{2.3}$$

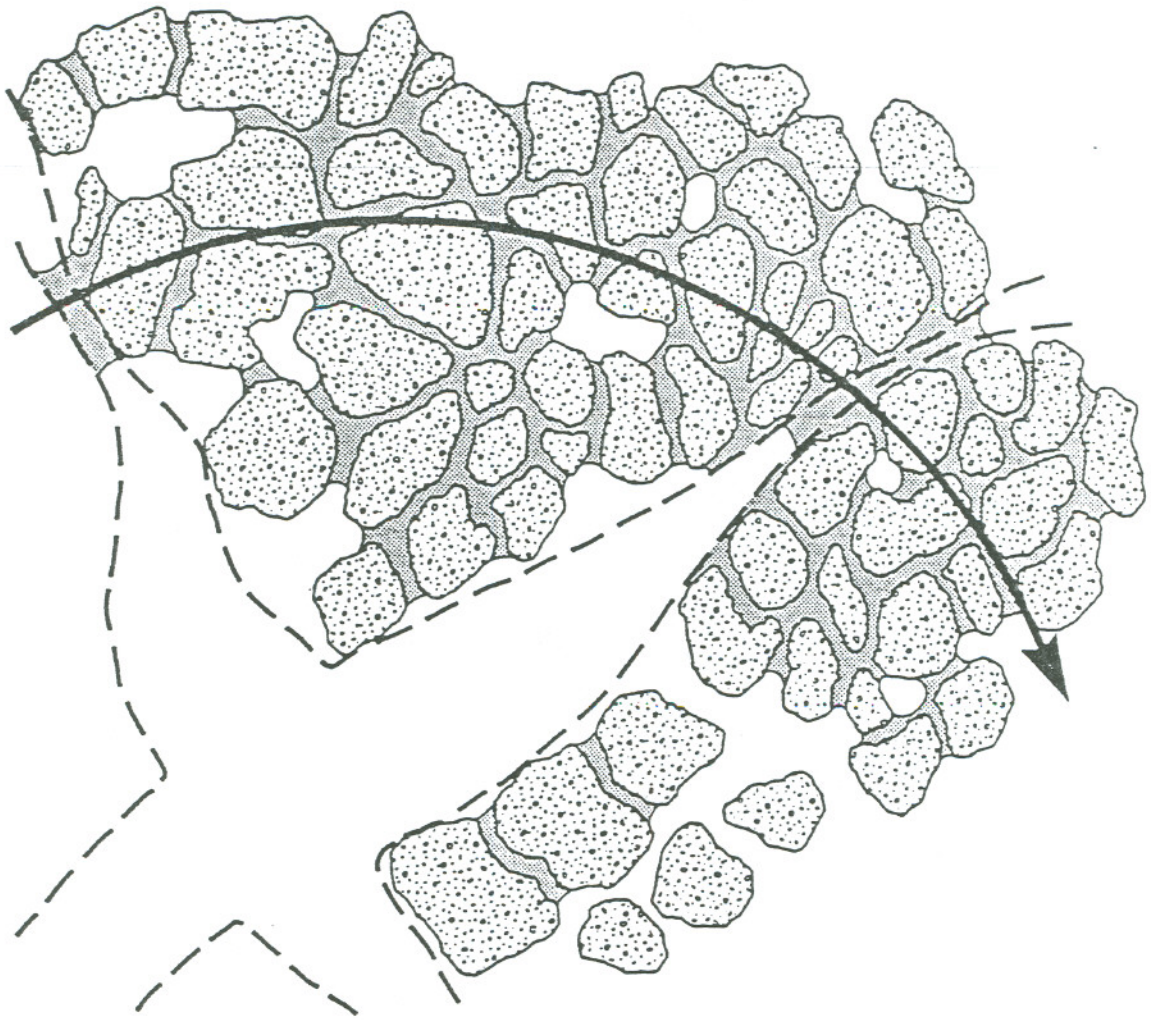

Figure 2.1 Schematic representation of water flow in a fractured porous medium.

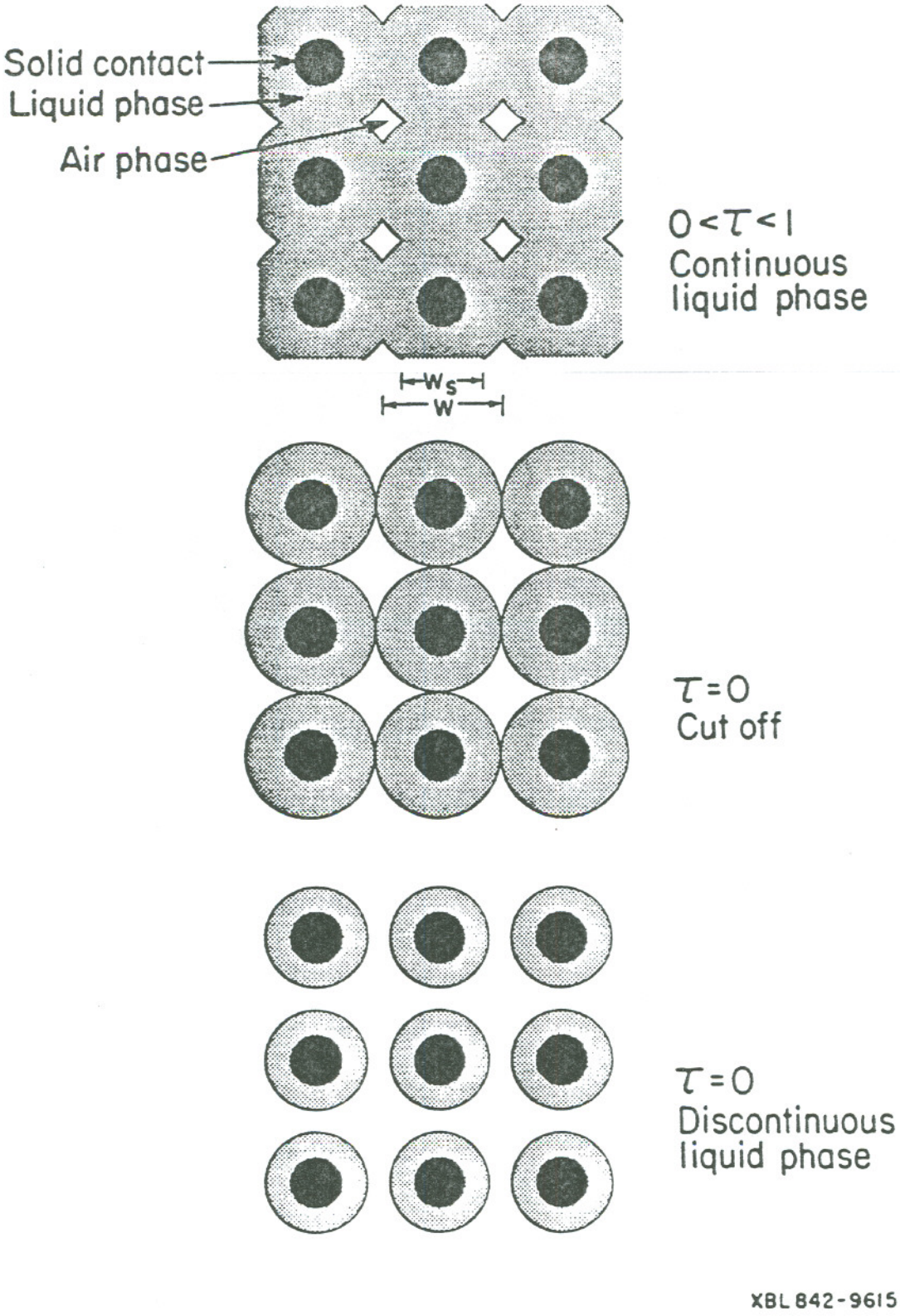

Figure 2.2 Schematic plan view of a fracture plane showing asperities (solid circles), liquid water (gray) and air (blank).

will be desaturated and unable to transmit liquid flow. We have derived relationships for fracture saturation $S(h)$, fracture relative permeability $k_r(h)$, and effective flow area for the fraction of wet fracture surface $\sigma(h)$ as functions of fluid pressure head h, in terms of integrals over the aperture distribution function $f(b)$:

$$S(h) = \frac{<b>_S}{<b>_1} ; \tag{2.4}$$

$$k_r(h) = \tau(h) \frac{<b^3>_S}{<b^3>_1} ; \tag{2.5}$$

where

$$<b^n>_S = \int_0^{b_S} b^n f(b)\, db, \quad n = 1, 3 ; \tag{2.6}$$

and

$$\sigma(h) = \omega + \int_0^{b_S} f(b)\, db , \tag{2.7}$$

where ω is the fraction of contact area.

The phase-constriction factor $\tau(h)$ in Eq. 2.5 accounts for the distortion of flow by the air pockets and sets the fracture permeability and flow to zero when the liquid phase is discontinuous. For the simple geometry shown in Fig. 2.2,

$$\tau(h) = \frac{W_S}{W} \tag{2.8}$$

can be related to the effective fraction of area $\sigma(h)$ occupied by the liquid water and contact area (Eq. 2.7). When the liquid flow path width W_S decreases to zero and the effective flow area is smaller than the area occupied by touching pendular rings, we have $\tau(h) = 0$ and $k_r(h) = 0$. If we neglect the phase-constriction effect by setting $\tau = 1$ for any h values, the relative permeability is determined by the average of aperture cubes in Eq. 2.5. This is equivalent to a capillary bundle model with all flow channels parallel to the direction of flow.

The general relationships 2.4, 2.5, and 2.7 can be used with any aperture measurement and distribution function. The detailed derivations and results to quantify the conceptual model are given in our first report (Wang and Narasimhan, 1984) and an archival paper (Wang and Narasimhan, 1985). For one simple aperture distribution function, the gamma distribution, we integrated explicitly to obtain algebraic relationships for the fracture characteristic curves.

The gamma distribution function

$$f_0(b_0) = \beta^2 b_0 e^{-\beta b_0}, \tag{2.9}$$

has only one parameter β to describe the variation of aperture b_0 of a fracture under zero stress. Under zero stress, the fracture surfaces are in point contact and the contact area is zero. In practice, $f_0(b_0)$ can be measured by scanning the open fracture surfaces and tracing the roughness profiles. The mismatch between the roughness profiles between two surfaces yields the aperture distribution function.

For in situ fractures with the surfaces in contact under nonzero stress, the fraction of contact area ω of the total area of the fracture can be expressed as

$$\omega = \int_0^{b_c} f_0(b_0)\, db_0 . \tag{2.10}$$

All the portions of fracture with initial aperture less than the contact cutoff aperture b_c will be in contact. The aperture under stress will be $b = b_0 - b_c$ in the open sections of the fracture. The aperture distribution function of the fracture under stress $f(b)$ in Eqs. 2.6 and 2.7 is

$$f(b) = f_0(b + b_c) = \beta^2 (b + b_c)\, e^{-\beta (b + b_c)} . \tag{2.11}$$

Table 2.1 summarizes the algebraic relationships for unsaturated fracture characteristic curves from integrations over the gamma distribution function with finite contact area ω and nonzero contact cutoff aperture b_c. Evans and Huang (1983) have constructed a fracture network model of parallel-plate fractures with the well-known lognormal aperture distribution. With lognormal distribution, they numerically evaluated the integrals in Eq. 2.6. Although the classical Evans and Huang model is for fracture network, the results can be reinterpreted for a single fracture with lognormal aperture distribution and zero contact area.

Very little data have been available to quantify the aperture distribution function for fractures in Yucca Mountain tuff. The simplicity of the gamma distribution function and especially the fact that there is only one parameter to quantify were on our minds when we chose it as the basis for detailed study. An added reason was that the limited analysis available at that time from a French study of natural granite fractures by Gentier (1986) indicated that $f_0(b_0)$ takes on a skewed shape, with long tails toward large apertures (Tsang, 1984). The gamma distribution can fit these aperture measurements well.

We should emphasize that we did not use granite data to represent tuff fractures. We used the gamma distribution function only to represent the functional form of the

Table 2.1 Fracture Characteristic Curves

Property	Algebraic Relationship*
contact area	$\omega = I_1(\beta b_c)$
effective flow area	$\sigma(h) = I_1(\beta b_c + \beta b_S)$
saturation	$S(h) = \dfrac{I_2(\beta b_S) + \beta b_c\, I_1(\beta b_S)}{I_2(\infty) + \beta b_c\, I_1(\infty)}$
relative permeability	$k_r(h) = \tau(h)\, \dfrac{I_4(\beta b_S) + \beta b_c\, I_3(\beta b_S)}{I_4(\infty) + \beta b_c\, I_3(\infty)}$

* $I_1(x) = 1 - (1 + x)\, e^{-x}$

$I_2(x) = 2 - (2 + 2x + x^2)\, e^{-x}$

$I_3(x) = 6 - (6 + 6x + 3x^2 + x^3)\, e^{-x}$

$I_4(x) = 24 - (24 + 24x + 12x^2 + 4x^3 + x^4)\, e^{-x}$

aperture distribution. Without actual aperture measurements on fractures in tuff, we used available fracture spacings and bulk permeability of tuff to inversely determine the β parameters. The assumptions and procedures used to determine β parameters from available tuff data will be discussed in Sec. 3.1. The fracture distribution functions derived for the vertical fracture and for the horizontal fracture are plotted in Fig. 2.3, with distribution parameters derived from Topopah Spring welded tuff data. The distribution functions are normalized, with the areas under the curves set equal to unity. Both vertical and horizontal fractures have hydraulic apertures in the sub-millimeter range according to these indirectly derived aperture distribution functions.

2.4 Flow Across Fractures: *Importance of Effective Flow Area*

For fractures underground, we expect that a fraction of the apertures will be closed under stress. We do not have data for the fraction of *in situ* contact area. However, borehole USW-G4 core analyses (Spengler and Chornack, 1984) indicate that about 12% of the fracture surfaces have coatings of zeolite, clay, and calcite which are likely minerals precipitated from water. We made an assumption that the fracture coatings of 12% correspond to the fraction of *in situ* contact area ω. We assume that contact areas

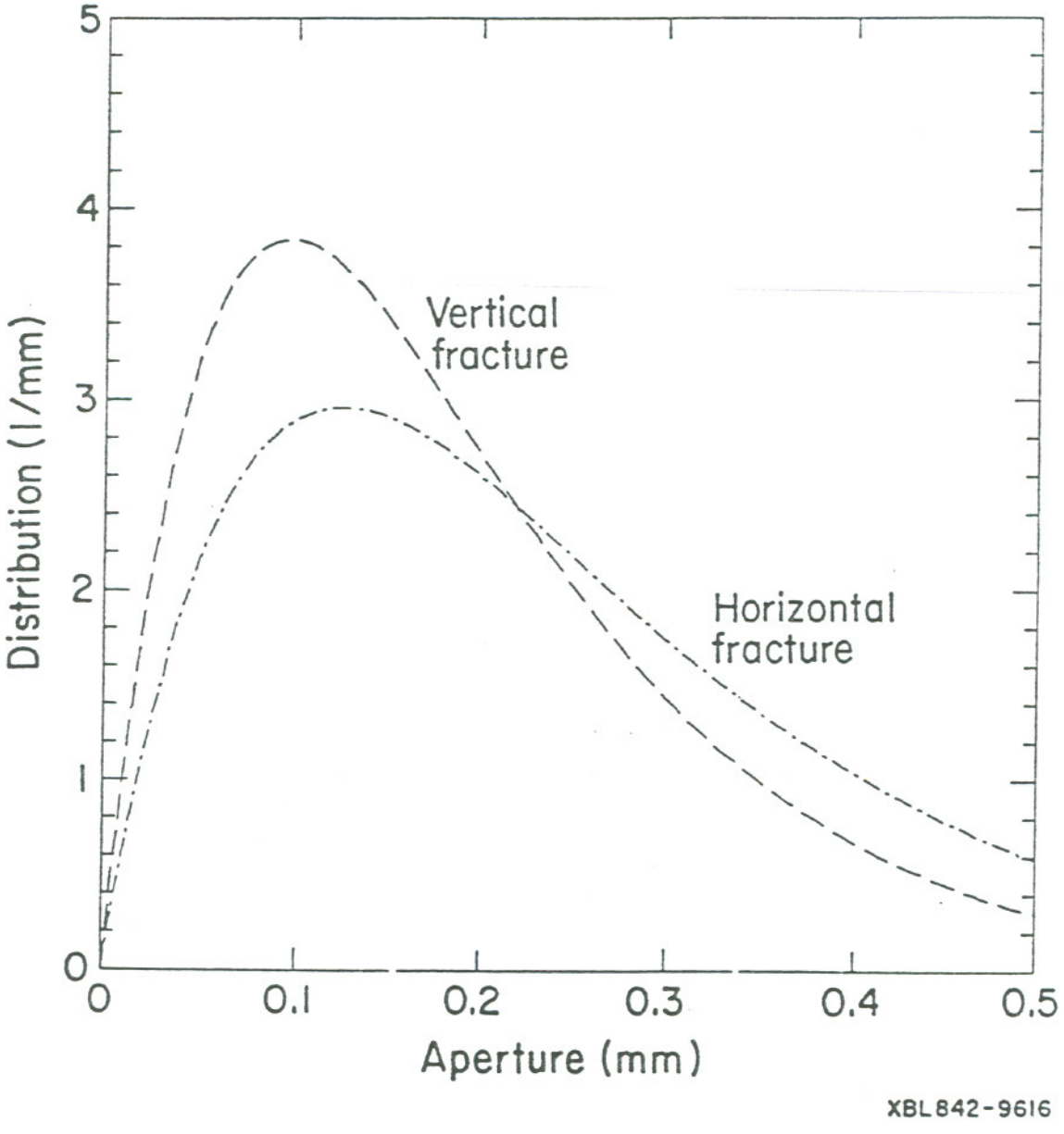

Figure 2.3 Aperture distributions for the Topopah Spring welded tuff unit (distribution parameter: vertical fracture - $\beta_v = 10.4\ mm^{-1}$; horizontal fracture - $\beta_h = 8.04\ mm^{-1}$).

remain wetted for a long time and allow hydrochemical alterations to occur in contact areas for the coatings to form. This assumption to relate fracture coatings with fracture contacts remains to be checked for consistency against other goechemical and geomechanical data. We believe that the evolution of fracture coatings can shed light toward a better understanding of the long-term processes relating mechanical deformation and stability, chemical dissolution and precipitation, and hydrological flow and transport in fractured, porous tuff under partially saturated conditions.

If both the matrix blocks and the fractures are fully saturated with liquid water, the whole fracture-matrix interface will be available for water to flow from the matrix into the fracture and vice versa. As the fractures drain, only a fraction of the area in the fracture surfaces will enable flow from one matrix block to another block across fracture. Fig. 2.4 shows that the effective flow area at fracture-matrix interfaces decreases and quickly approaches the limiting contact area fraction of 12% as the pressure head decreases. With liquid flow from one matrix block to another restricted to cross the interfaces through reduced areas, the flow lines will converge toward, then diverge away from contact areas. Therefore, flow paths will be more tortuous in a partially saturated, fractured porous medium. The pressure dependence of effective fracture-matrix area is not taken into account in conventional numerical models. We incorporate this effective area dependence into the TRUST code (Narasimhan *et al.*, 1978) to properly simulate the flow in fractured tuff systems.

2.5 Transport Properties of Fractured Tuff: *Contrasts between Fracture and Matrix Characteristics*

The relation between water saturation and pressure head and the relation between permeability and pressure head are two physical functions that are essentially required for modeling water movement in the fractured tuff. Fig. 2.5 compares the fracture characteristic curves with the tuff matrix characteristic curve of saturation versus head for the Topopah Spring welded tuff unit. The tuff matrix curve was provided by SNL from laboratory measurement of a representative core sample (Peters *et al.*, 1984). The thermocouple psychrometer matrix data were fitted with the equation suggested by van Genuchten (1980). Fig. 2.5 shows that the fractures will desaturate easily with a small suction of $-0.1\,m$. The saturation in the matrix will remain high. If the *in situ* matrix saturation in Topopah Spring welded tuff unit is 0.8, then the negative pressure head in this unit is over $-100\,m$. With such a large suction, the fracture saturations will be essentially zero.

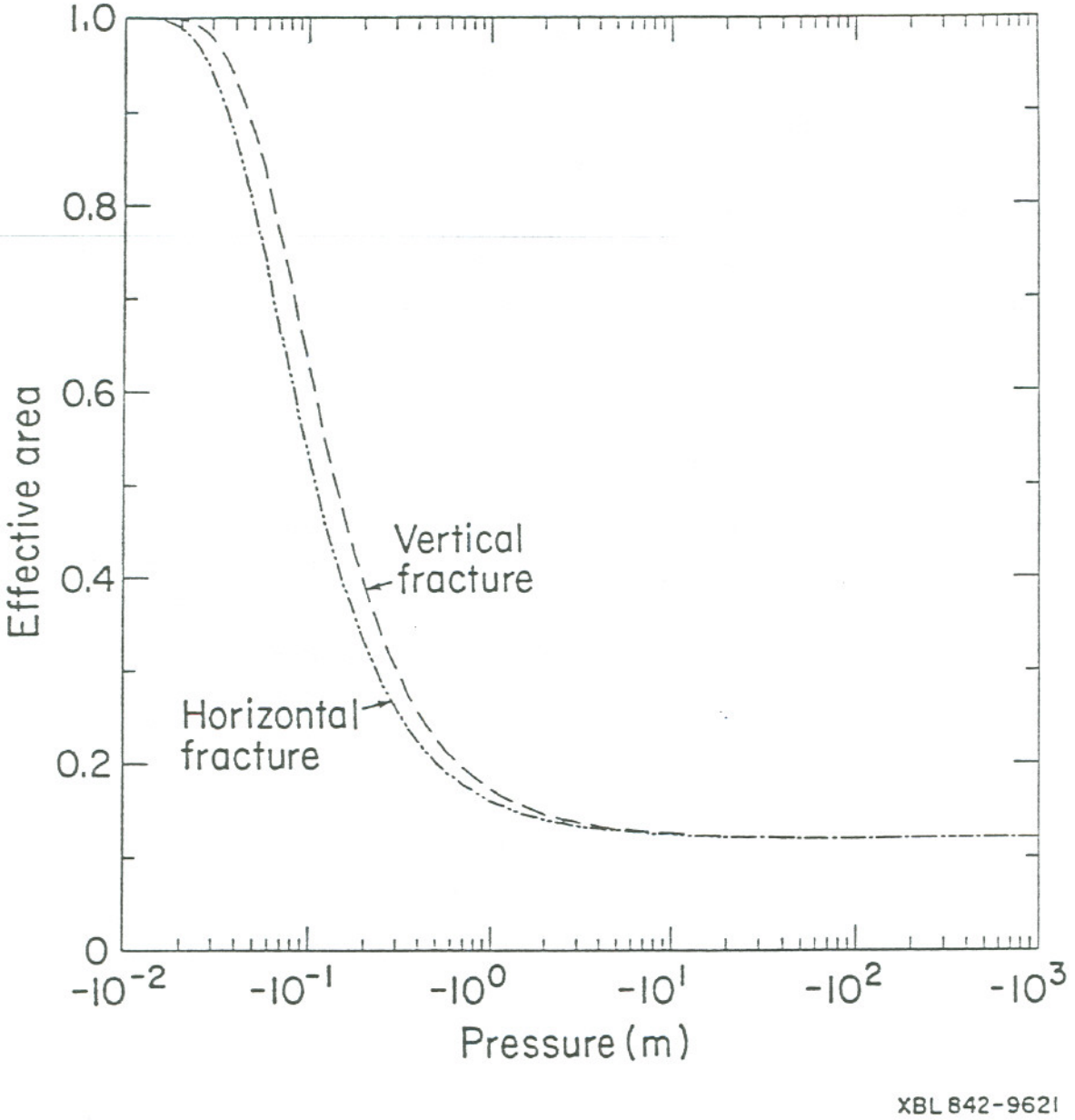

Figure 2.4 Effective flow area versus pressure head for flow across the fracture plane.

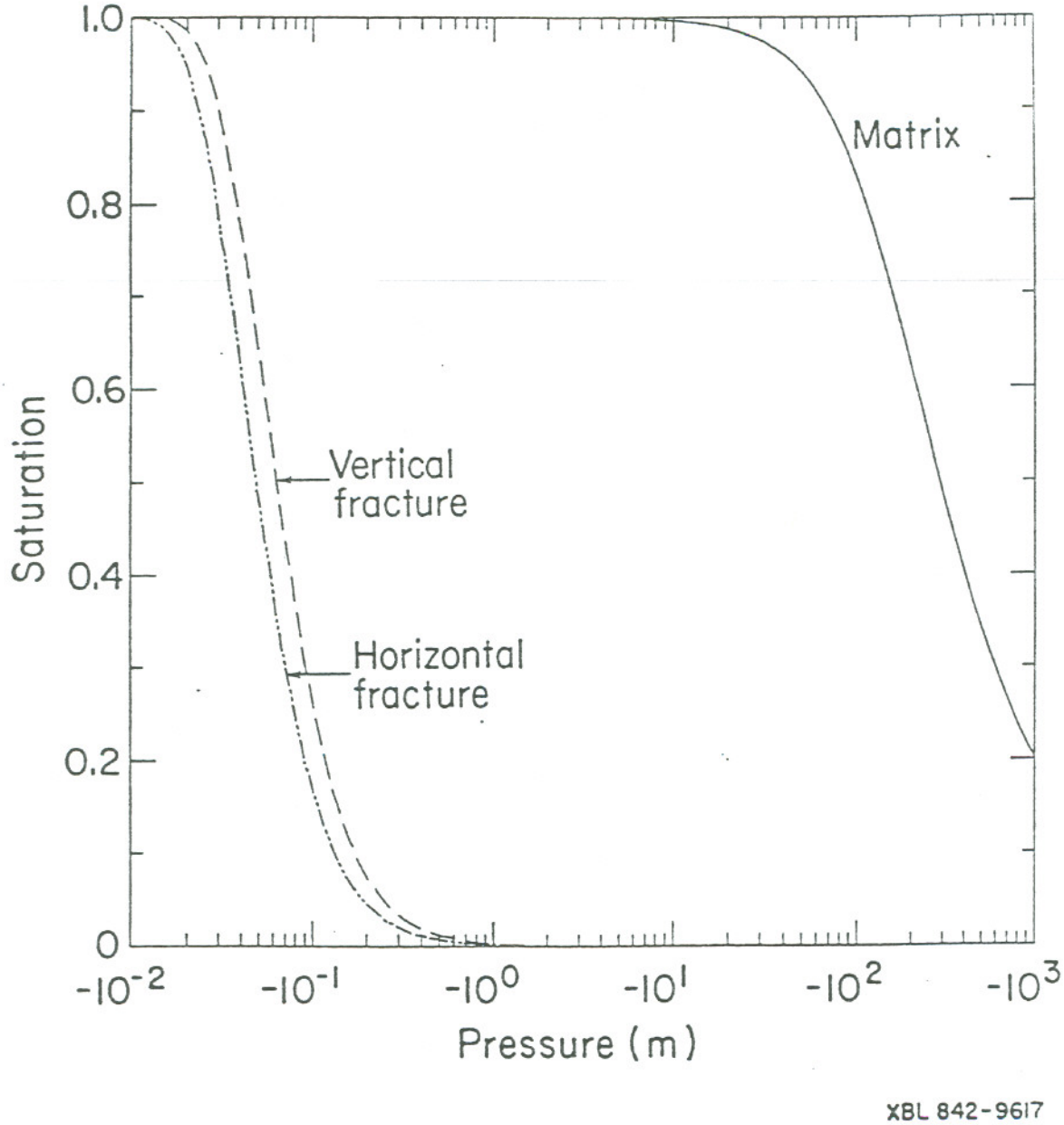

Figure 2.5 Saturation characteristic curves of fractures and tuff matrix.

The relations between effective permeability and pressure head are shown in Fig. 2.6 which shows that the fracture permeabilities are very sensitive to suction. The fracture permeabilities are also sensitive to whether the phase-constriction factor $\tau(h)$ is included in the calculations (Eq. 2.5) to take into account the effects of blockage of flow by air pockets, the flow-path distortion around the air pockets, and the transition from continuous to discontinuous liquid phase associated with desaturation. If fully saturated, the permeability of each discrete fracture is eight orders of magnitudes greater than the matrix permeability. With small suctions in the range of -0.1 to $-10\,m$, the discrete fracture permeabilities decrease drastically, especially for the curves with the phase-constriction factor. The matrix permeability decreases much more gently as the pressure head becomes more negative. Near fully saturated conditions, the fractures will control the fluid flow. As desaturation proceeds and the fracture permeability of each discrete fracture becomes less than the matrix permeability, the matrix will control the flow. With *in situ* suction of over $-100\,m$, fracture flow diminishes and matrix flow dominates. The drastic change of the role played by the fractures as the active main conduits for flow and transport in saturated conditions to become passive dry pores in unsaturated conditions is the most important result arising from our conceptual model. If the role reversal between fracture flow and matrix flow does not occur under ambient partially saturated conditions, then the highly fractured tuff unit will transmit liquid water very quickly through the connected fracture networks and the travel time will be very short. Substantiating our finding for the role reversal between fracture flow and matrix flow is crucial for the performance assessment of the partially saturated flow field at Yucca Mountain.

3.0 Drainage Responses of a Fractured Tuff Column: *Dynamic Interaction between Discrete Fractures and Porous Matrix*

With the development of a conceptual model based on capillary theory and aperture distribution of rough-walled fractures, we used the fracture characteristic curves derived in 1983 to study the detailed responses of a fractured, porous tuff column in 1984, taking explicitly into account the vertical and horizontal fractures and tuff matrix blocks. Our finding that fracture pressure and matrix pressure are approximately equal after the column is drained provides a rational basis for the development of a composite medium model at SNL by Peters and Klavetter (1988). In addition, the dominance of liquid flow in the matrix, together with the findings by Pruess *et al.* (1985) that gas flow occurs mainly through the fractures has provided incentive for the concurrent development of a

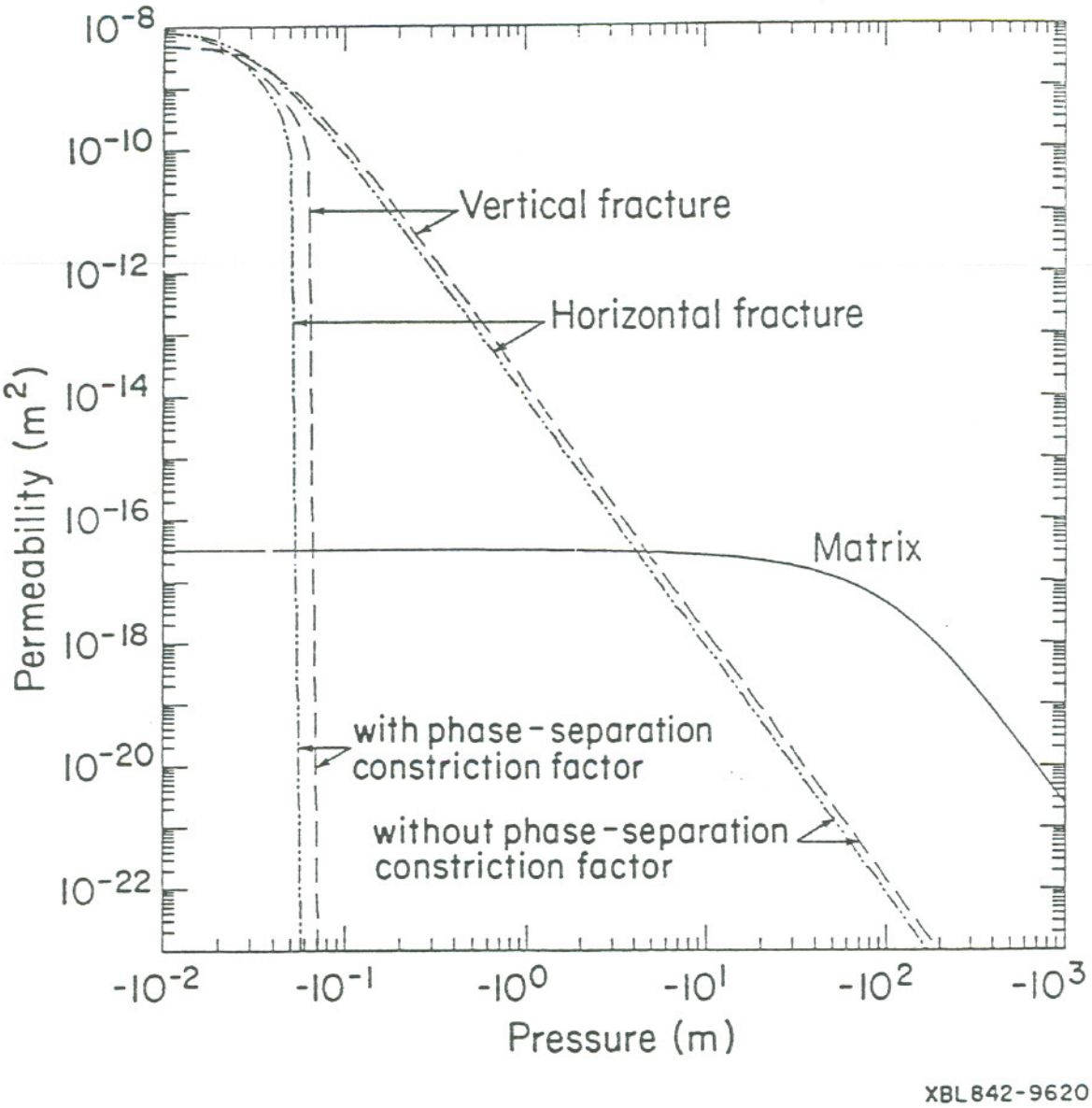

Figure 2.6 Permeabilities of partially saturated fractures and tuff matrix.

multi-phase composite medium model. This model is known as an effective medium model. Detailed studies with discrete fractures are valuable for better understanding of system behaviors and for developing useful approximations for large-scale analyses.

3.1 Fracture Description: *Adaptation of Field Data*

To construct the detailed model representing the Topopah Spring welded tuff unit, we first analyzed available data on fracture orientation and spacing at Yucca Mountain. There are two nearly vertical fracture sets: one strikes roughly north-northwest, and the other, north-northeast (Scott *et al.*, 1983). Fracture inclination data from borehole USW-G4 (Spengler and Chornack, 1984) also indicate the presence of a minor, nearly horizontal fracture set. By grouping the fractures as either nearly vertical or nearly horizontal according to their dip inclinations and using the measured fracture frequency of $4.36/m$, we determined the average fracture spacings of the sets as shown in Fig. 3.1. We assumed that the two nearly vertical sets had equal spacing and that they contributed equally to the equivalent fracture continuum permeability (cube of aperture divided by spacing).

Without the direct availability of data for the equivalent fracture continuum permeability in 1984, we deduced the equivalent permeability value $k_f = 1.02 \times 10^{-11}\ m^2$ from well testing in well J-13 (Thordarson, 1983). Well J-13 is located in a low-standing structural block east of Yucca Mountain with part of Topopah Spring welded tuff unit below the water table. It is assumed that the water pumped out during testing had moved through a connected network of fractures which provide effective pathways for fluid movement under saturated conditions. We also assumed that equivalent fracture continuum permeability was isotropic.

Along a given direction in three dimensional space, two fracture sets contribute to the equivalent fracture continuum permeability k_f. We assume that

$$\frac{k_f}{2} = \frac{<b^3>_1}{12\,d} \tag{3.1}$$

for each set with spacing d. With gamma distribution Eq. 2.11 in Eq. 2.6, we have

$$<b^3>_1 = \frac{24 + 6\,\beta b_c}{\beta^3}\, e^{-\beta b_c}\,. \tag{3.2}$$

Since βb_c can be determined by the parameter ω (Table 2.1 and Sec. 2.4), we can used Eq. 3.1 to determine the distribution parameter β for each fracture set, as shown in Fig. 2.3. All other fracture characteristic curves in Table 2.1 can then be evaluated.

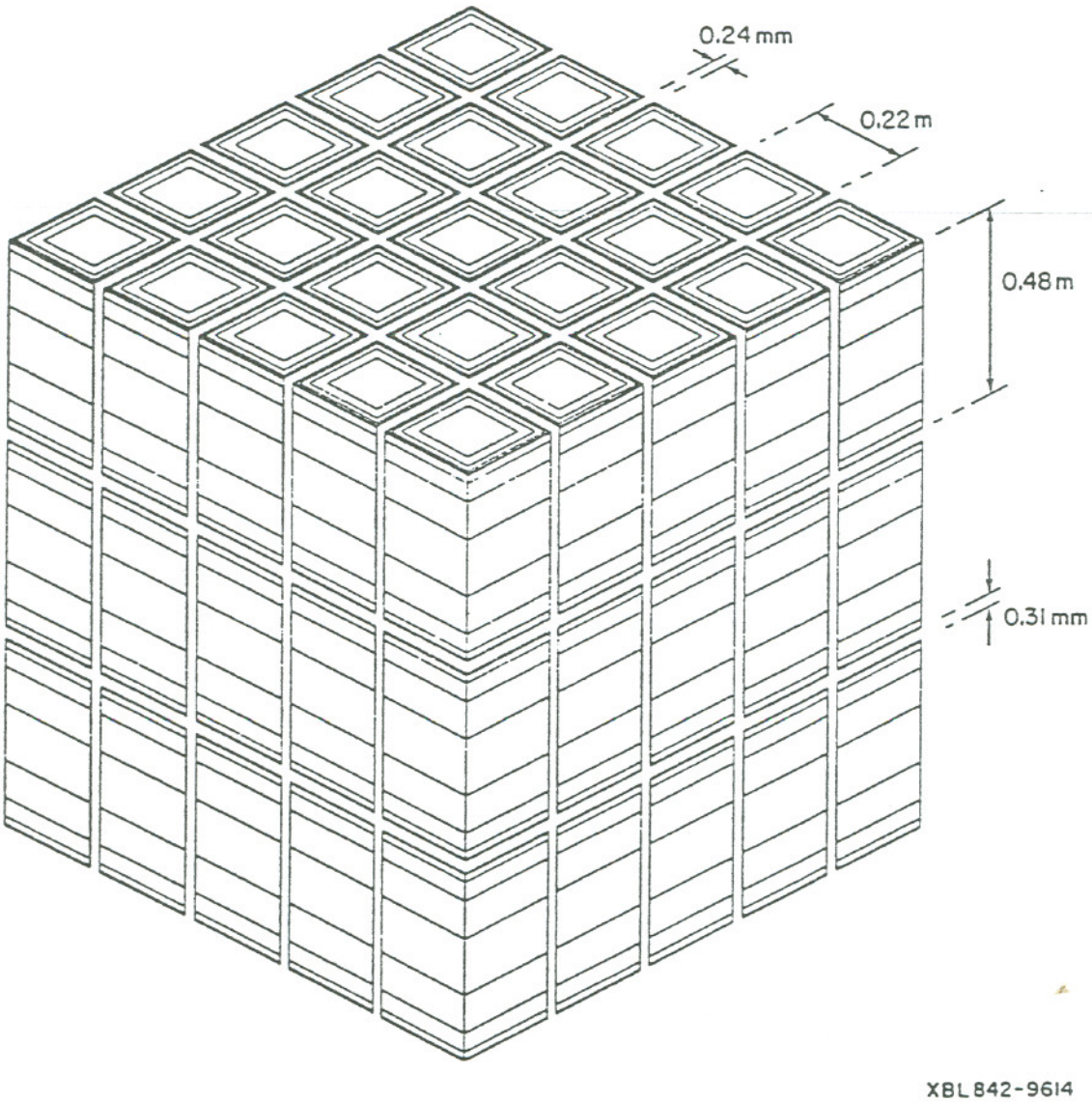

Figure 3.1 Schematic representation of three fracture sets for the Topopah Spring welded tuff unit.

The steps outlined above show that the parameters used in our simulations were derived from available tuff data and no other parameter values were assumed or adjusted in the tuff fracture desaturation curves. The simplying assumptions about the fracture network can be easily relaxed and the procedures of fracture network analyses can be generalized to determine anisotropic fracture spacings and non-parallelepiped blocks from more data on anisotropic equivalent continuum permeability tensors. In the course of this study, we have continuously updated our models as more realistic data were provided by SNL and incorporated them into later simulations.

3.2 Discrete Fracture - Porous Matrix Model: *Nested Matrix Elements*

With the spacings of the fracture sets and the sizes of the tuff matrix blocks determined, we constructed a small discrete fracture-porous matrix model to simulate vertical drainage of a fractured tuff column (Fig. 3.1). Two horizontal fractures, normal to the direction of general flow, are explicitly simulated. On the local scale, lateral flow is allowed between the vertical fracture and the matrix blocks. The horizontal cross section of a matrix block is further partitioned into six nested elements and the vertical cross section of each block is sliced into nine sections. The grid elements are small near the fractures and large toward the middle of the matrix block. The partition of horizontal nested elements is similiar to that used in the multiple interacting continuum idealization (MINC) (Pruess and Narasimhan, 1985). Such a nested grid allows the simulation of convergent flow from the fractures into the matrix block and divergent flow from the matrix block into the fractures with relatively few elements if we are interested mainly on the fracture-matrix interflows and not concerned with the detailed flow field near the diagonals within the matrix block. The nested elements also take properly into account the geometrical configuration with each horizontal cross section of a matrix block surrounded by fractures on all four sides. The usual semi-analytic treatments of fracture-matrix flow with one-dimensional approximations do not properly account for the multiple-side effects. In the simulations, we did not group the matrix elements from different blocks at different elevations together. The two horizontal fractures and the three matrix blocks within each vertical column are explicitly simulated. In this respect, we did not carry out the simulation in the multiple interacting continuum grouping approximation and account for the effects of discrete fractures in detail.

3.3 Tool of Analysis: *The TRUST Code*

In 1984, we modified the TRUST code to account for the effective flow area with the available area for flow across the fracture-matrix interfaces determined by the

fracture saturations. At the limit that the fractures are completely desaturated, the available area is the contact area between adjacent blocks for matrix flow from one block to the next. The outermost matrix node for one block is connected to the fracture and is not directly connected to the matrix node in the next block in the simulations. It is important to note that fracture permeabilities are intrinsically defined only along the fracture planes. Normal to the fracture matrix interfaces, the fractures will not introduce any resistance under both the saturated conditions and under partially saturated conditions with flow through finite wetted areas around contact points. With the integrated finite difference method (Narasimhan and Witherspoon, 1976) in the TRUST code, this can be easily taken into account by setting the distances from the fracture nodes to the fracture-matrix interfaces to zero so that normal flow from matrix blocks to fractures is controlled by matrix permeability. We point out this detail in the simulation because the conventional finite difference and finite element codes do not usually take this intrinsic anisotropy of fracture permeability into account. If the proper treatment of fracture permeability is not taken into account, the zero permeability of the fracture elements under completely desaturated conditions will block the flow from one matrix block to the next. Physically, we expect that flow will cross one matrix block to another matrix block through the finite contact areas.

In 1984, we used the usual harmonic mean approximation to determine the conductances at the element interfaces from permeability values of neighboring nodes weighted by the distances from the node center to the interfaces. If we use the geometry-imbedded Darcy's law (Narasimhan, 1985), we can probably reduce further the number of nested elements from six to one or two for each horizontal matrix block cross section and similiarly for the vertical grids. The development of geometry-imbedded path-integration modeling techniques can increase the efficiency and accuracy of modeling discrete fracture-porous matrix systems.

3.4 Major Findings: *Flow Dominance by Matrix*

We simulate the transient changes in the fractured tuff column from initial fully saturated condition to final partially saturated condition. Initially the column is filled with water with pressure determined by hydrostatic equilibrium. The hydraulic head is everywhere zero and fluid is stationary. At time $t = 0^+$, a negative suction head is applied to the lower boundary to induce drainage and transient changes in the fluid flow field throughout the fractured, porous tuff column. The boundary suction head is over $-100\ m$ which corresponds to a final ambient matrix saturation of $S = 0.8$.

The transient pressure drops at different locations in the column are shown in Fig. 3.2 for three cases. We studied five cases for flow in the column: (1) a fractured, porous tuff matrix column with the phase-constriction factor taken into account for the discrete fractures ($1 \le \tau(h) \le 1$); (2) a fractured, porous column without the phase-constriction factor ($\tau = 1$); (3) a matrix column without fractures; (4) a discrete fracture column without matrix and with τ factor; and (5) a discrete fracture column without matrix and without τ factor. The locations of interest are the middle of the matrix block (point A), the middle of the vertical fracture (point B), the middle of the upper fracture (point C), and the middle of the lower horizontal fracture (point D), as shown in the inserts of the plots.

The pressure drops for the first three cases at different locations in Fig. 3.2 are essentially the same after an initial desaturation period of $10^{-2}\,yr$. Within this short period, the onset of fracture desaturation depends on whether the phase-constriction factor is taken into account as shown in the small differences between the top two plots in Fig. 3.2. As pressures become negative following initial desaturations, the pressure changes are controlled mainly by the matrix. At the same elevation, the matrix pressure at point A and the vertical fracture pressure at point B are approximately the same. The fracture-matrix pressure equilibrium is reached. The lower fracture, point D, is closer to the suction boundary and has more negative pressure than the higher elevation points. The simulation results involving only matrix in the third plot in Fig. 3.2 are nearly identical to the results with discrete fractures simulated. It is clear, therefore, that pressure changes can be simulated with matrix properties only, if the transition from saturated conditions to unsaturated conditions is not of interest. We also simulate the changes in the fractured column without the matrix (case 4 and case 5) and obtain very unrealistic results to illustrate the importance of porous matrix blocks as flow channels for fluid to change pressure (Wang and Narasimhan, 1985).

Associated with the pressure drops, the fracture saturations drop abruptly at early times. The matrix changes more slowly from the initial fully saturated condition of $S = 1$ to the final ambient saturation of $S = 0.8$. These changes are observed in the simulated results. They can also be deduced from the characteristic curves in Fig. 2.5. The permeability changes confirm the role reversal between fracture flow at saturated condition and matrix flow after the desaturations. The effective fracture-matrix flow area changes abruptly from 100% at full saturation to 12%, the contact area fraction. The simulated results suggest that the ambient flow field is through the matrix blocks, the fractures are dry, and the flow lines are distorted in crossing from one matrix block to the next matrix block through fracture contact areas.

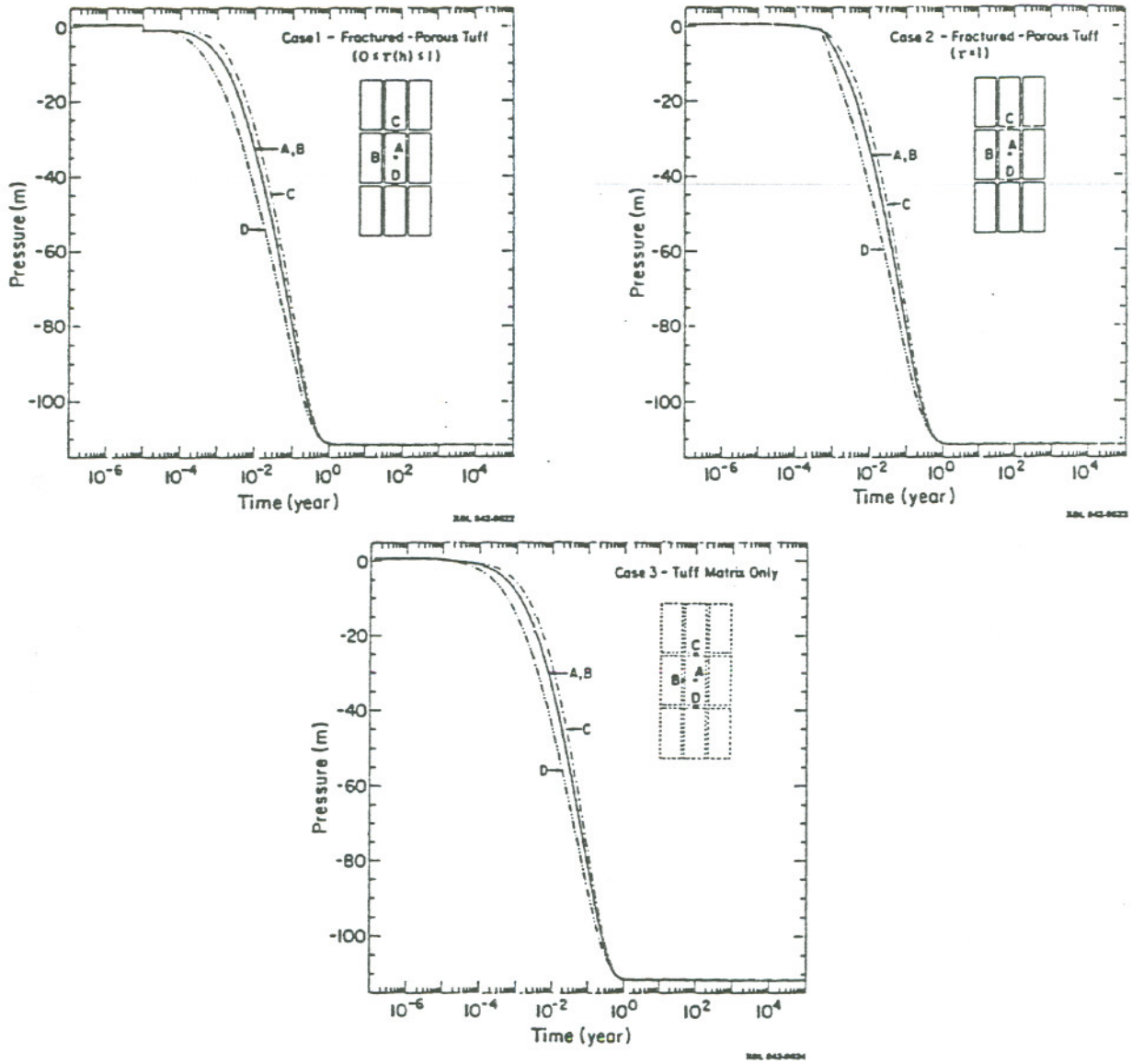

Figure 3.2 Unsaturated drainage in a tuff column: comparison of pressure changes for three different conceptualizations.

In addition to pressure, saturation, permeability, and effective fracture-matrix flow area changes, we also calculate the Darcy velocity versus time at different locations. With the dependence on both permeability and pressure gradient, the Darcy velocity changes are very sensitive to the details of fracture-flow characteristics. Before the fractures completely desaturate, we have the flows along the fractures change from initially static condition, to large flows associated with fast fracture drainage, to abrupt flow stoppage as the fractures lose the water within the small fracture volume. The fracture-matrix interflows are also sensitive to fracture characteristics. Fig. 3.3 illustrates the changes in Darcy velocities across the fracture-matrix interfaces at the midpoints of fractures. Before the fractures desaturate, the fluid in the matrix flows toward the fractures to supply the fluid in the fractures which is drained rapidly by the suction. At the saturated-desaturated transition, these fracture-matrix flows change drastically. After the transition, the fluid mainly moves vertically from upper matrix blocks, across horizontal fractures, into lower matrix blocks. The horizontal flow also reverses direction from an initial matrix-to-fracture flow to a small but significant fracture-to-matrix flow. After the transition, the fractures no longer transmit fluid and become a passive and small fluid storage source to feed the matrix blocks as they drain.

After the fractures desaturate, the Darcy velocities from one matrix block across the fracture into the next matrix block are essentially the same as those calculated by a matrix-only model, as illustrated in case 3, Fig. 3.3 for a tuff matrix column without fractures. The agreement among the velocities in cases 1, 2, and 3 strongly indicates that the fluid flow field of a partially saturated, porous formation can be simulated without taking fractures into account, if the transition region from saturated to unsaturated condition is not of concern.

In quasi steady-state flow, although the dry fractures limit the available areas for flow to cross from one matrix block to another matrix block, the total flux through the fractured column is insensitive to local distortion near the fracture-matrix interfaces. In the 1984 studt, we did not simulate the flow field in the scale of individual fracture contacts. The effects of the small-scale heterogeneity are taken into account by the statistical average procedures used in deriving the relative permeabilities and effective fracture-matrix flow areas. Although the total quasi-steady flow is not sensitive to the flow path distortion through the fracture-matrix interfaces, the particle velocity field and the solute transport are expected to be affected by the reduction of fracture-matrix flow areas. We need to study the fundamental process at small scale around individual contact area at fracture-matrix interfaces to achieve a better understanding of the particle movement through fractured, porous tuff systems.

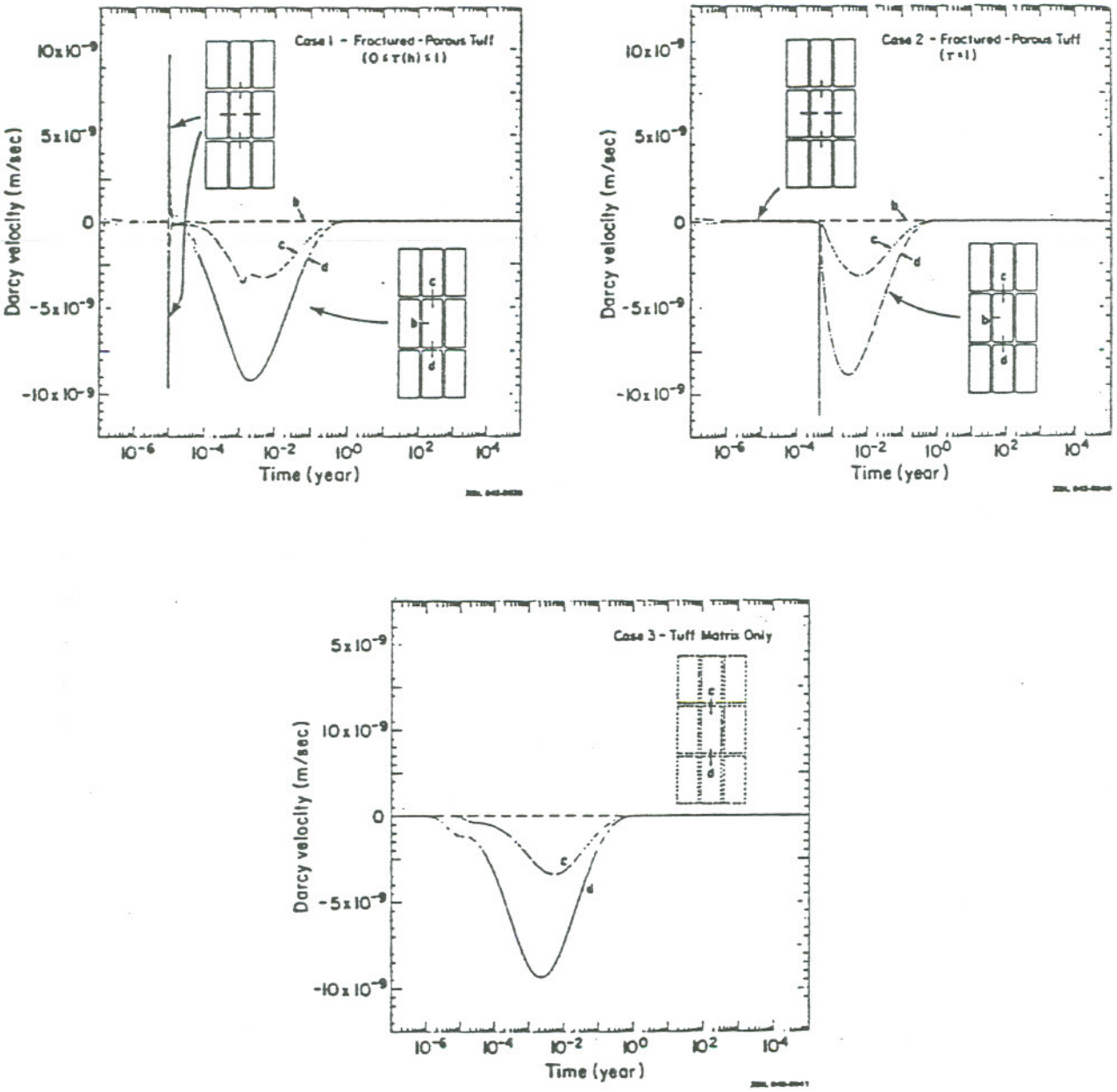

Figure 3.3 Unsaturated drainage in a tuff column: patterns of darcy velocities (sign convention: horizontal fracture - flow into fracture is positive; vertical fracture - upward is positive).

3.5 A Useful Corollary: *The Composite Model*

One of our important findings in 1984 was that the fracture pressure and matrix pressure were approximately the same. This suggests that one may simplify the simulation by considering only one pressure field. The fracture-matrix pressure equilibrium, or more generally thermodynamic equilibrium to include temperature as well as pressure, is one of the essential assumptions of the composite medium-effective continuum models (Peters and Klavetter, 1988; Pruess *et al.*, 1985, 1990). With the same pressure defined for both the fractures and the porous matrix, one governing equation is sufficient for a fractured, porous matrix system. In the composite medium-effective continuum governing equation, the equivalent saturation is expressed as a sum of fracture saturation S_f and matrix saturation S_m, weighted by continuum porosities. The equivalent permeability is also expressed similiarly by a sum of fracture permeability $k_s k_{rf}$ and matrix permeability $k_m k_{rm}$.

$$S_{fm}(h) = \frac{S_f(h)\phi_f V_f + S_m(h)\phi_m V_m}{\phi_f V_f + \phi_m V_m} = \frac{S_f(h)\bar{\phi}_f + S_m(h)\bar{\phi}_m}{\bar{\phi}_f + \bar{\phi}_m} . \tag{3.3}$$

$$k_{fm}(h) = k_f k_{rf}(h) + k_m k_{rm}(h) . \tag{3.4}$$

The subscripts f and m refer to the fracture and matrix domains, respectively. ϕ is the porosity (void fraction) of intact domain and $\bar{\phi}$ is the equivalent continuum porosity of the voids in one domain as a fraction of total volume $V = V_m + V_f$.

There is no conceptual difficulty to accept the assumption that the equivalent saturation is a porosity-weighted sum of fracture saturation and matrix saturation. Saturation is a scalar quantity which is defined as the ratio of saturated volume to pore volume. The permeability, on the other hand, is not a scalar. By summing over fracture permeability and matrix permeability, the fracture flow channel and the matrix flow channel are intrinsically assumed to be parallel in the composite medium-effective continuum models. In view of the popularity and usage in benchmark studies, we have programmed these composite saturation and permeability characteristic functions into the TRUST code. We also used these models later in this study for some of the large-scale simulations. However, there is a need to check the results of simpler models from time to time, with the results generated from detailed discrete fracture-porous matrix models. More important, the assumptions and limits of simpler models must be kept in mind when we use and interpret the results from these models. For example, the composite model is adequate for vertical infiltration studies if we only consider vertical fracture sets so that both fracture flow and matrix flow are vertical. For multi-dimensional simulations with potential lateral flows crossing the fractures, it remains to be determined if composite models are

adequate. The development of large scale models to account for both fractures and porous matrix blocks remains to be an important task for the studies of a partially saturated flow field of a fractured, porous system.

4.0 Vertical Infiltrations through Welded-Nonwelded Units: *Maintenance of Unsaturated State*

In 1985, we extended our models from a short column with a few fractures to a tall column over 500 *m* in depth to represent the whole unsaturated zone from ground surface to the water table. Yucca Mountain consists of alternating units of welded and nonwelded tuff. The infiltration of water through these alternating layers were studied under steady and transient conditions. We wanted to determine if spatial heterogeneities associated with welded-nonwelded interfaces and temporal variations associated with extreme flooding on the ground surface can induce significant fracture flow in the Topopah Spring welded tuff unit. For performance assessment, the flow velocity field from the repository in the Topopah Spring welded tuff unit to the water table determines the groundwater travel time. The onset of significant fracture flow will shorten the travel time drastically.

4.1 Fracture and Matrix Data and Model: *Observational Basis*

To construct models representing the welded and nonwelded units, we analyzed the fracture orientation and spacing data from borehole USW-G4 (Spengler and Chornack, 1984) for all the unsaturated units. For the welded units, Tiva Canyon (TCw) and Topopah Spring (TSw), fracture densities are high and fracture spacings are in the sub-meter range. For the nonwelded units, Paintbrush (PTn), vitric Calico Hill (CHnv), and zeolitic Calico Hill (CHnz), fracture densities are low and fracture spacings are in the meter and tens of meter range. It is generally assumed that flow of water in the nonwelded units is dominated by matrix, and fractures can be ignored. Within fracture planes, we assumed that the contact areas were identical to the areas where mineral coatings occurred in the fractured cores. The fraction of fracture coatings, predominately clay, calcite, and zeolite, increases with depth. This is consistent with the closure of fractures with depth as a result of overburden stress. The equivalent fracture continuum permeabilities for the welded and nonwelded units were based on the estimates of Thordarson (1983) and Sinnock *et al.* (1987). For the tuff matrix, we used the characteristic curves of the representative samples chosen by Peters *et al.* (1984).

We used either a discrete fracture-porous medium model or a composite medium model in the simulations. Before we discuss the detailed models, we will briefly review the results from one-dimensional composite medium simulations. One-dimensional infiltration problems have been extensively studied, especially the steady-state cases. In a one-dimensional column, we can represent the different units with nonuniform grids, as illustrated in Fig. 4.1. The thicknesses of the units correspond to the values determined from borehole USW-G4 (Ortiz *et al.*, 1984).

4.2 Estimate of Ambient Infiltration Rate: *Observational Constraints*

Although the infiltration rate is a given input parameter and controls the simulation results, it has not been determined by direct measurements, but rather determined inversely by models, ambient saturation, and other characteristic parameters. Especially, the effective matrix conductivity under partially saturated conditions determines the infiltration rate. The saturated conductivity for the TSw matrix is about 1 mm/yr for the representative sample used in our 1985 analyses. Our calculations showed that for the 0.1-mm/yr case (Fig. 4.2) and for the 0.5-mm/yr case (Fig. 4.3) the saturation profiles were uniform and the corresponding fluid pressure constant in the upper part of the TSw unit.

In the range of the constant pressure profile, the pressure gradient is, of course, zero, and the hydraulic potential gradient is unity from the gravity component alone. In the range of the unit hydraulic gradient, the partially saturated hydrualic conductivity is equal to the Darcy velocity which is equal to the steady infiltration rate. The solution in the thick TSw unit is essentially determined by demanding the saturation to attain a uniform value at which the infiltration rate exactly matches the partially saturated, effective hydraulic conductivity.

The ambient saturation for TSw was estimated by SNL to be 0.8 in 1983 and later reduced to 0.69 ± 0.15 (Sinnock *et al.*, 1987; Reference Information Base (RIB), SNL, 1986). With an ambient saturation of 0.8 or lower, the modeling results indicate that one can only allow the system to have 0.1 mm/yr or less water flowing through the system. If one increases the infiltration rate over 0.1 mm/yr, the TSw saturation will be higher than the ambient saturation. The ambient saturation can be easily measured in the field by weighing analyses of core samples. Net infiltration rates, on the other hand, cannot be easily and directly measured. We are not aware of any practical experimental technique to directly measure low infiltration rate under partially saturated conditions. To reproduce the ambient condition for the saturation, we inversely determine the infiltration rate of 0.1 mm/yr or less as a reasonable estimate.

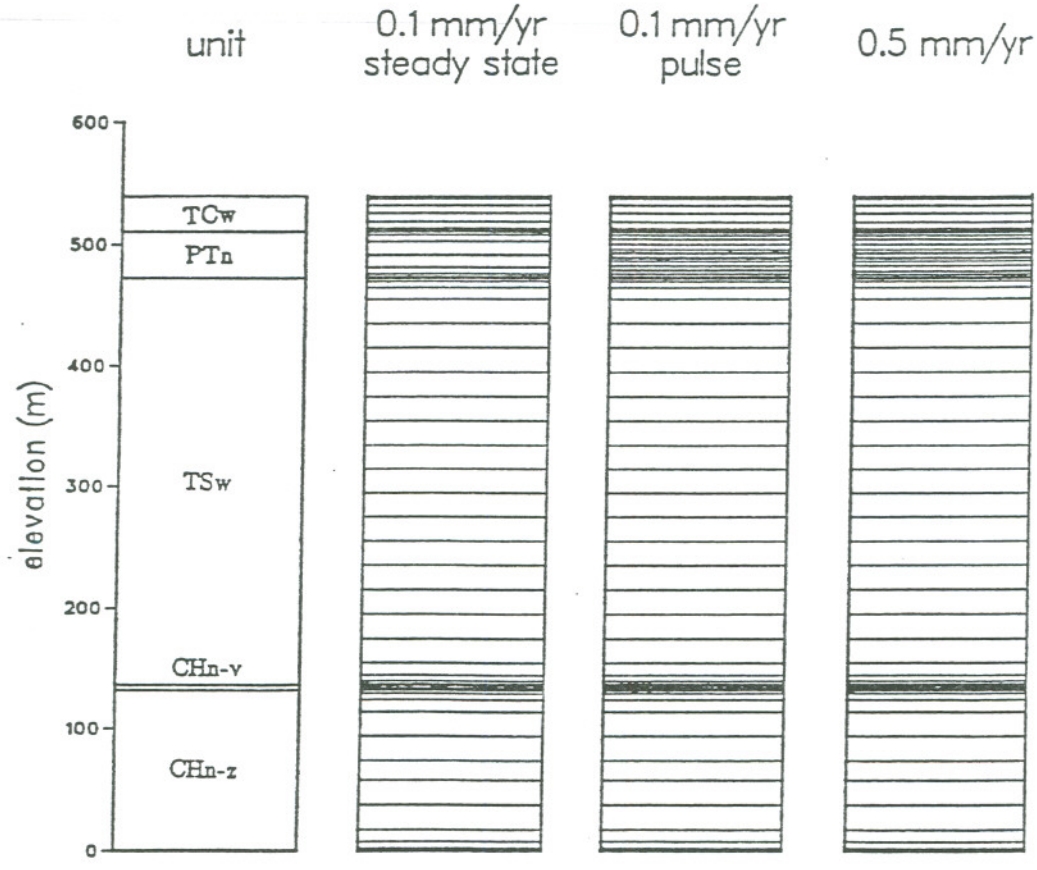

Figure 4.1 Nonuniform grids used for one-dimensional simulations.

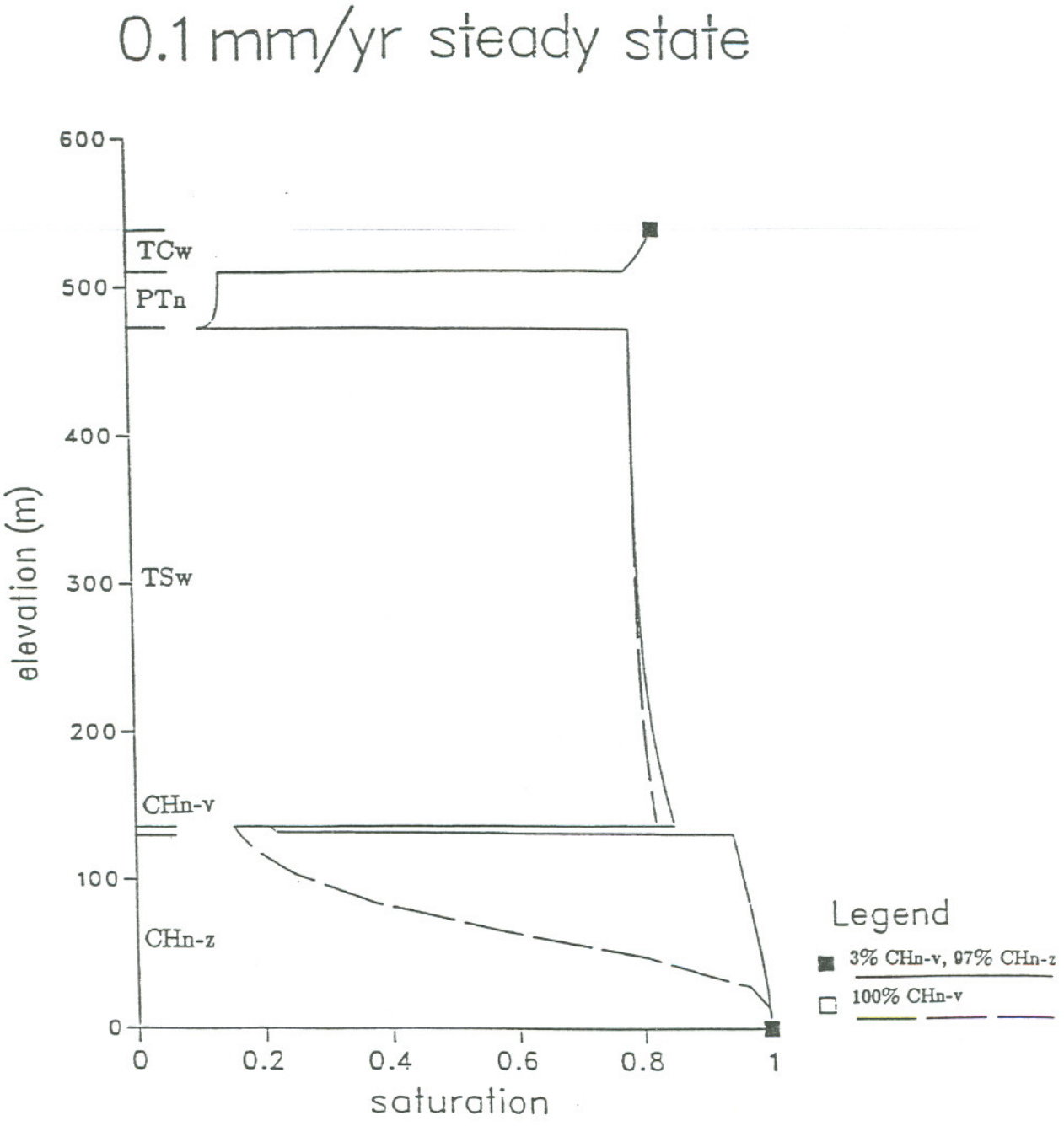

Figure 4.2 Saturation profiles for 0.1-*mm/yr* steady-state infiltration.

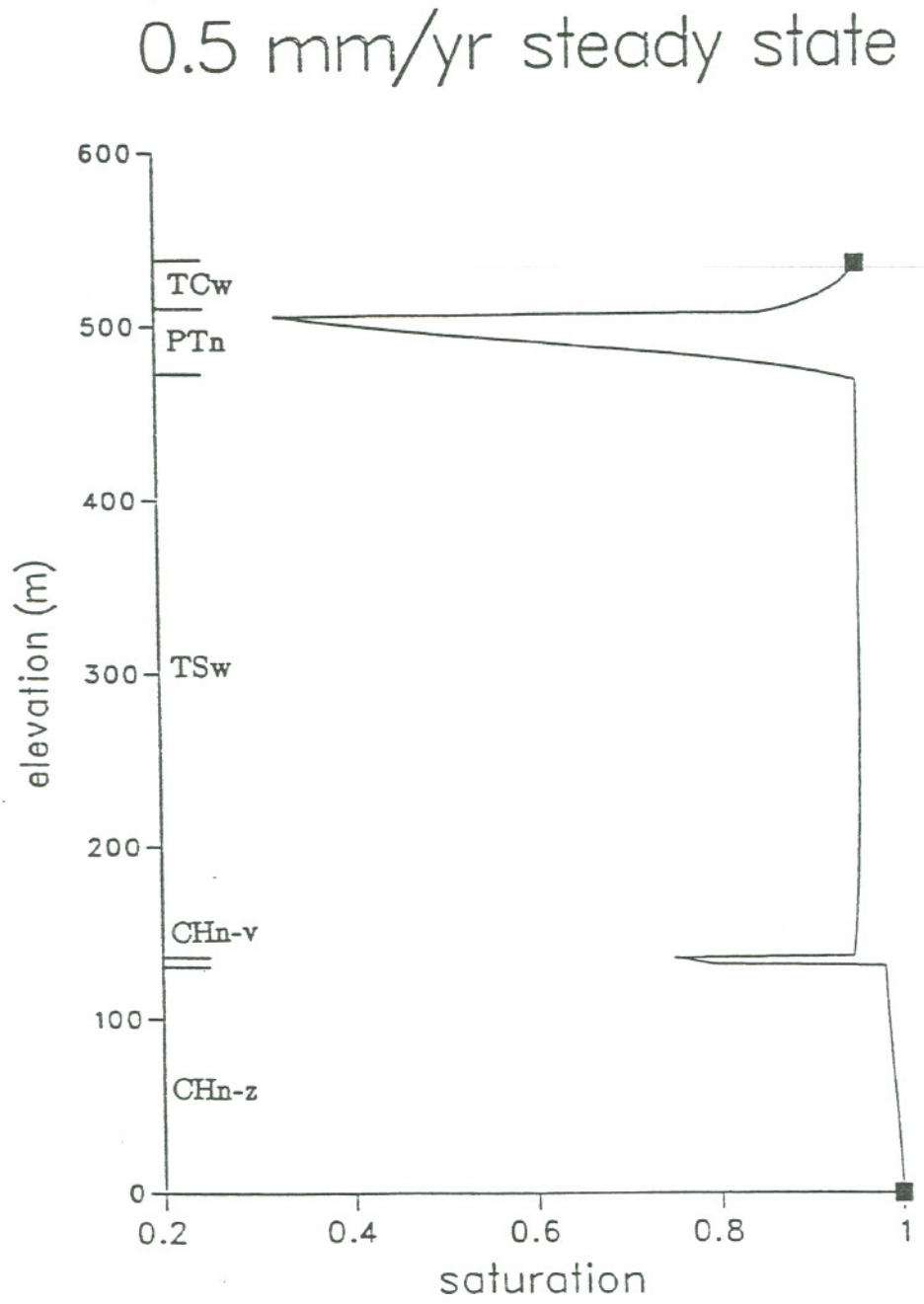

Figure 4.3 Saturation profile for 0.5-*mm/yr* steady-state infiltration.

Because infiltration simulation is usually cast as a boundary value problem with infiltration rate as an input parameter, there is a tendency for reviewers to ask the simple question as to what the effects of infiltration rate changes are. We can indeed create alarmingly fast fracture flows with infiltration over 1 mm/yr which seems to be still a very small infiltration rate. However, the onset of fracture flow is also associated with nearly full saturation in the tuff matrix. At Yucca Mountain, with water table over 500 m deep, tuff units are in partially saturated states and are not on the verge of becoming fully saturated. If we accept the findings that the tuff units are partially saturated with ambient matrix saturation less than one, and that the matrix characteristic curves can be measured in the laboratories with reasonable accuracy, then we can set a limit on the infiltration rate. This is an important but subtle issue which is frequently raised in analyzing the results.

4.3 Welded-Nonwelded Flow Interaction: *Effect of a Thick Unit on Thin Units*

We should point out that the 1985 results have indicated very low saturation values for the nonwelded units (Fig. 4.2). The thick TSw unit at Yucca Mountain is bounded above by a PTn unit and below by a CHn unit. The CHn unit is further divided into an upper vitric subunit and a lower zeolitic subunit. The relative thicknesses of CHnv and CHnz subunits vary throughout the Yucca Mountain and the CHnv is very thin at well USW-G4 (4.6 m or 3% of the total CHn thickness, Ortiz *et al.*, 1985). The calculated saturation values for PTn and for CHnv do not agree with the ambient saturation of 0.56 ± 0.17 for PTn (Sinnock *et al.*, 1987), 0.9 for CHnv, and 0.91 ± 0.06 for CHnz (SNL, 1986). These discrepancies were later reevaluated in 1986 by sensitivity studies for the nonwelded matrix parameters (see Sec. 5.4). The PTn and the CHnv units exhibit low saturations because one particular feature in the matrix characteristic curves of the representative samples chosen for these two units (Peters *et al.*, 1984). For the representative PTn and CHnv matrix curves, most of the saturation changes occur over a relatively narrow pressure range around $-100\,m$. This indicates that the pores in these nonwelded PTn and CHnv representative samples are nearly uniform in size. For the 0.1-mm/yr case the thick TSw unit stablizes the pressure profile to $-150\,m$. With $-150\,m$ more negative than $-100\,m$, most of the pores in these two nonwelded units are drained and the calculated saturations are nearly equal to their residual saturation values.

The thick TSw unit effectively decouples the upper units from the lower units. The saturation, pressure and potential profiles in the upper units are insensitive to profiles in the lower units with or without CHnz below CHnv. The thick TSw unit damps out boundary effects from both the upper and the lower boundaries. This suggests that we may

approximately decouple the studies of the upper units from those of the lower parts. We used this approximation in some of the pulse infiltration studies.

4.4 Approximate Model for Steady-State Profiles: *Elementary Path Integration*

For the transient simulations, the initial conditions used are appropriate steady-state conditions. Computationally, the steady-state conditions were obtained by letting the transient process evolve until changes in conditions are negligibly small. If we can estimate the pressure distribution well, we can obtain the steady-state easily. Before we discuss the transient pulse simulations, we will briefly describe a simple and efficient procedure we use to estimate one-dimensional steady state pressure distribution without using sophisticated numerical codes. For a vertical one-dimensional column with steady-state infiltration flux q everywhere constant, one can simply integrate explicitly the Darcy's equation,

$$q = = -K(h)\left[\frac{dh}{dz} + 1\right], \tag{4.1}$$

from a boundary with given elevation z and pressure head h. At the lower water table boundary $z = z_0 = 0$, we know the pressure head $h = h_0 = 0$. With pressure known at that elevation, we can calculate the corresponding conductivity value $K(h_0)$. The pressure at the next node Δz above the boundary can be estimated from

$$\Delta h = -\left[1 + \frac{q}{K(h_0)}\right]\Delta z \ . \tag{4.2}$$

We can proceed to calculate the conductivity at $h_1 = h_0 + \Delta h$, and calculate the pressure head at the next higher node. If Δz and Δh are small enough so that the conductivity value does not change significantly between two neighboring nodes, we can explicitly calculate the pressure profile from the bottom boundary upward node by node. We have incorporated this simple path-integration procedure in a mesh generator program as a preprocessor for the TRUST code. We used this procedure in the one-dimensional column simulations and also in two-dimensional multi-column simulations in 1986. Simple procedures such as the one outlined above and the code LLUVIA developed at SNL can be useful and practical tools for sensitivity and statistical analyses.

4.5 Response to Extreme Infiltration Pulses: *Damping by Near-Surface Units*

The purpose of the transient simulations is to study the responses of the fractured, porous units to extreme infiltration pulses of high rates and short durations. We first

focus on the upper layers in Yucca Mountain. We investigate possible scenarios with short-transient infiltration pulses having periodic rates much higher than the saturated matrix conductivity. Fig. 4.4 is a discrete fracture-porous matrix model with the PTn unit sandwiched between two 10-m layers of fractured welded tuff. The discrete model for the welded units contains both vertical fracture grids and horizontal connections from the vertical fractures into the matrix. The PTn unit is treated as a composite medium.

For simulations involving infiltration pulses, the initial conditions correspond to the steady-state solution with a constant infiltration source of 0.1 mm/yr on the top TCw node and a sink of 0.1 mm/yr on the bottom TSw node. The infiltration pulses are applied to the fracture continuum at the top. The thickness of TCw unit is greater than 10 m and varies with the topography at Yucca Mountain. At well USW-G4, TCw is approximately 30 m thick. By modeling only the lower 10-m section and applying infiltration pulses to the fractures, we assume that the fractures near the surface in the upper part of TCw have apertures larger than the capillary limit and water can penetrate 20 m of TCw without retention and delay by the tuff matrix. By bypassing the upper portion of TCw, we also neglect the complex near-surface evaporation-transpiration and runoff processes. These processes determine the percentage of precipitation (1) returning upward back to the atmosphere, (2) moving laterally away from the mountain, and (3) infiltrating downward into the ground. We are primarily interested in the effects of net infiltration into the TSw and lower units and the travel time from repository to water table. We assume that the water reaching the top of the lower 10-m section of TCw is the net infiltration.

To systematically study this pulse infiltration problem, first we fix the duration of pulse to 0.2 yr, corresponding to an intense rainfall or snow melt period. The pulses are applied periodically. The periods are chosen to be 1 yr, 5 yr, 50 yr, 500 yr, and 5,000 yr. For the 1-yr pulse, the intensity of the infiltration is 0.5 mm/yr, which corresponds to 1 $yr \times 0.1$ mm/yr, divided by 0.2 yr. For the 5,000-yr pulse, the intensity of infiltration is 2,500 mm/yr, which corresponds to 5,000 $yr \times 0.1$ mm/yr, divided by 0.2 yr. For the case with 5,000-yr pulse, all the infiltration in 5,000 yr is applied to the system within 0.2 yr. After 0.2 yr, the infiltration rate is zero until the start of the next infiltration pulse, 4999.8 yr later. The average infiltration rate over any 5,000-yr period is the same as the constant infiltration rate of the initial steady-state condition.

For the mild and frequent pulses (1 yr, 5 yr, and 50 yr), the matrix was found to always remain partially saturated and the fractures essentially dry. The effects of the pulses are completely damped out in TCw. These results are consistent with the findings of Travis *et al.* (1984) that a slug of water moving through fractures with apertures as

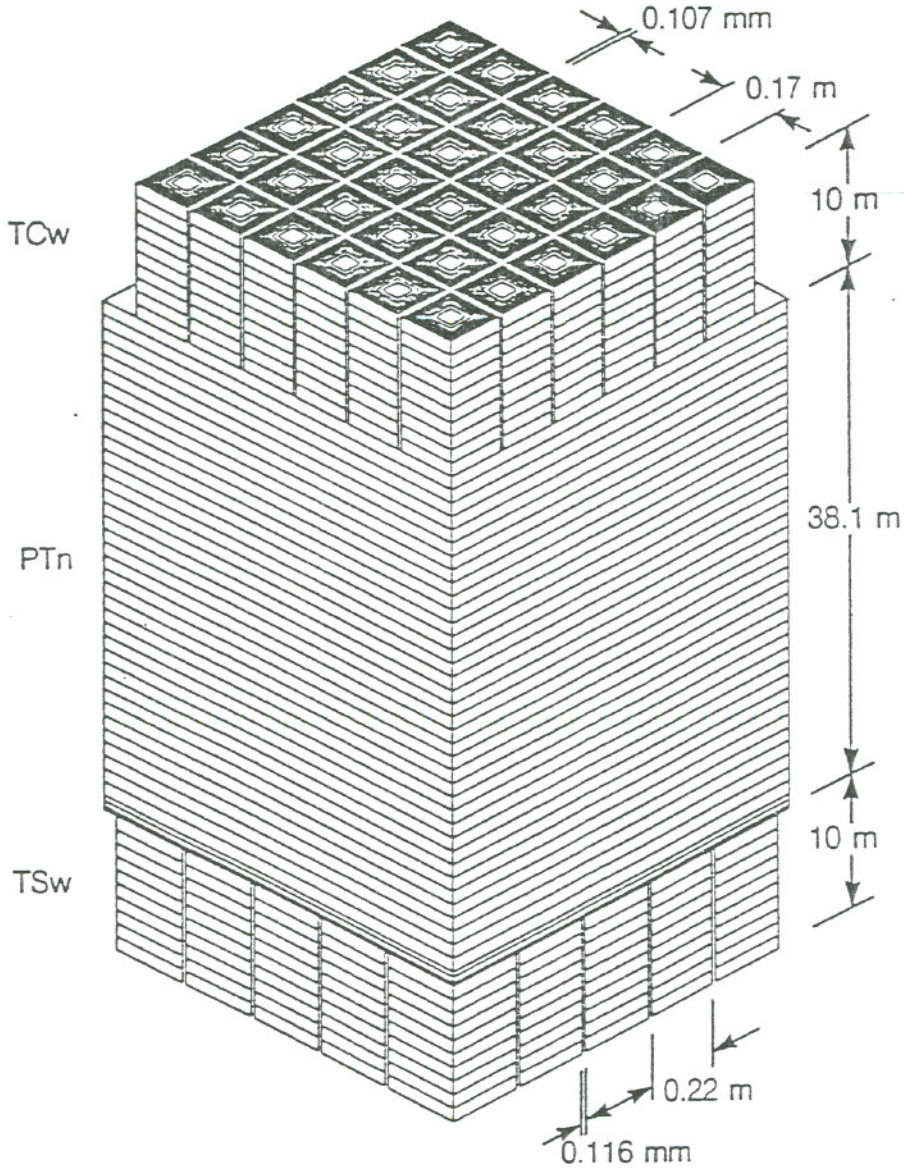

Figure 4.4 Three-dimensional mesh used for studying column response to extreme infiltration pulses.

small as 0.1 mm will be unable to penetrate more than a few meters, at most, through fractured welded tuff with matrix saturations as high as 0.9. Repeated pulsing does not change the capacity of the partially saturated matrix of TCw to absorb all the pulsed water by capillarity. Even for a 50-yr pulse with more than 10 cycles of repeat pulsing, the transient changes are limited within TCw and the matrix remains partially saturated.

For the 500-yr pulse, the intensity of the infiltration pulse (250 mm/yr for 0.2 yr) is high enough to saturate the top 2 m of TCw. Fig. 4.5 illustrates the horizontal saturation profiles within the topmost matrix block of TCw. The pulse is applied to vertical fractures surrounding the four sides of the matrix block. At time $t = 0$, the first (topmost) discrete fracture continuum node starts to receive all the water at a rate corresponding to 250 mm/yr infiltration per unit surface area. Although the water enters the fracture node first, it does not accumulate in the fractures which remain partially saturated. The water is quickly drawn into the matrix by capillarity and distributed nearly evenly throughout the matrix block, which is simulated with 10 nested nodes. The matrix saturations near the matrix-fracture interfaces, 0.085 m (half the vertical fracture spacing of TCw) away from the matrix block center, are only slightly higher than the matrix saturations in the center of the matrix block.

At $t = 0.08\ yr$, the matrix block becomes fully saturated ($S = 1$). The total amount of water infiltrated from $t = 0$ to $t = 0.08\ yr$ is approximately equal to the initial available pore spaces, $\phi(1 - S)$, in the topmost matrix block. For TCw with porosity of $\phi = 0.1$ and an initial saturation of $S = 0.8$, the available pore space in the 1-m thick block will be filled in $0.1 \times (1 - 0.8) \times 1\ m$ divided by 250 mm/yr, or 0.08 yr. As the matrix approaches full saturation and the negative pressure head approaches zero, the saturation in the fractures increases and water moves down through fractures to the next fracture node. The process of horizontal wetting of the second matrix block follows essentially the same fast-suction, even-wetting behavior of the first matrix block shown in Fig. 4.5. Because we can calculate the times required for each block to become fully saturated by the available pore volume and the intensity of pulse without detailed calculations of the horizontal wetting and vertical sharp wetting front movements, the pulse calculations can be greatly simplified as described by Wang and Narasimhan (1986).

The results in Fig. 4.6 for the first cycle for a 500-yr pulse showed that changes in saturation occur mainly in the 10-m section in TCw. Full saturation occurs only in the upper part of TCw during the infiltration period. The pulse effects penetrate slightly into the upper part of PTn but do not reach TSw. Effects of a second cycle are similiar to those of the first cycle. For a 5,000-yr pulse, the 10-m section of TCw is completely saturated during the infiltration period. After infiltration of 2,500 mm/yr over 0.2 yr, the

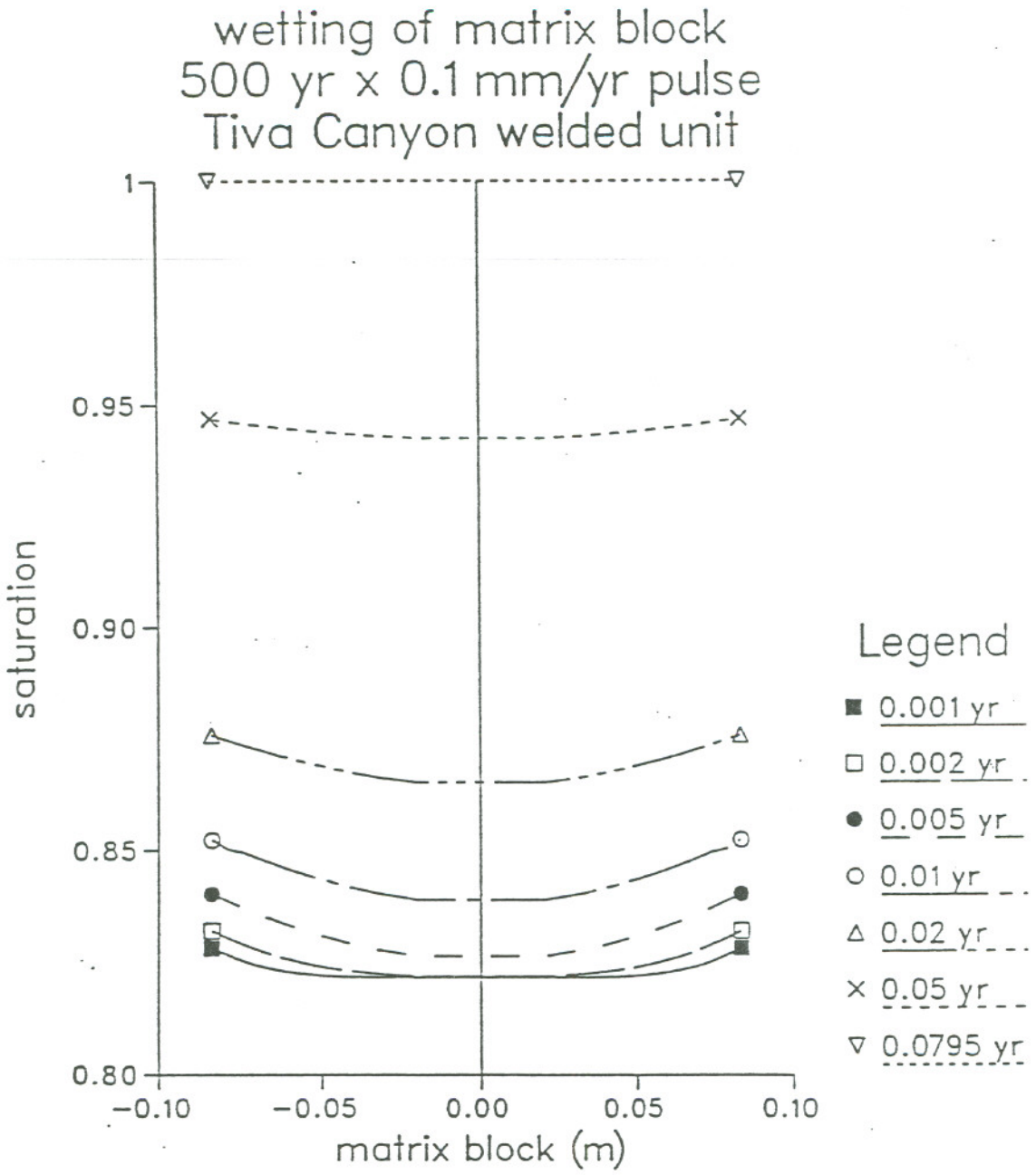

Figure 4.5 Horizontal saturation profiles within matrix block of Tiva Canyon welded tuff unit.

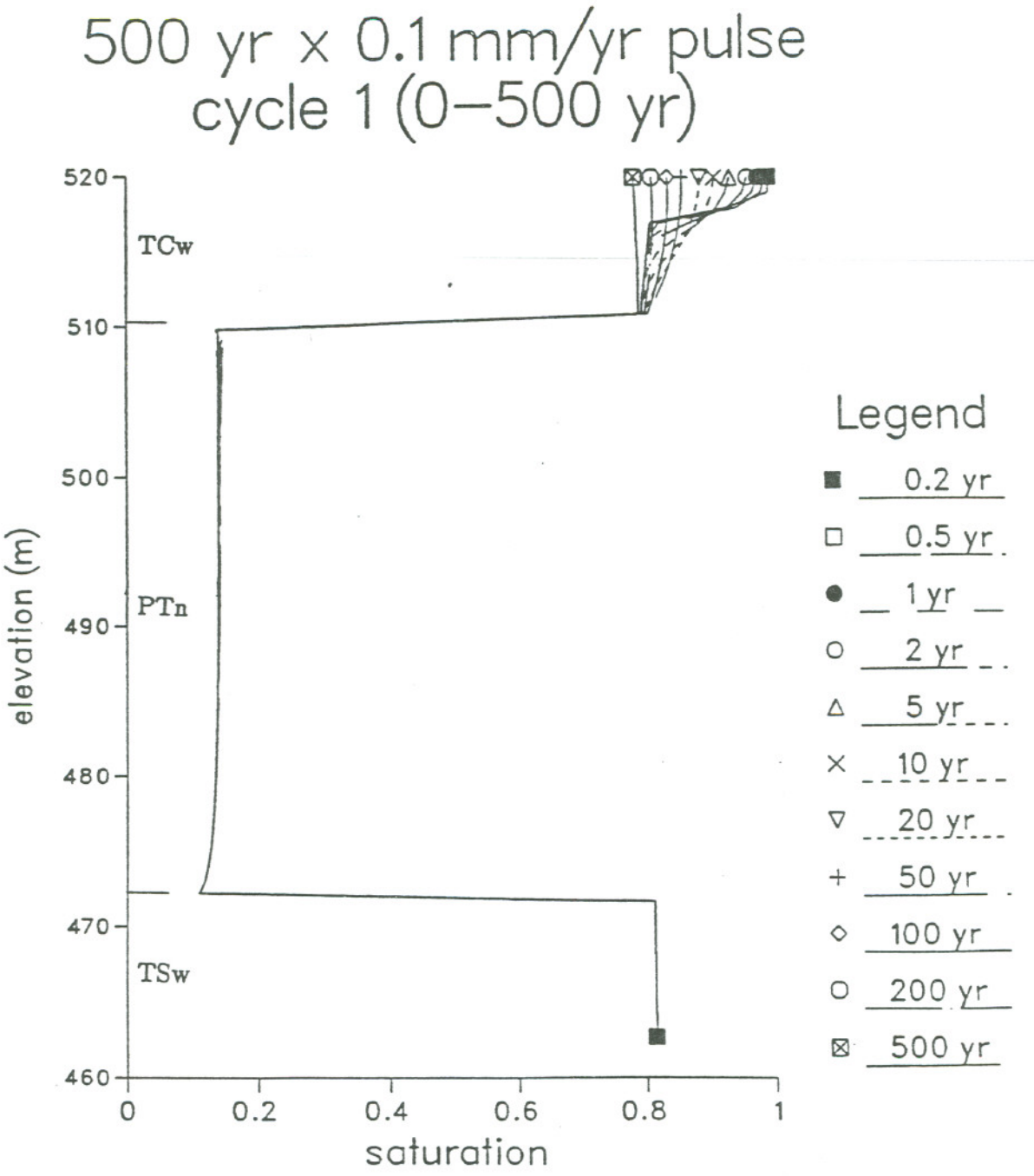

Figure 4.6 Saturation profiles for the first cycle of 500-*yr* × 0.1-*mm/yr* transient infiltration.

infiltrating water moves through PTn and reaches TSw in about 1,000 *yr*. Even for this large pulse, PTn and TSw remain partially saturated. Because the 5,000-*yr* pulse effects do reach TSw, one may question if the lower boundary used in the simulations was perhaps too close to the PTn-TSw interface. We did another set of simulations for the 5,000-*yr* pulse cases using an extended grid.

In the extended grid (see Fig. 4.1), we use the composite-medium model to represent all welded and nonwelded units from the surface to the water table. For the 5,000-*yr* $\times$ 0.1-*mm/yr* pulse case, an infiltration rate of 2,500 *mm/yr* is applied for 0.2 *yr* to TCw below the fully saturated interval which has all its available pore space occupied by infiltrated water. The total amount of water applied to the system in 0.2 *yr* corresponds to all the infiltration in 5,000 *yr*. The results of transient profiles for the first 5,000 *yr* showed that the zone of full saturation does not penetrate the PTn. Similiar results are obtained for additional cycles of pulse infiltration. The damping of the pulse and the penetration of the transient effects for this composite-medium, all-unit simulation agrees with the earlier discrete-fracture, upper-unit results with finer meshes. The effects of the pulsing reach the top of TSw in about 1,000 *yr* and penetrate only the upper part of TSw.

Most of the damping of the pulse occurs in PTn. A large 5,000-*yr* pulse can saturate the matrix, initiate fracture flow, and generate complex flow field in TCw. When the transient effects move into PTn, its large pore volume and highly nonlinear unsaturated characteristics can effectively accommodate and absorb the highly transient and intense water pulses. Only mild perturbations reach TSw. Fig. 4.7 illustrates the propagation and damping of the pulse in PTn. The large mass flux passing through the top TCw-PTn interface at 100 *yr* is damped out as it moves down PTn. The mass flux crossing the lower PTn-TSw interface into TSw is much smaller in magnitude and later in time.

In this extended grid, composite-medium column simulation, we also use a fixed-gradient approximation to estimate the potential lateral flow which may divert a fraction of infiltration from the vertical direction along the column. The results in Fig. 4.7 includes the effects of lateral leakage from anisotropic PTn. The usefulness and limitation of the fixed gradient approximation are discussed by Wang and Narasimhan (1986). Because we went beyond the single vertical column to more accurately estimate the effect of lateral flow in 1986, we will omit further discusion on the fixed gradient approximation.

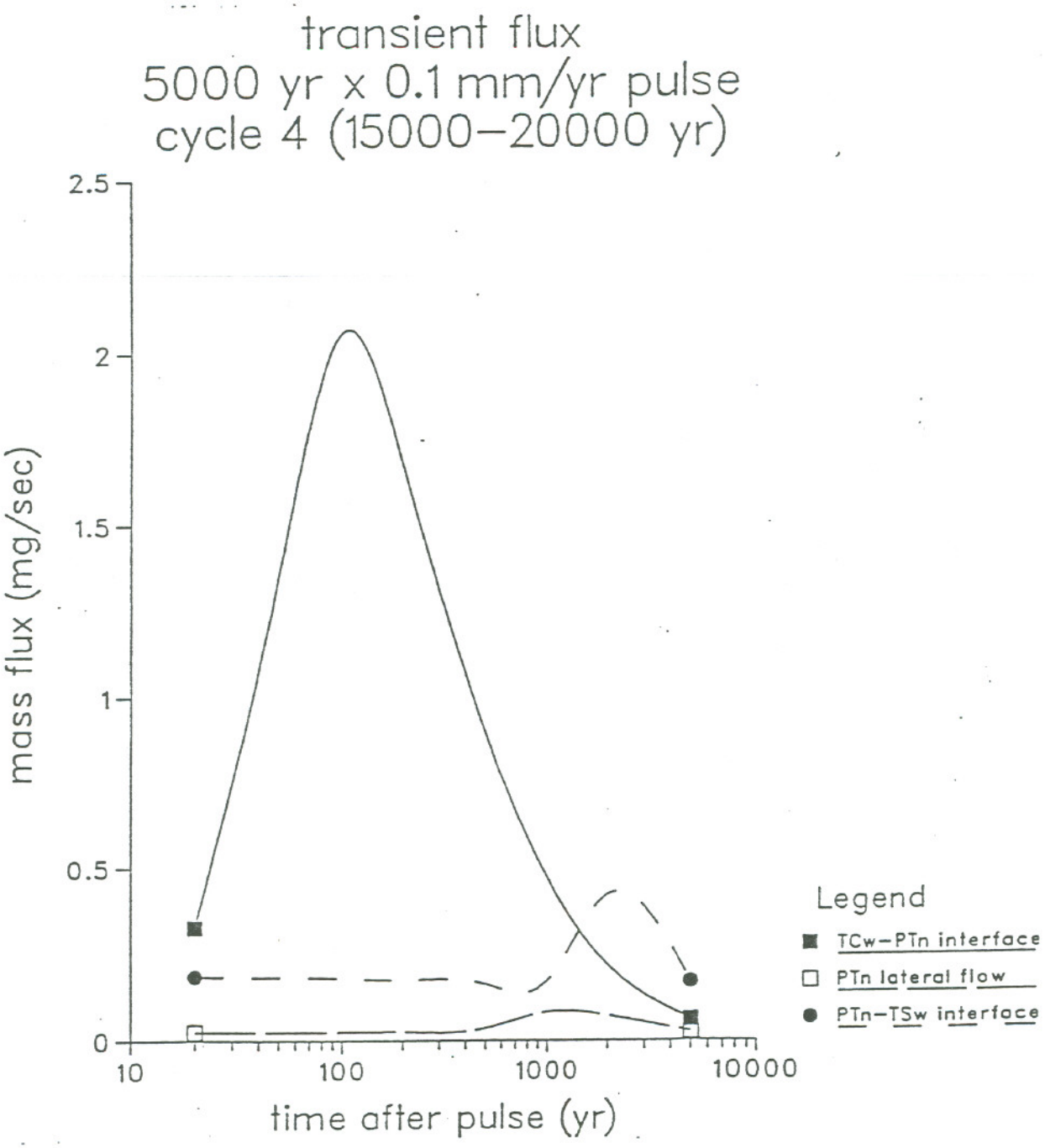

Figure 4.7 Response to 5,000-*yr* infiltration pulse: damping of fluxes within the Paintbrush nonwelded tuff unit.

4.6 Ambient Infiltration: *An Estimate*

Our 1985 results support a conclusion that water flow occurs mainly through the tuff matrix if the average net infiltration rate is less than the saturated conductivity of the matrix. Spatial heterogeneities associated with welded-nonwelded interfaces and temporal variations associated with large infiltration pulses do not change the flow field at TSw significantly. The saturated conductivity of the welded tuff matrix is very small from laboratory measurements. With small saturated conductivity in the range of $1\ mm/yr$, the net infiltration rate is estimated to be $0.1\ mm/yr$ or less so that the simulated saturations agree with the ambient values of 0.6 to 0.8 for the welded units. If the onset of fracture flows could be demonstrated to be unlikely under ambient conditions and under extreme flooding events and the dominant flow direction is vertical, performance assessment could be easily and convincingly carried out for the partially saturated, fractured tuff at Yucca Mountain.

5.0 Distribution of Fluid Near a Fault Zone: *Possibility of Lateral Flow*

In 1986, we extended our models from a single vertical column to a two-dimensional east-west cross section bounded by vertical fault. Yucca Mountain is approximately $2{,}000\ m$ wide. A minor fault, the Ghost Dance Fault (GDF), inside the proposed repository area, will be a major hydrological concern if the fault flow is an important transport mechanism. Without experimental data on the unsaturated characteristics of the fault zone material, we focused our attention in 1986 on the distribution and movement of water in the unsaturated formation near GDF and assessed the potential for water to overcome capillary forces and exit laterally through the formation-fault interface. If water can be diverted away from dispersed vertical flow through the unsaturated formation to concentrated flow through the localized fault zone, the fault zone would likely constitute the fastest flow path from the repository to the water table. On the other hand, the absence of significant fault flow and the dominance of matrix flow will result in long travel time through the unsaturated tuff units.

5.1 Unsaturated Fault: *Different Hydrological Possibilities*

The distribution of fluid flow in the unsaturated zone is governed by the balance between the capillary forces and gravity. The external gravitational force moves the water downward, and the internal capillary forces hold the water in place within the pores. The magnitude of capillary force is inversely proportional to pore size and the heterogeneity of rock pore structure controls distribution and movement of water through

partially saturated formations. Within the meter scale, we have the heterogeneity with tuff matrix blocks separated by discrete fractures. The large fracture openings cannot maintain the strong capillary forces required to hold water within discrete fractures under ambient partially saturated conditions. In the much larger scale covering the mountain width, we have the faults as the heterogeneous feature.

In modeling the hydrology of Yucca Mountain, it is important to assess the impacts of faults that traverse the tuff formation. If faults are barriers to flows, faults will partition the system into separate hydrologic blocks, and we can focus on the study of flows through the interior of blocks. If faults are the main conduits for fluid, then we should focus on the study of fault flows. In saturated systems, we have a clear distinction between these two possibilities. A closed fault is treated as a no-flow boundary, and an open fault as a constant potential boundary if it is connected to a constant-head reservoir. In the latter case, faults may help transport water from a far-removed source or may help remove water to a deeper sink.

In partially saturated systems, we may not have such a clear distinction between an open and a closed fault. Three possibilities can be considered:

- If a fault zone is made up of broken up mass because of brecciation, it might have very coarse openings that can be easily drained. If the openings are dry, there is no fluid to be transported. On the other hand, a dry opening is not a barrier to fluid flow. If water enters the opening, it will have high permeability and offer low resistence for fluid to slide down the walls of large openings (noncapillary flow). Under partially saturated conditions, an ''open'' fault becomes a passive boundary which can transport water if water enters it, but it cannot keep water because there is only very weak capillary force to hold water in large openings.

- If a fault is sealed with gouge material and fine-grained materials, it can retain water and may even attract water with the strong capillary force associated with small openings. On the other hand, small openings have low permeability and cannot be good conduits for transporting fluid. Under partially saturated conditions, a ''closed'' fault becomes a relatively wet zone that passively retains water in nearly static conditions.

- There is a third, remote, possibility that the fault may have a unique combination of saturated and unsaturated characteristics. If the fault material can maintain both strong capillary attractive force and large permeability, then the

fault can pull water away from the formation and transport it quickly away from the system. We cannot rule out the existence of such a unique combination wherein fault flow would control the partially saturated hydrology.

5.2 How to Model the Fault: *The Seepage Face Idealization*

There are no data for the faults to clearly distinguish whether faults in tuff formations have open, closed, or exotic characteristics. In the 1986 study, we did not use material properties to represent the fault. We treat the fault-formation interface as a seepage boundary. It is well known from hillside studies that water will seep out of the formations if the potential at the open face is lower than the potential inside the hill. We assume that the fault is so open that capillary force is zero and the face of the fault behaves like a hillside open surface exposed to atmospheric pressure. We focus on the interior of the formation to determine whether water can overcome capillary forces holding water inside the tuff formation. If water does not exit through the fault-formation boundary, the seepage boundary is essentially a closed boundary. If water remains inside the formations, distribution of fluid flow will be independent of whether the fault is open or closed. The only possibility we do not model is the third possibility, wherein the fault acts as a strong capillary suction sink as well as a high-permeability conduit under partially saturated conditions.

Within the tuff formation, the lateral component of the gravity gradient caused by the tilting of the units has been proposed as a mechanism to divert water laterally (Montazer and Wilson, 1984; Rulon *et al.*, 1986). The stratigraphic units at Yucca Mountain generally tilt eastward at 5° to 7° (Scott and Bonk, 1984). For an average 6° tilting, the tangent of 6° is 0.1 and the external driving force along a lateral direction is 10% of gravity. The partially saturated flow movement is determined by the balance of external force with internal capillary forces. We expect that a weak external force associated with the lateral component of gravity will demand a mild readjustment in lateral variation in saturation, capillary pressure head, and potential to allow the capillary force balances out the external force.

5.3 Stratigraphy, Fracture, Matrix Data: *An Update*

Before we present our results from the two-dimensional cross section models, we briefly discuss several preliminary steps and the systematic approaches we adapt in this study. In 1986, a Reference Information Base (RIB) was developed at SNL. Y. T. Lin of SNL provided us with digitized data for section A-A' from RIB. Section A-A',

illustrated in Fig. 5.1, is one of the sections used by Sinnock *et al.* (1987) in a multi-column unit-gradient vertical-flow stochastic simulation to study the groundwater travel time distributions. To focus on the impact of the GDF on the two-dimensional flow behavior in section A-A', we first repeat the single column simulations with thicknesses of the units corresponding to digitized values at GDF instead of borehole USW-G4 in our earlier studies. We also update matrix (Table 5.1) and fracture (Table 5.2) according to RIB and other new SNL reports. For examples, the average fracture orientation and frequency data from five boreholes (Bauer, 1986) was used instead of the early analyses with USW-G4 data alone. The main difference between the updated results and early analyses is that the horizontal fractures are relatively fewer than the vertical fractures, especially for the welded units. For the matrix, the RIB saturated conductivity values for TSw and CHn matrix are lower than corresponding values in earlier references. With lower saturated conductivity, the calculated saturation in TSw is approximately 5% higher than the 1985 result for the same infiltration of 0.1 mm/yr.

In the RIB (SNL, 1986), the characteristic parameters are not tabulated. We still used the data of Peters *et al.* (1984) for these parameters. Until 1986, we had been focusing attention on understanding fracture characteristics and relied on SNL to provide matrix characteristics. In 1986, we also started to analyze available matrix data. The comprehensive report by Peters *et al.* (1984) contains much data and analyses of laboratory measurements of small intact as well as fractured tuff core samples. In our 1986 simulations, the matrix characteristic curve parameters for TSw1, TSw2, CHnz, and PPw units correspond to the representative samples chosen by Peters *et al.* (1984). For PTn and CHnv, we used two other samples with wider pore size distributions which were also from Peters *et al.* (1984). These two nonwelded units may have multi-modal pore structure as shown in later detailed PTn study by Peters *et al.* (1987). Recent study by P. G. Kaplan of SNL indicates that the CHnv unit is very heterogeneous with many subunits of different characteristics.

5.4 The Ghost Dance Fault: *A Column Profile*

With the use of characteristic curves representing wider pore size distributions in our 1986 study, we were able to yield simulated saturation values closer to measured ambient saturations for the nonwelded units as shown in the GDF column results in Fig. 5.2. The evolution of the 1986 results from the 1985 results represents our efforts to update our data and improve our model predictions. All our model parameters are determined from available data. In 1985 and earlier, we had the wrong impression that the nonwelded units are porous and homogeneous. The predictions of low saturations in

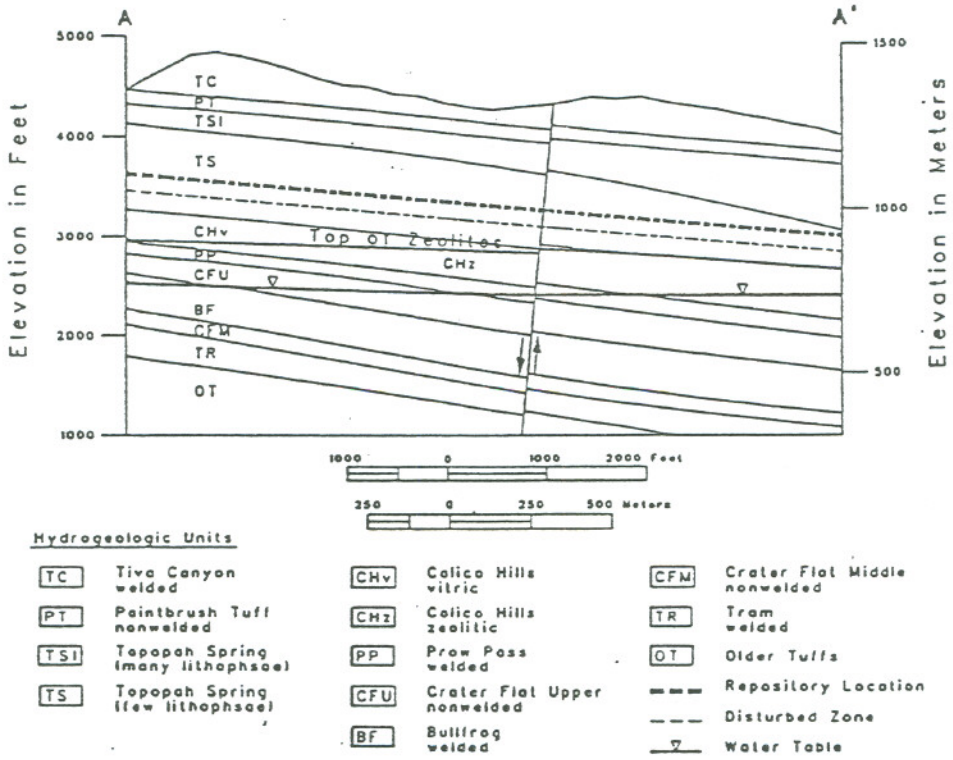

Figure 5.1 Idealized cross section of Yucca Mountain.

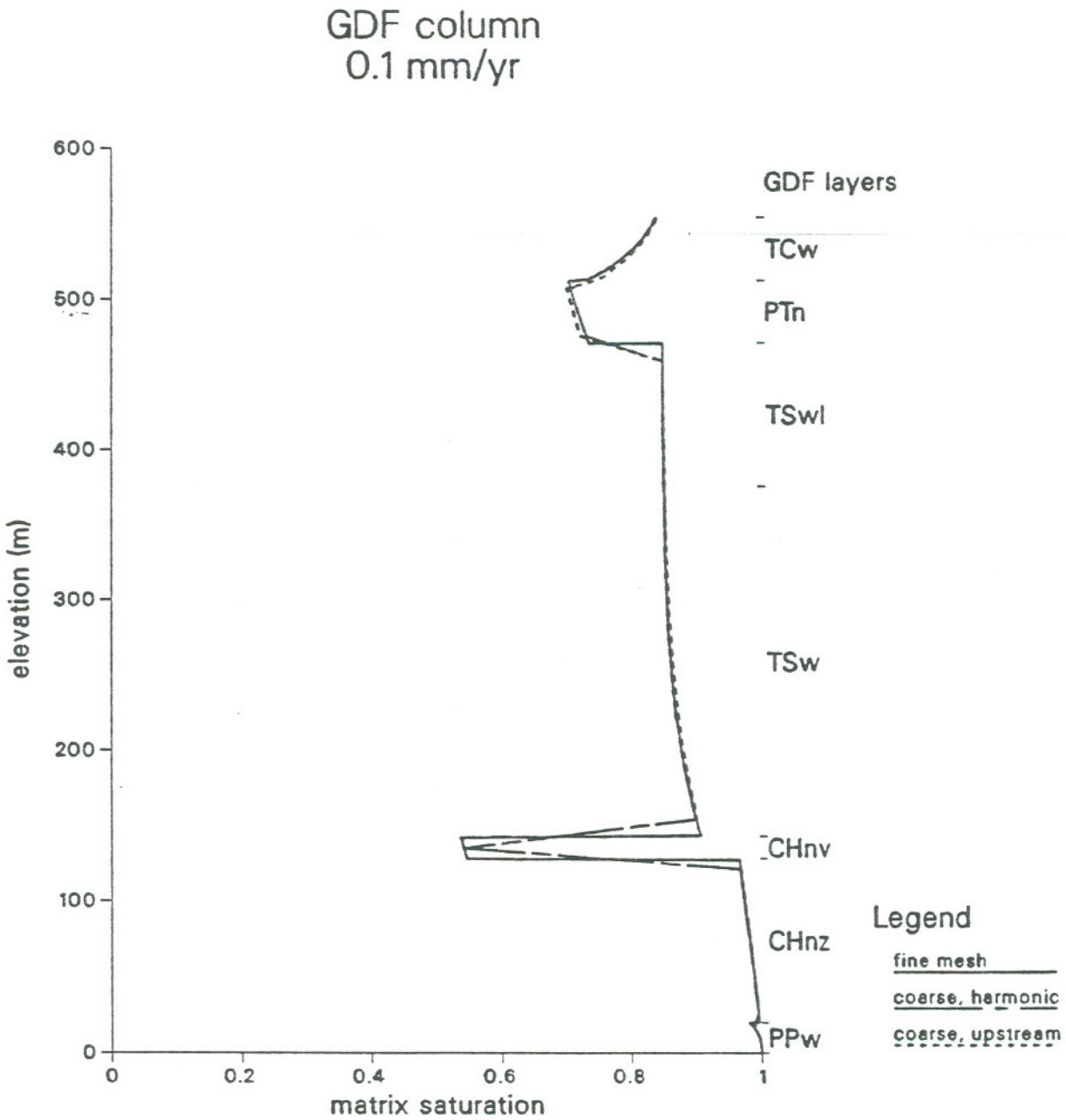

Figure 5.2 Saturation profiles for 0.1-*mm/yr* steady-state infiltration for fine and coarse meshes at Ghost Dance Fault.

Table 5.1 Matrix Properties

Unit	Saturated Permeability k_s (Conductivity [1]) m^2 (mm/yr)	Porosity[2] ϕ	van Genuchten Parameters α[3] ($1/m$)	n[3]	S_r[4]	Compressibility [5] (1/m)
TCw	2.55×10^{-18} (0.789)	0.114	8.21×10^{-3}	1.558	0.002	6.2×10^{-7}
PTn	2.45×10^{-15} (757.385)	0.448	3.05×10^{-2}	1.22	0.040	8.2×10^{-6}
TSw1	2.33×10^{-18} (0.722)	0.143	5.67×10^{-3}	1.798	0.091	1.2×10^{-6}
TSw2	2.33×10^{-18} (0.722)	0.1168	5.67×10^{-3}	1.798	0.091	5.8×10^{-7}
CHnv	3.46×10^{-16} (107.168)	0.3541	4.40×10^{-2}	1.496	0.0852	3.9×10^{-6}
CHnz	1.73×10^{-18} (0.535)	0.3064	3.08×10^{-3}	1.602	0.1211	2.6×10^{-6}
PPw	2.84×10^{-16} (87.742)	0.2557	1.41×10^{-2}	2.639	0.0686	1.5×10^{-6}
CFUn	6.99×10^{-17} (21.637)	0.3239	3.82×10^{-3}	1.9455	0.2282	2.4×10^{-6}
BFw	3.83×10^{-16} (118.439)	0.2391	2.025×10^{-2}	3.2025	0.0584	1.7×10^{-6}

(1) TCw, PTn values from Sinnock *et al.* (1987), other valus from RIB (SNL, 1986) sec. 1.1.4.2

(2) TCw, PTn, TSw1 values from RIB 1.3.1.2.1-4, other values calculated from data in RIB 1.1.8.1 and 1.1.3.1-2. TCw, PTn, TSw1 values from RIB 1.3.1.2.1-4, other values calculated from data in RIB 1.1.8.1 and 1.1.3.1-2.

(3) from Peters et al. (1984) with sample code: TCw:G4-1, PTn:G4-2, TSw1:G4-6, TSw2:G4-6, CHnv:GU3-15, CHnz:G4-11, PPw:G4-18, CFUn:G4-19/20, BFw:G4-21/22.

(4) TCw, PTn values from Peters *et al.* (1984), other values from RIB 1.1.3.1-2.

(5) Nimick *et al.* (1984).

Table 5.2 Fracture Properties

Unit	Bulk Saturated Permeability (Conductivity [1]) m^2 (mm/yr)	Fracture [2] Spacing d (m) Vertical	Horizontal	Effective Aperture $\bar{b}$ (mm) Vertical	Horizontal	Discrete Fracture Permeability k_s (m^2) Vertical	Horizontal
TCw	1.18×10^{-12} (3.65×10^5)	0.18	0.42	0.109	0.144	9.87×10^{-10}	1.72×10^{-9}
PTn	2.42×10^{-13} (7.5×10^4)	1.02	1.12	0.114	0.118	1.09×10^{-9}	1.15×10^{-9}
TSw1	1.18×10^{-12} (3.65×10^5)	0.21	1.26	0.114	0.208	1.09×10^{-9}	3.59×10^{-9}
TSw2	1.18×10^{-12} (3.65×10^5)	0.21	1.26	0.114	0.208	1.09×10^{-9}	3.59×10^{-9}
CHnv	2.42×10^{-13} (7.5×10^4)	2.12	4.49	0.146	0.187	1.77×10^{-9}	2.91×10^{-9}
CHnz	2.42×10^{-13} (7.5×10^4)	2.12	4.49	0.146	0.187	1.77×10^{-9}	2.91×10^{-9}
PPw	1.18×10^{-12} (3.65×10^5)	1.49	2.73	0.219	0.268	4.01×10^{-9}	6.00×10^{-9}
CFUn	2.42×10^{-13} (7.5×10^5)	5.07	4.49	0.195	0.187	3.16×10^{-9}	2.91×10^{-9}
BFw	1.18×10^{-12} (3.65×10^5)	0.393	3.39	0.141	0.289	1.65×10^{-9}	6.94×10^{-9}

Unit	Contact[4] Cutoff Aperture b_c (mm) Vertical	Horizontal	Aperture[4] Distribution Parameter β (mm^{-1}) Vertical	Horizontal	Fracture [5] Surface Contact Area ω	Discrete[6] Fracture Compressibility ($1/m$)
TCw	0.010	0.014	24.8	18.8	2.8%	1.32×10^{-6}
PTn	0.027	0.028	21.7	21.1	11.8%	1.90×10^{-7}
TSw1	0.027	0.050	21.7	11.9	12%	5.60×10^{-8}
TSw2	0.027	0.050	21.7	11.9	12%	1.20×10^{-7}
CHnv	0.041	0.053	16.6	13.0	15% (no zeolite)	2.80×10^{-8}
CHnz	0.132	0.169	12.7	9.91	50% (w. zeolite)	2.80×10^{-8}
PPw	0.130	0.159	9.53	7.79	35%	1.20×10^{-7}
CFUn	0.115	0.110	10.7	11.2	35%	2.80×10^{-8}
BFw	0.083	0.170	14.9	7.24	35%	1.20×10^{-7}

(1) Representative values from well J-13, Thordarson (1983); Sinnock *et al.* (1987).

(2) Derived from average fracture spacings and orientation data in well USW G-1, UE-25a#1, USW GU-3/G-3, USW G-4, see Bauer (1986).

(3) Derived from bulk saturated permeability and fracture spacings, assuming two vertical sets and one horizontal fracture set.

(4) Derived with gamma distribution from permeability and surface contact area for rough-walled fractures, Wang and Narasimhan (1985).

(5) Assumed to be equal to the fraction of fracture surface coated with clay, calcite, and/or zeolite, in well USW G-4, Spengler and Chornack (1984).

(6) Peters *et al.* (1984).

nonwelded units using matrix characteristic curves with narrow pore size distribution bothered us. In 1986, new studies and observations suggested that the nonwelded units are heterogeneous, and the updated predictions reduced the discrepancies between model predictions and experiment measurements. We expect that the continuing process of cross checking between models and measurements will validate the models for performance assessment.

Before implementing two-dimensional grids, we conducted tests with several one-dimensional cases to study the effects of mesh refinement and spatial averaging of permeability on the solution. Our calculations showed that we did not introduce any serious errors because of our choice of the mesh refinement or the method of spatially averaging permeability.

5.5 Multi-Column Models: *Fluid Redistribution within the Tuff Formation*

To focus on the effects of eastern tilting of the units and the presence of GDF on the two-dimensional flow behavior, we modeled the region west of GDF, treating GDF as a seepage boundary. The location of the western boundary was treated as variable ranging from 190 m to 648 m. Five meshes were used in the two-dimensional studies to evaluate the effects of mesh refinement and the effects of system boundaries. Fig. 5.3 is a 9-column, slanted mesh used in the 648-*m* wide model. Our results showed that numerical uncertainties associated with lateral mesh refinements were small. With mild variations in saturation, pressure, and potential in the lateral direction, coarse gridding can be used to generate acceptable results (Wang and Narasimhan, 1988).

The two-dimensional simulations showed that the eastern tilting of the units results in slightly higher matrix saturations in the eastern side of the cross section. Consequently, pressure heads along eastern columns closer to the seepage boundary are slightly higher than pressure heads along western columns. Pressure head values remain negative and deviations of two-dimensional results from one-dimensional one-column results were found to be small. The equal potential lines in most units are nearly horizontal, as illustrated in Fig. 5.4. From matrix saturation, pressure head, and potential results of the two-dimensional multi-column model, tilting of the units changed vertical distributions very little.

The matrix saturation and pressure head values of the nodes in the middle of TSw2 unit were found to be higher in the east than in the west. From saturation differences between the easternmost and westernmost columns, we calculated that the rate of linear saturation change varied from 5 to 17%/km, depending on the number of columns in the model; the smaller the number of columns, the larger the change. From results of the 9-

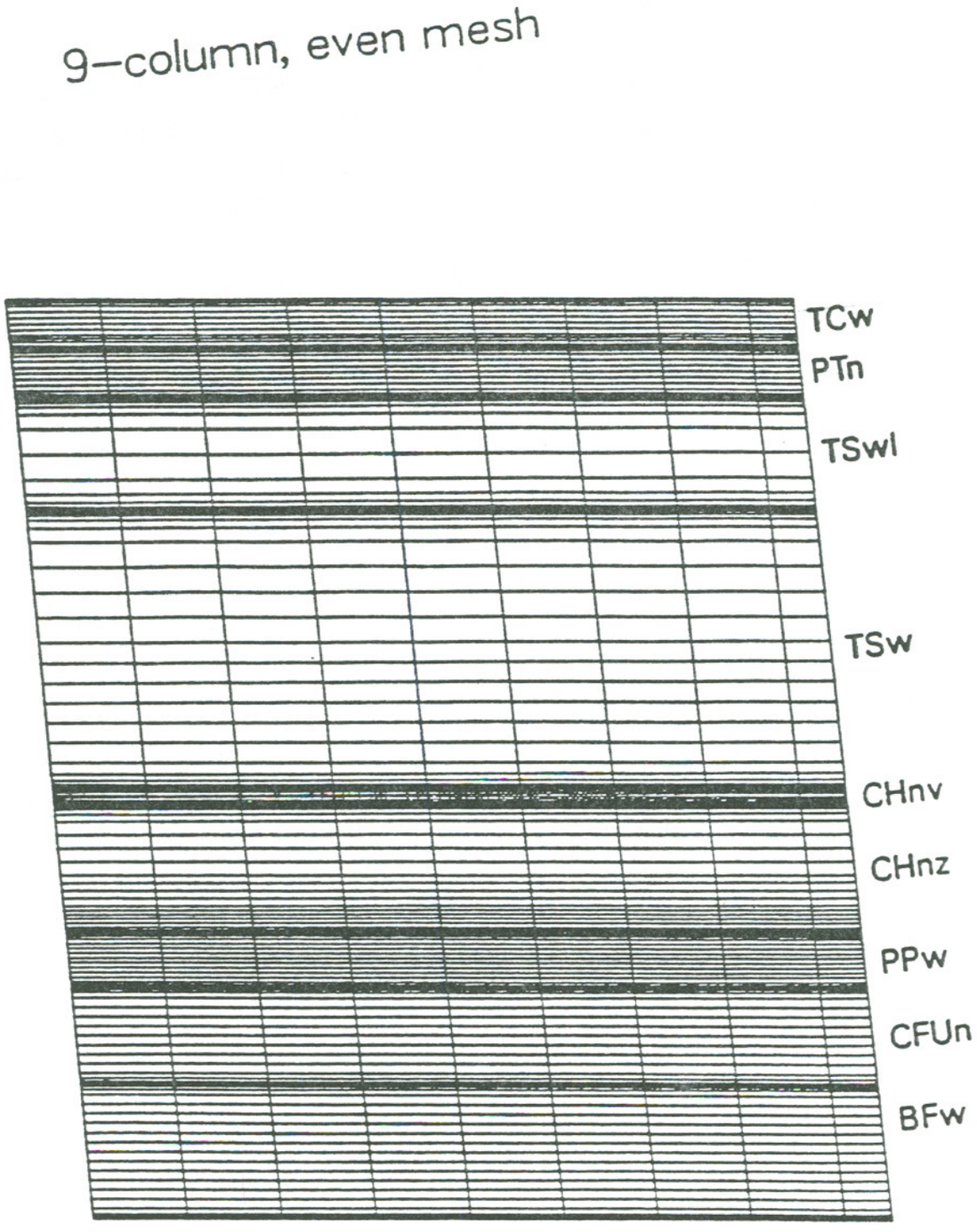

Figure 5.3 Two-dimensional grid for vertical and lateral flow model.

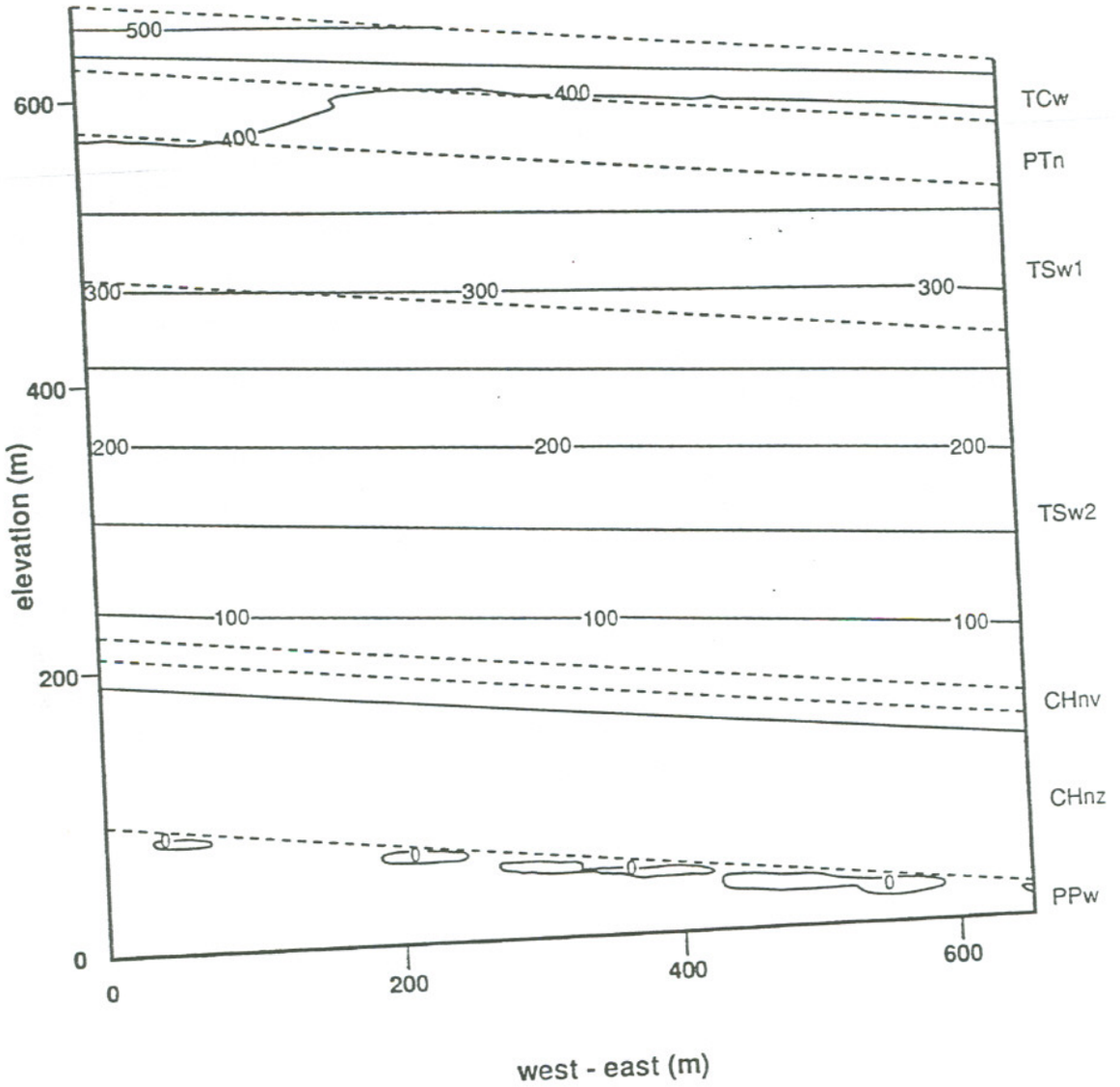

Figure 5.4 Potential distribution in a 645-*m* section west of Ghost Dance Fault.

column, 648-*m* section model, we can also estimate wider section upper bounds for the change rate of other variables: pressure head: 60 *m/km*; potential, 44 *m/km*; vertical Darcy velocity, 0.085 *mm/yr/km*; and vertical matrix pore velocity, 0.79 *mm/yr/km*.

5.6 Vertical and Lateral Flow: *Nonwelded Unit as Lateral Channel for Fluid Redistribution*

Calculations using the 9-column, 645-*m* model showed that vertical Darcy velocity along columns closest to the GDF boundary is approximately 25% higher than the 0.1-*mm/yr* infiltration rate; flow in column 5, in the middle, is approximately 0.1 *mm/yr*; and flow in column 9, away from the GDF boundary, is approximately 25% lower than 0.1 *mm/yr* (Fig. 5.5). From the vertical matrix velocity, we can calculate the travel time from the repository to the water table. For the 9-column, 648-*m* model, the travel time along the easternmost column is approximately 50% shorter than the travel time along the westernmost column. If the width of the section is doubled, we expect the groundwater travel time to vary in the range of a factor of 2 from different points in the repository. The fluid flow redistribution effects induced by the tilting units are unlikely to introduce orders-of-magnitude changes in travel time for the 0.1-*mm/yr* infiltration cases.

In slanted meshes used in this study, lateral fluxes between two neighboring columns are evaluated from both pressure and elevation differences of neighboring nodes. Because elevation differences are included in flux calculations, a lateral velocity is not a horizontal velocity. Lateral velocities measure flux magnitudes along layers parallel to tilted interfaces. A careful evaluation of the lateral fluxes between the columns showed that lateral Darcy velocities are smaller than vertical Darcy velocities.

When it does occur, lateral flow occurs mainly within the PTn unit. Lateral flow is the mechanism to redistribute vertical infiltration by channeling water from the west to the east, so that vertical Darcy flux in the east is higher than in the west, and saturation is higher in the east than in the west. Magnitudes of lateral flow were found to be higher in the middle of the cross section than near the side boundaries (Fig. 5.5). In other words, water does not exit through the fault-formation boundary. The lateral gravity gradient associated with tilting of interfaces cannot overcome capillary forces that hold water in partially saturated formations.

5.7 Onset of Seepage Flow: *A Hypothetical Nearly-Saturated System*

For the 0.1-*mm/yr* cases, representing the ambient saturation conditions, no seepage flow occurs through the formation-fault boundary. The onset of seepage flows is

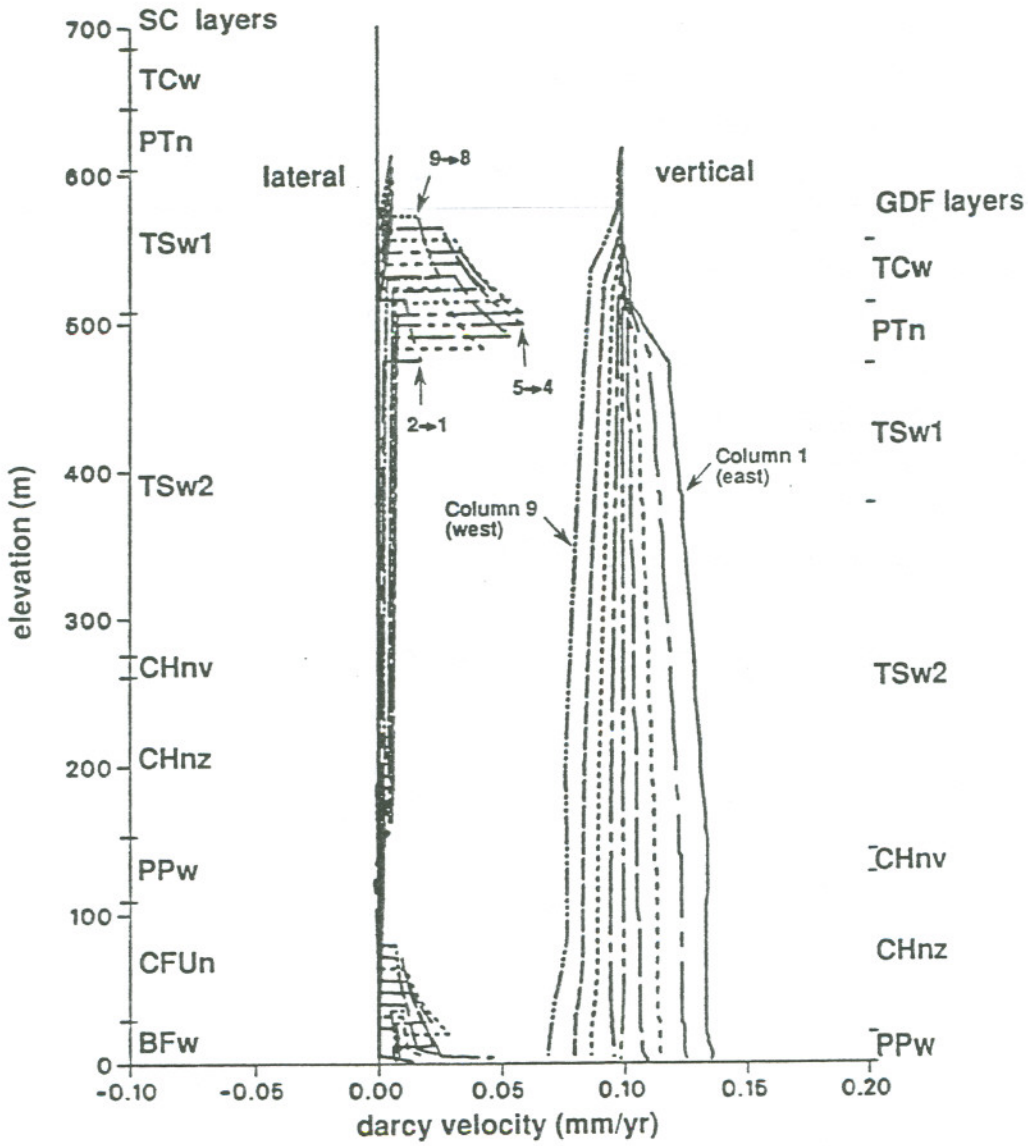

Figure 5.5 Darcy velocity profiles for vertical and lateral flows with 0.1-*mm/yr* steady-state infiltration.

simulated in the 0.5-*mm/yr* infiltration cases. With 0.5-*mm/yr* infiltration, the tuff units are nearly saturated and seepage flow was found to occur only at the CHnv-CHnz interface for a 5-column, 343-*m* section model with 0.5-*mm/yr* infiltration. In terms of mass fluxes, we have approximately 8% lateral diversion; i.e., 8% of infiltration on the ground surface exits at the CHnv-Chnz interface out of the two-dimensional section, and the remaining 92% moves down to the water table. For this case, the amount of water flux driven by the lateral gravity gradient parallel to tilted interfaces is larger than the matrix saturated conductivity, and fracture flows are initiated at the seepage exit point. With the material properties used in the 1986 study, we observed seepage flow only in the CHnv-CHnz interface for the 0.5-*mm/yr* cases. If we use different characteristic curves for the units, we may also generate results with seepage flow in other units if the units have pressure values nearly zero and redistribution effects are strong enough to increase pressure values to nonnegative ranges. We should reemphasize that saturation and pressure distributions with 0.5-*mm/yr* infiltration do not represent ambient partially saturated conditions at Yucca Mountain. Therefore, predictions of the existence of seepage flows in the 0.5-*mm/yr* cases were mainly modeling exercises.

5.8 Ambient Flow Field: *Effect of Stratigraphic Tilting*

Based on results with two-dimensional cross section models for alternating layers tilted toward the seepage boundary on the east, we may conclude the following for 0.1-*mm/yr* infiltration:

- Eastern tilting of units contributes to redistribution of flow, resulting in higher saturations and higher vertical velocities in the eastern side of a block bounded by faults. This redistribution effect is approximately proportional to cross-section width.

- Nonwelded units are major channels in redistributing vertical infiltration. Magnitudes of lateral flow are higher in the middle of the cross section than near side boundaries.

- Tilting itself is not a strong enough mechanism to induce drastic changes in saturation, pressure, and potential distributions to drive flows into fault zones.

The mild lateral variations in saturation, pressure, and potential indicate that one-dimensional results are fairly good estimates of ambient conditions. The lateral tilting mechanism is a second-order perturbation that does not globally change the downward,

gravity-driven flow patterns. So long as fluid flow remains inside partially saturated units, redistribution effects caused by tilting will not introduce order-of-magnitude differences in fluid transport predictions. If the system is on the verge of making a phase transition from partially saturated to fully saturated condition, as in the case of 0.5-*mm/yr* infiltration, the lateral tilting mechanism can perturb the system and change a fraction of fluid flow from dispersed slow flows percolating through the formations to concentrated fast flows rushing down the faults. If fault flow is important, the early arrival portion of the groundwater travel time distributions may be controlled by the fault characteristics. For ambient conditions with large negative pressure values in all partially saturated units, it is unlikely that the lateral tilting mechanism can perturb the pressure and saturation field significantly enough to overcome negative capillary forces holding water in formations and change groundwater travel time distributions drastically.

6.0 Statistical Analyses of Tuff and Soil Data: *Variability of Hydrological Parameters in Different Media*

In 1987, we systematically analyzed the hydrological parameters of tuff matrix and fractures. Because many hydrological parameters are determined from microscopic pore structures, together with fluid properties and rock textures, correlations among different parameters may manifest themselves in the measured values. To elucidate the parameter correlations, we compile and compare saturated and unsaturated parameters of tuff matrix with watershed soil data. There are two reasons for us to analyze the tuff matrix and soil data in detail. We are concerned with the proper range of the fault and fracture parameters which are difficult to measure but may control the system response in the fractured tuff formations. Also the determination of groundwater travel time distribution requires statistical quantification of model parameters. We conclude this section with a discussion of the application of fractal theory to the analysis of rough-walled fractures and heterogeneous media and the relationships between fractal theory and geostatistics.

6.1 Parameter Distributions: *Difference between Tight Tuff Matrix and Permeable Soil*

Because many unsaturated flow models were developed in soil studies, it is important to analyze the similiarity and difference between soil and tuff rock characteristics. Some of the soil data have also been used to represent fractures and faults in tuff formations. We compared parameter distributions of tuff matrix data with watershed soil data. Specifically, the tuff matrix data are from the SNL studies by Peters *et al.* (1984) and Klavetter and Peters (1987), fitted with the van Genuchten (1980) model. The watershed

data are from the United States Department of Agriculture study by Holtan *et al.* (1968), fitted by Panian (1987) of Desert Research Institute, also with the van Genuchten model.

In the van Genuchten model, the dependence of effective saturation S_e on suction pressure head h is described by the equation,

$$S_e(h) = [1 + (|\alpha h|)^n]^{-1+\frac{1}{n}}. \tag{6.1}$$

Figure 6.1 compares the van Genuchten curves with the popular Brooks and Corey (1966) model,

$$S_e(h) = \begin{cases} 1 & \text{if } |\alpha h| < 1 \\ |\alpha h|^{-\lambda} & \text{if } |\alpha h| \geq 1 \end{cases}. \tag{6.2}$$

In the range of large suction, the van Genuchten equation is asymptotically equivalent to the Brooks and Corey power function with the pore-size distribution index $\lambda = n - 1$. The inverse of the parameter α, $|h_{ae}| = \alpha^{-1}$, is frequently referred to as the air entry value or bubbling pressure in the soil literature. This is one interpretation for the parameter α or h_{ae}. When suction pressure head h overcomes the air entry pressure h_{ae} ($|h| \geq |h_{ae}|$), air enters the pores and water flows out of the medium to initiate desaturation. This interpretation is based on the cutoff separating the $S_e = 1$ saturated region from the $S_e = |\alpha h|^{-\lambda}$ desaturated region in the Brooks and Corey model. Another interpretation for α is to treat it as a scaling parameter. The saturation depends on αh together and not on α and h separately. Characteristic curves of soils with different α, but same λ, can be scaled into one curve. Therefore, we refer to α as the air entry scaling factor. If flow channels are represented by capillary tubes, we can define air entry radius by the capillary equation

$$r_{ae} = -\frac{2\gamma}{\rho g h_{ae}} = \frac{2\gamma}{\rho g}\alpha. \tag{6.3}$$

With surface tension γ, water density ρ, and gravitational acceleration g as constants, r_{ae} is proportional to α. We can treat the air entry radius r_{ae} as a parameter equivalent to the air entry scaling factor α.

We have analyzed the pore-size distribution index and the air entry scaling factor, together with saturated permeability, porosity, and residual saturation. Detailed analyses of the distributions and the correlations of soil and tuff parameters are in the report by Wang and Narasimhan (1989). In this review, we focus on two parameters: the saturated permeability and the unsaturated air entry scaling factor. Fig. 6.2 compares the distributions of log air entry scaling factor of watershed soils with tuff matrix. The important

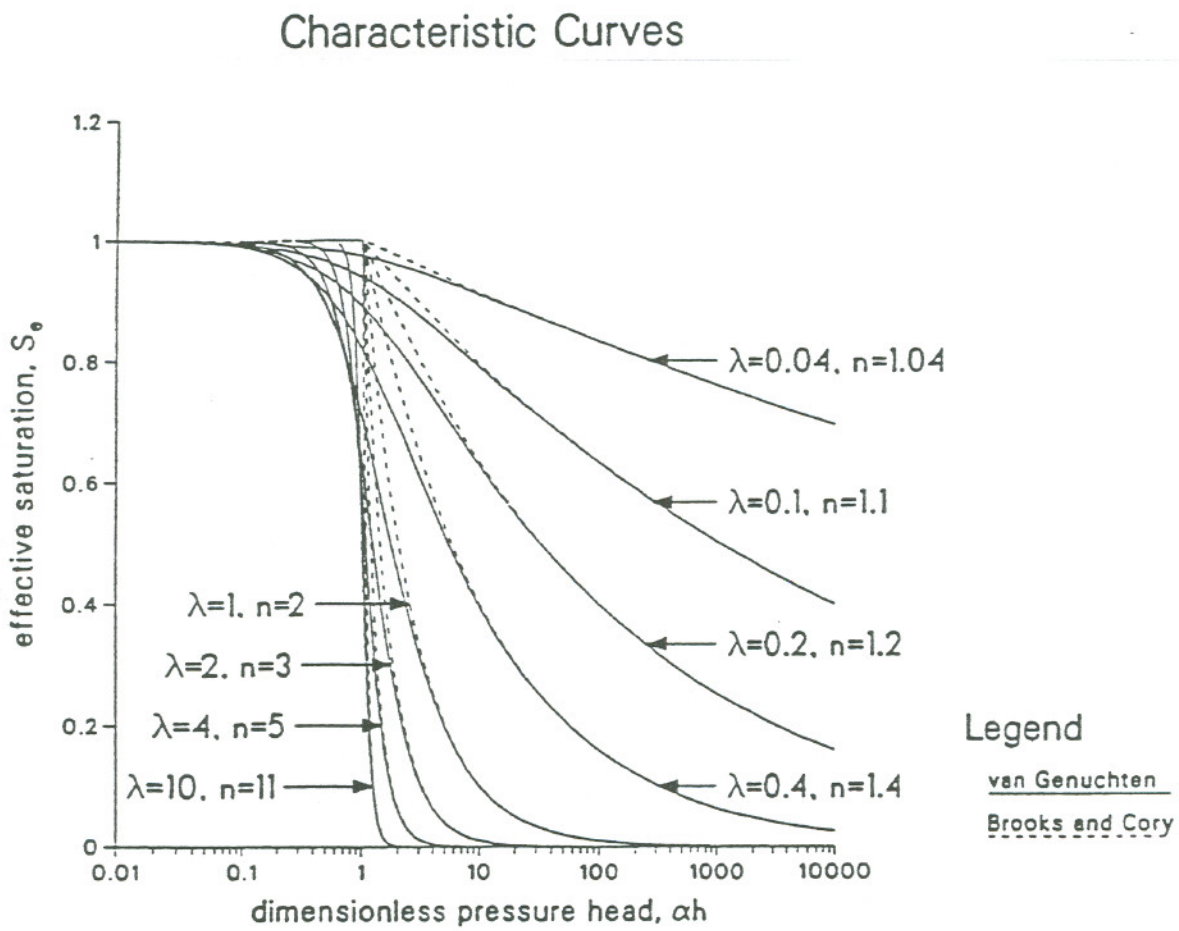

Figure 6.1 Comparison of characteristic curve of the van Genuchten model and the Brooks-Corey model.

observation is that the average air entry scaling factor for watershed soils is two to three orders of magnitude larger than both the welded tuff and nonwelded tuff. Because air entry radius is proportional to air entry scaling factor, the order of magnitude differences simply indicate that the soils have much larger pores that can be easily desaturated and tuff matrix have smaller pores that are more difficult to desaturate. Fig. 6.3 shows that the average saturated permeability for watershed soils is five to seven orders of magnitude larger than those for welded/zeolitized tuffs.

6.2 Parameter Correlations: *Relationship between Hydrological Parameters and Flow Geometry*

The correlation between saturated permeability and air entry radius based on mean values of these parameters for different soil texture categories and different tuff stratigraphic units are plotted in Fig. 6.4. If a porous medium is represented by uniform circular tubes with radius r_{ae}, the maximum permeability of this idealized air entry tube model is

$$k_{\max} = \frac{r_{ae}^2}{8} . \tag{6.4}$$

Fig. 6.4 shows that the correlation between saturated permeability and air entry radius follows approximately the square functional dependence when soil data are compared with welded/zeolitized tuff matrix data. Wang and Narasimhan (1989) discuss other data sets in the literature on this and other parameter correlations.

In the literature, the correlation between permeability and porosity has been extensively studied. If the saturated permeability does correlate with other hydrological parameters, it probably correlates better with air entry radius than with porosity. Physically, this correlation makes more sense with air entry radius than with porosity. The saturated permeability measures the flow through connected channels in a medium. The air entry radius measures the desaturation of fluid from the interior of medium through connected channels to the outside. Both parameters do not depend on dead end pores with stagnant fluid isolated from the connected channels. The porosity measures the volume of both connected channels and dead end pores. There is considerable interest in the literature on the permeability-porosity relationship. The correlation between permeability and air entry radius, observed in soil and tuff matrix data, also deserves attention in natural geological medium studies. Practically, this correlation of saturated permeability can be more easily demonstrated with air entry radius than with porosity. The air entry radius, or equivalently the air entry scaling factor, varies over several orders of

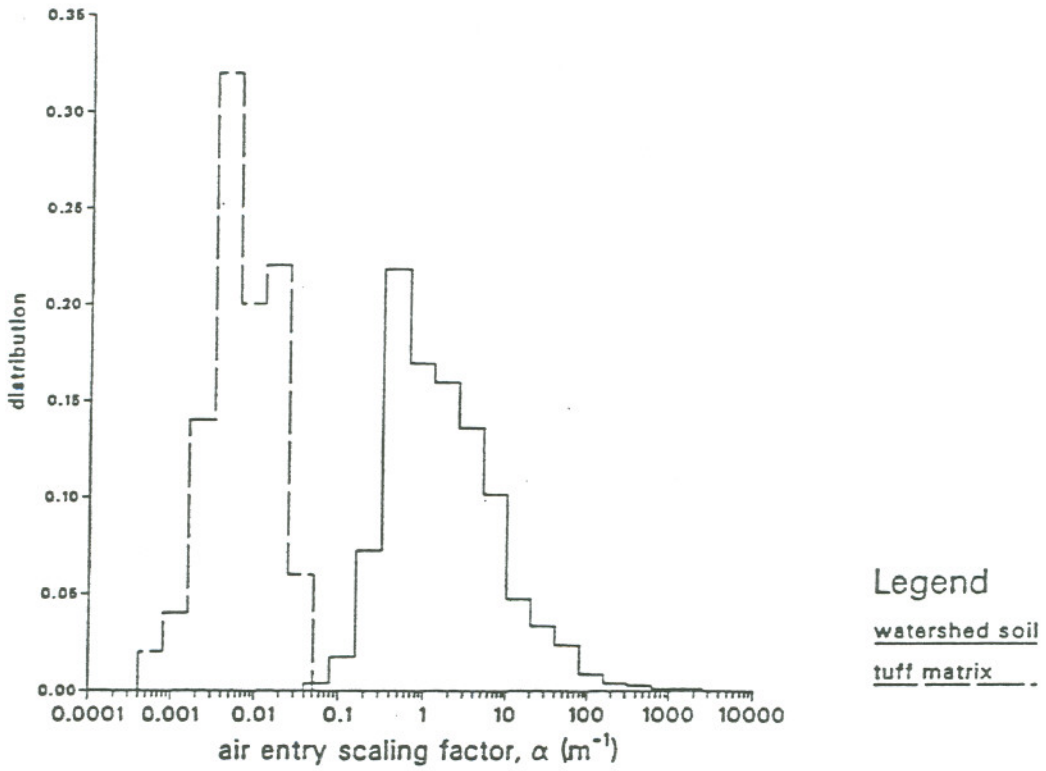

Figure 6.2 Distribution of air-entry scaling factor for natural soils and tuff matrix.

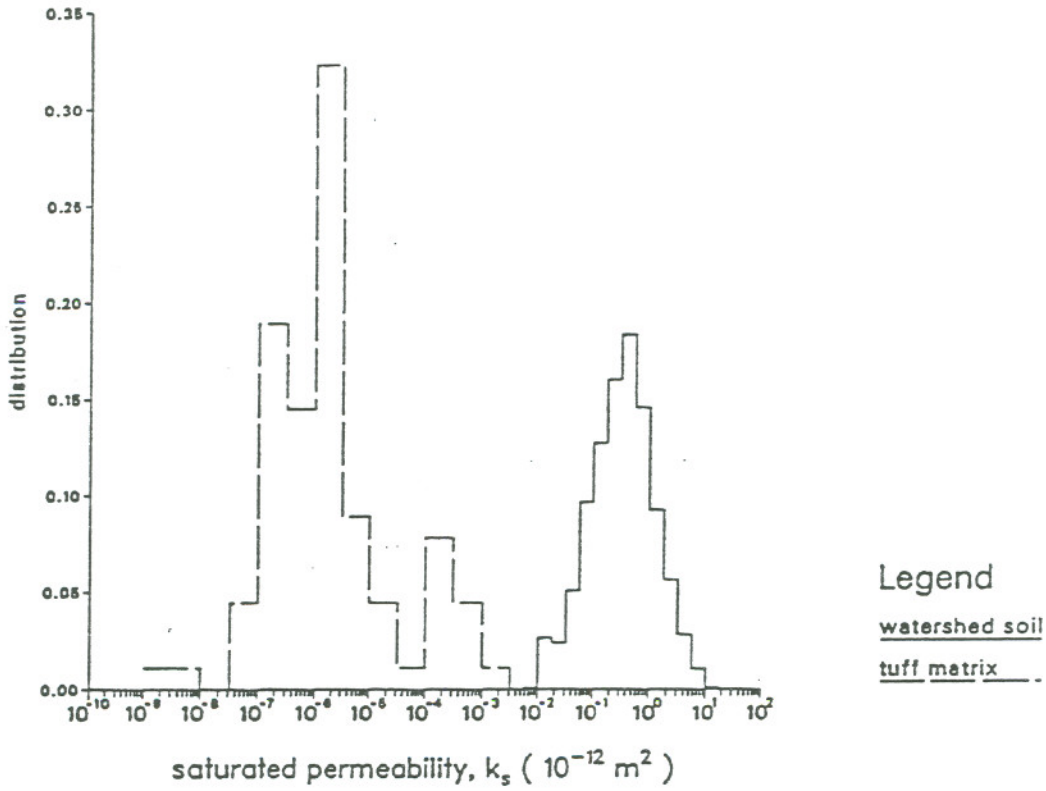

Figure 6.3 Distribution of saturated hydraulic conductivity for natural soils and tuff matrix.

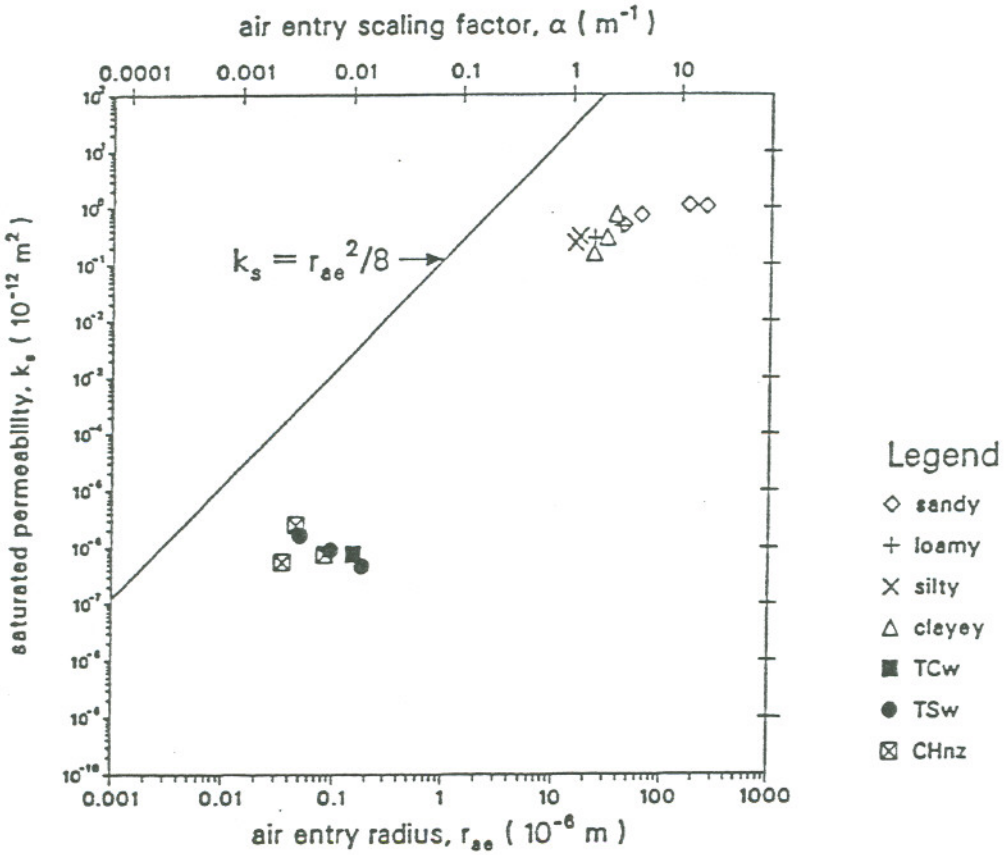

Figure 6.4 Correlation between saturated hydraulic conductivity and air-entry scaling factor for natural soils and tuff matrix.

magnitude among different geological media. The porosity varies over a much narrower range among different geological media. With wider variations, the air entry radius may correlate better with saturated permeability, which has the widest range of variation among all hydrological parameters.

6.3 Fracture and Fault Parameters: *Physical Constraint*

We need hydrologic data for the fractures and faults. There are only a few measurements on saturated permeability of fractured cores (Peters *et al.*, 1984) and none on unsaturated characteristic curves of fractures. Only theoretical models have been derived or assumed to represent the fracture and fault characteristic curves. Wang and Narasimhan (1985) derived the fracture curves in terms of measurable bulk conductivity, fracture orientations and spacings, and fractions of fracture coatings. Peters *et al.* (1984) assumed that the fractures behave like permeable sand. Rulon *et al.* (1986) used a parallel channel model (Harrold *et al.*, 1985) to derive anisotropic fracture- and fault characteristic curves. Fig. 6.5 compares the model parameters in the correlation cross plot of saturated permeability and air entry radius. Clearly the model parameters are very scattered and some of the models have saturated permeability greater than the maximum capillary tube value $r_{ae}^2/8$.

Even though theoretical models can be derived for fractures and faults, we need to have experimental measurements to validate the theoretical models. The contrast of hydrological parameters between fractures and tuff matrix in meter scale determines if the fluid flow is fast through fractures or slow through matrix under ambient partially saturated conditions. The contrast of hydrological parameters between stratigraphic units and bounding faults in kilometer scale determines if the net infiltration is dispersed through the unsaturated tuff formations or concentrated through a few major faults from ground surface to water table. The lack of data in fractures and faults is one of the reasons we survey the soil data and study the parameter variations and correlations among different natural geological media. If constraints and correlations can be shown to govern and scale among different geological media, we can evaluate whether the theoretical model parameters are reasonable and physical and establish better confidence in our calculation results.

If correlation between saturated permeability and air entry radius is important, we need to take this correlation into account. For stochastic modeling of alternating units of welded and nonwelded tuff or formation blocks bounded by fault zones, we propose to impose correlations and constraints on average values of saturated permeability and air entry scaling factor between highly different units to avoid unlikely combinations of

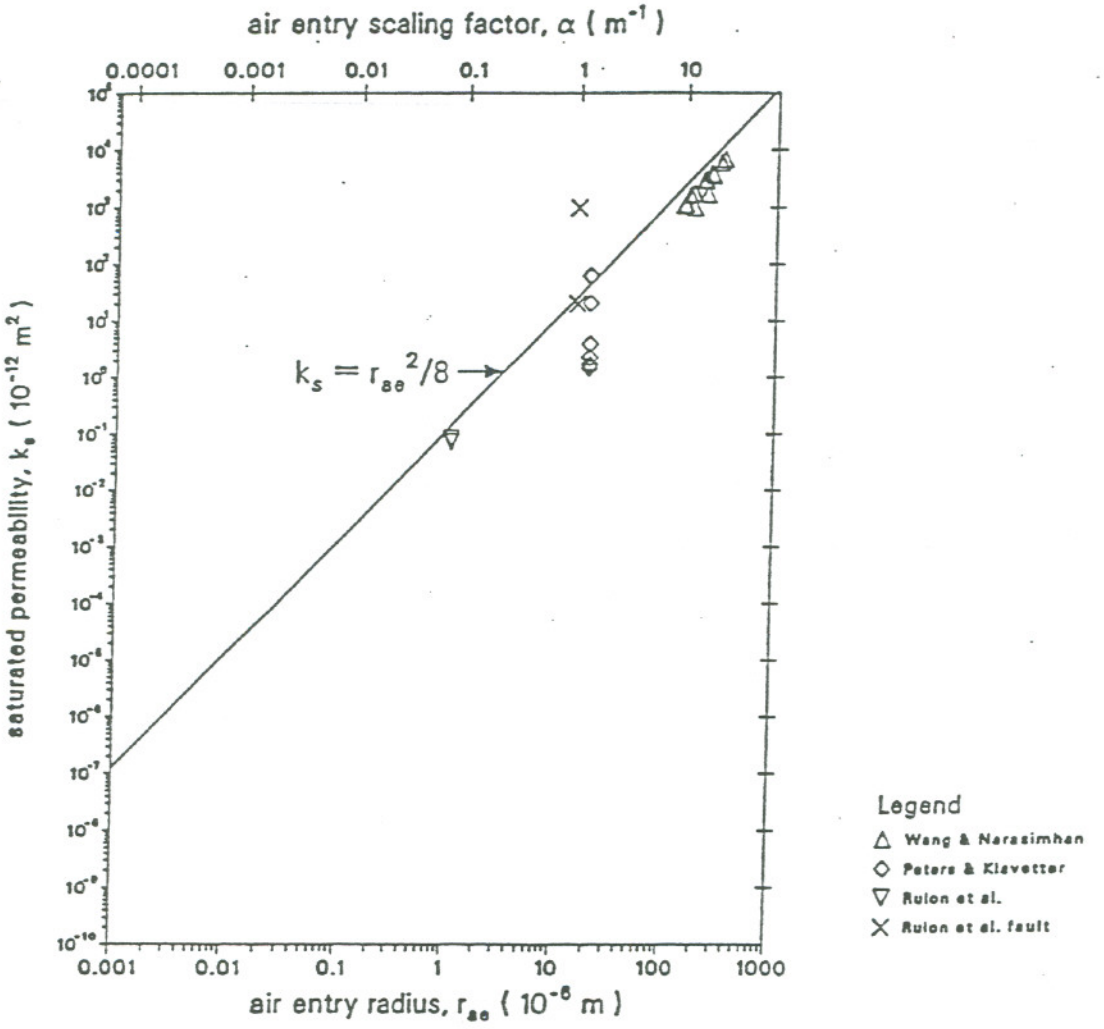

Figure 6.5 Correlation between saturated hydraulic conductivity and air-entry scaling factor for tuff fracture and fault models.

parameters and predictions. Within a given stratigraphic unit, this physically meaningful correlation is likely to be masked by data variablilty, and uncorrelated parameters with wide distributions may be acceptable.

6.4 Fractal Theory: *Spatial Correlation and Scaling of Rough-Walled Fractures*

With parameter distributions and correlations determined from laboratory measurements, we need additional information on spatial correlation and scale dependance to properly model field-scale hydrological processes. The spatial correlation structure determines the grid block sizes to represent a heterogeneous formation and the scaling law relates the laboratory measurements to field experiments. We have constructed a fractal fracture model (Wang *et al.*, 1988) to represent a rough-walled fracture. From that particular model study, we also recognize that the fractal scaling approach can be used for other parameters. Even more important is the realization that fractal scaling is more general than traditional geostatistical analyses with empirical variograms for representation of spatial correlation.

A very useful and interesting aspect of the fractal is its scaling behavior. A rough profile measured with a low-resolution measuring device over a large distance may be geometrically similiar to the profile measured with a high-resolution device over a much smaller scale on the same rock sample. If this scaling property can indeed be demonstrated, we can deduce structure information at small scales by measuring at large scales, and vice versa. The fractal dimension D can be regarded as a scaling parameter. Fig. 6.6 illustrates the steps in a recursive subdivision algorithm (Fournier *et al.*, 1982; Brown, 1987) to generate a fractal surface. The procedure starts with a 3 by 3 mesh with zero z values on the mesh points to define a reference flat surface. In the second level with a 5 by 5 mesh, the z value of a new point is computed by a Gaussian random variable function, with the expected value determined by its four known neighbors (two on the boundaries) of the 3 by 3 mesh, and the standard deviation scaled by the fractal dimension D and distance to the neighbors. We can continue the generation procedure level by level to finer mesh. A low-D surface will have the standard deviation scaled down faster than a high-D surface as one proceeds from one level to another level to fill the mesh (Fig. 6.7).

We can use a similiar procedure to generate representations of heterogeneous media with spatially varying and correlated parameters. We simply replace the elevations by the property values and the Gaussian distribution by the parameter distribution. If data values are known at a given number of locations, we can start with these locations as the first-level mesh points and generate refinements in accordance to the parameter

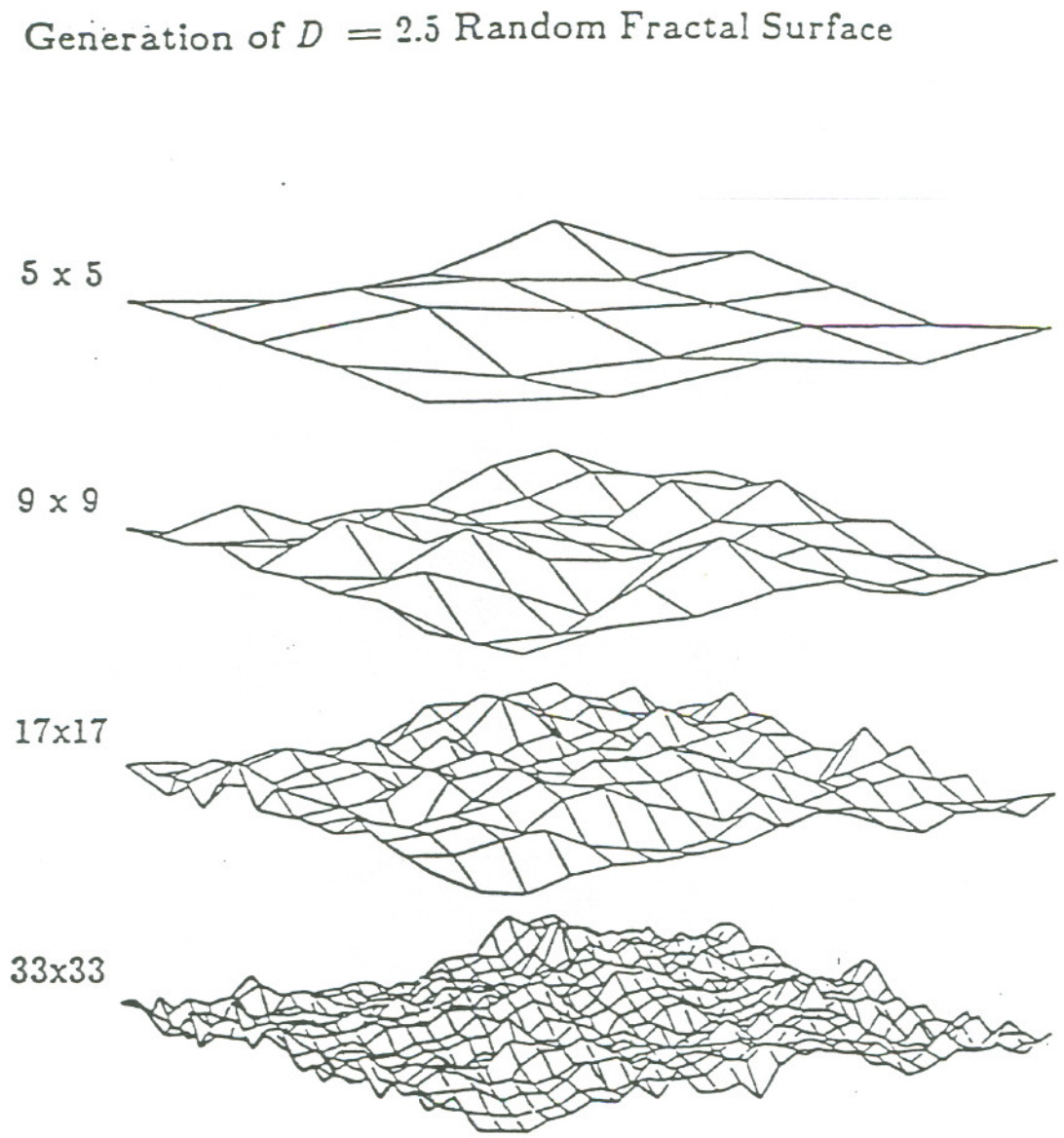

Figure 6.6 Steps involved in generating a rough fracture with fractal dimensions.

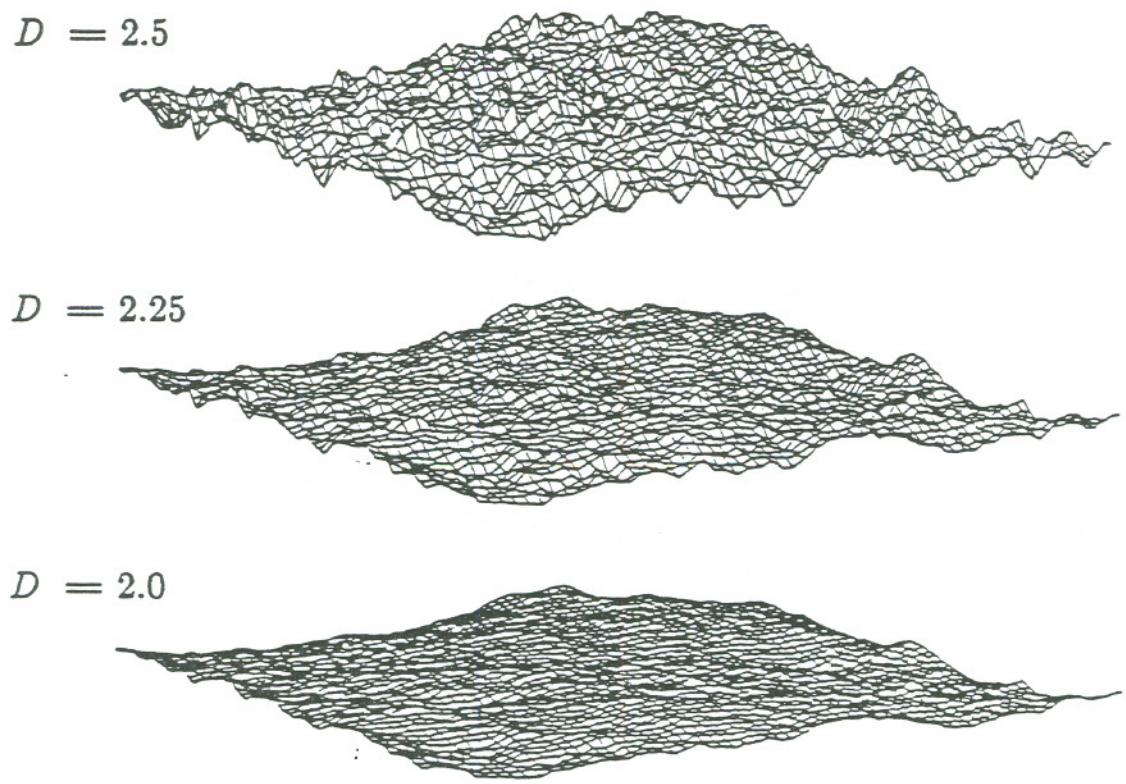

Figure 6.7 Representation of rough fractures with fractal surfaces.

distribution and spatial correlation structure. The heterogeneous field generated by this procedure will take into account the spatial correlation because the mean value at a mesh point is determined by the values of its neighbors. Because the generation of each sub-domain use the same procedure for the larger domain, domains of different sizes are scaled. We can have a low-level or low-resolution mesh to first model the field approximately and continue upgrading the results with meshes of higher-level refinements.

The fractal dimension D can be determined by log-log type curve analyses from variogram data of the parameter distribution. The log-log slope near the origin of zero spatial separation is equal to $6 - 2D$, as shown in Fig. 6.8 from a derivation for the fractal fracture model (Wang *et al.*, 1988). The spherical model and many other empirical variogram models widely used in geostatistical analyses have a log-log slope of 1. If we reanalyze many variogram data in a log-log plot instead of linear plot, we can deduce the fractal dimension and use the fractal dimension as a scaling parameter to generate geostatistical representations.

If a heterogeneous field is generated with parameter distribution, correlation, and scaling properly taken into account, we can then proceed to solve flow equations to obtain the distributions in pressure, flux, and velocity field. We need to quantify uncertainties to obtain groundwater travel time distributions. We are still perfecting our approaches and models so that the groundwater travel time calculations can be efficiently and accurately calculated.

7.0 Review and Summary

From analysis of capillarity-based conceptual model (Sec. 2 and 3, Wang and Narasimhan, 1984, 1985), fractures can be desaturated more easily than the matrix if fracture apertures are larger than matrix pore sizes. With fractures drained, liquid water could flow from one matrix block to another across contact areas. Reda (1987) and Eaton and Bixler (1987) measured and analyzed the imbibition of liquid water into a tuff core which contained several microfractures transversely oriented to the direction of the wetting-front propagation. The local minima in saturation were shown to occur near the fractures. A fracture could also impede liquid front movement, whereas vapor-phase transport might occur across a fracture. The dominance of matrix flow was illustrated by the following two tests. Haldeman *et al.* (1991) showed that the wetting front moved mainly through the unsaturated matrix, and not much through the vertical fracture when liquid water under suction was applied to the top of a fractured tuff block from Apache Leap, Arizona. Gvirtzman *et al.* (1988) examined the partitioning of downward

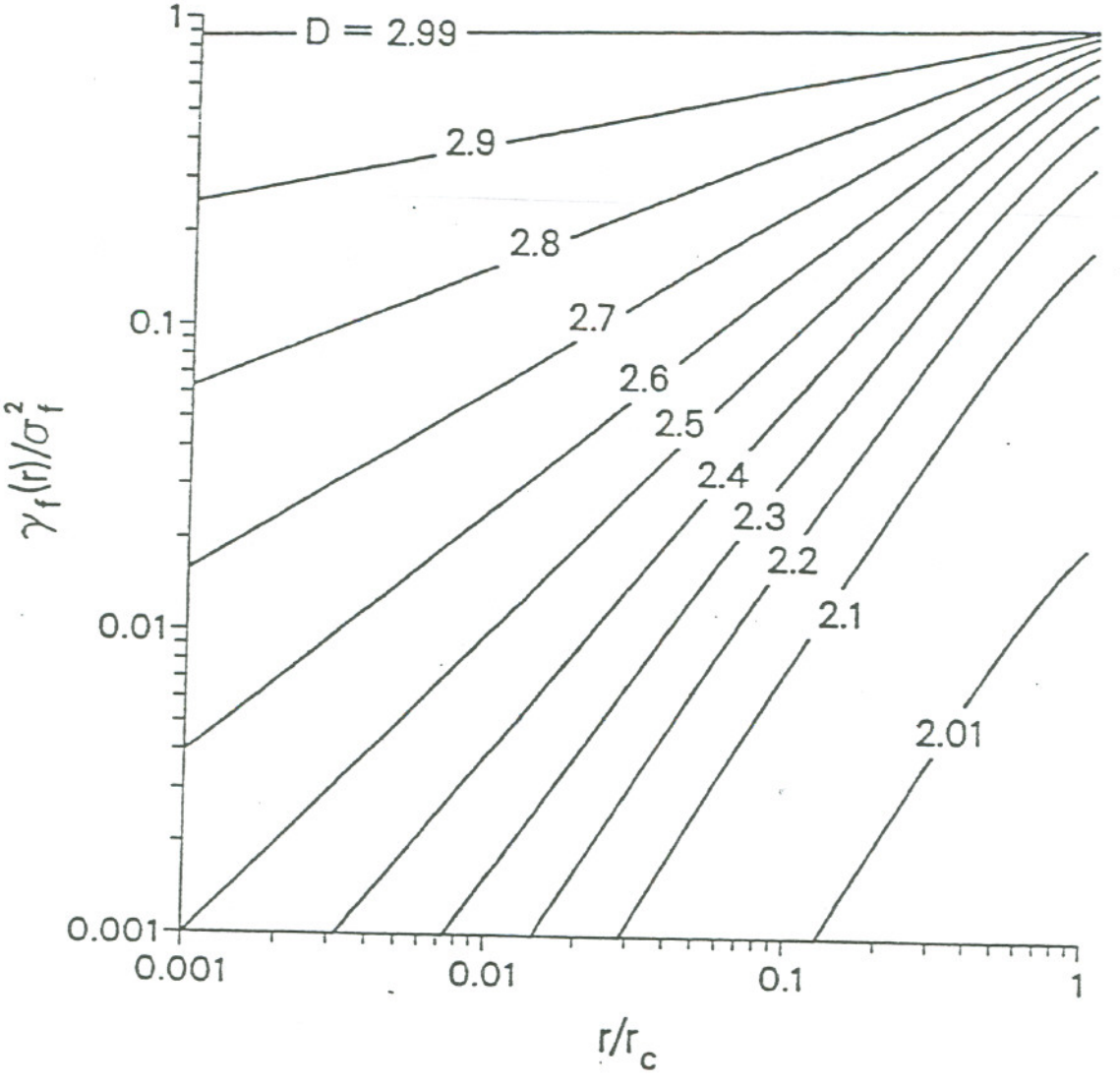

XBL 8711-4652

Figure 6.8 Relation between variograms and fractal dimensions.

percolation between slow bulk flow through the matrix and fast flow through the fractures in calcareous sandstone, using environmental tritium as a natural tracer.

Pruess and Tsang (1990) studied the fracture flow for both the liquid phase and the gas phase and showed that the interference between fluid phases flowing in a fracture was strong, with the nonwetting phase flow easily choked off when the wetting phase occupied small aperture regions. Fracture flow can be important when the fracture is in nearly-saturated conditions. If water ponding occurs at the ground surface at the entrance of a vertical fracture, thus guaranteeing a continuous slug of water along the fracture, the wetting front along the fracture may be ahead of that in the matrix (Nitao and Buscheck, 1989). Capillary hysteresis in the matrix may also enhance vertical fracture flow penetration (Niemi and Bodvarsson, 1988). If the supply of water is finite, as in the case of cyclic infiltration pulses (Sec. 4, Wang and Narasimhan, 1986, 1990), the water entering the fractures may easily imbibe into the matrix. When a fracture is filled with water, the capillary force will draw water into the unsaturated matrix blocks. Zimmerman *et al.* (1990) showed that the rate of absorption into the matrix is proportional to the ratio of surface area to volume for irregularly shaped blocks. The presence of a low-permeability skin at the fracture-matrix interface might delay, but not entirely eliminate, the absorption of water into the matrix blocks (Pruess and Wang, 1987).

Composite-porosity models, effective medium models and multiple interacting continua methods were used in recent field-scale simulation studies to assess the impact of siting a high-level nuclear waste repository at Yucca Mountain. Sinnock *et al.* (1987) estimated the release rate of radionuclides from the potential repository with a multiple-column unit-gradient stochastic model. Kaplan *et al.* (1989) illustrated the sensitivity of groundwater travel time calculations on particle tracking or conservative tracer concentration criteria. Bloomsburg et al. (1989) demonstrated the need to include multi-dimensional analyses for heterogeneous unsaturated systems. The concern for lateral flows and fault flows (Rulon *et al.*, 1986; Montazer and Wilson, 1984) motivated the two-dimensional modeling studies by Prindle (1989) and Wang and Narasimhan (1988, 1990) (Sec. 5). Multi-dimensional modeling results are sensitive to the boundary conditions and to the constrast in hydrological parameters of fault and tuff units. In addition to liquid flow, gas flow can be significant in unsaturated, fractured media. Weeks (1987) and Kipp (1987) measured and modeled the seasonal variation of high-rate air flows in boreholes at the crest of the mountain. Tsang and Pruess (1987) estimated that the buoyancy-driven gas phase convection velocity is orders of magnitude larger than the liquid velocity.

Statistical, geostatistical, and fractal analyses (Sec. 6, Wang *et al.*, 1988; Wang and Narasimhan, 1989) will be needed to characterize the fractured, tuff formations and to scale the hydrological parameters. As site characterization activities at Yucca Mountain (DOE, 1989) proceed, the uncertainties about the ambient conditions will be better quantified and models for performance assessment will be better calibrated and validated. In addition to ambient conditions, we need to understand the long term evolution of the system to make the long term predictions more creditable. This chapter mainly addresses the conceptual analysis of the nature of unsaturated flow regime in a fractured, porous tuff system. For the assessment of the unsaturated repository concept, we need to account for the contact of flow with waste packages and the migration and retardation of radionuclides (Fig. 7.1). The amenability to long term monitoring and the retrievability of the wastes for a repository in the unsaturated zone are also important components in finding a rational solution to this challenging problem. These general issues are addressed by Narasimhan and Wang (1991) with a hierarchy approach to identify the hydrological issues that need resolution to support the performance assessment of Yucca Mountain.

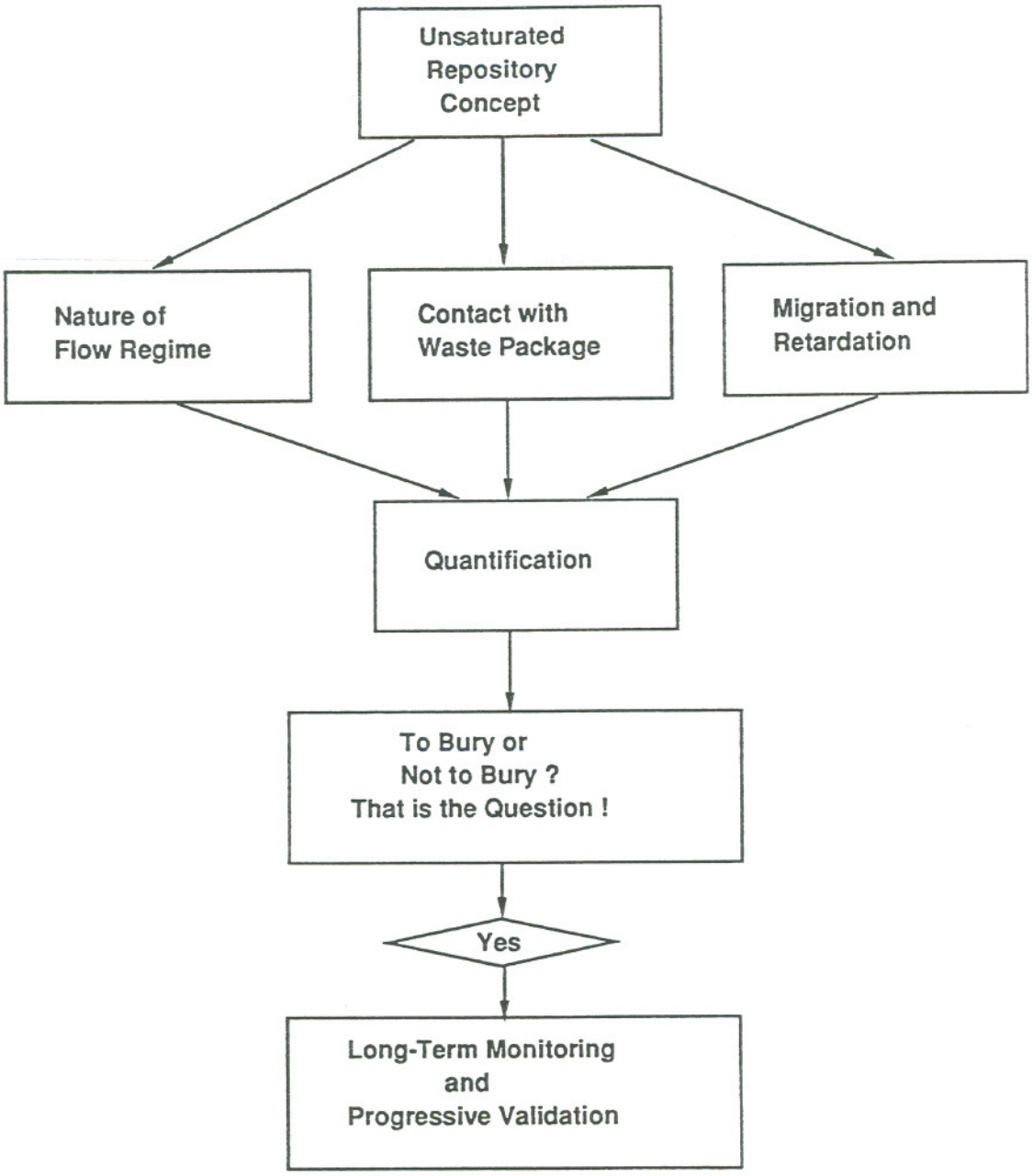

Figure 7.1 Framework of fundamental questions in performance assessment.

Acknowledgments

We would like to thank Scott Sinnock, Tom Lin, and Paul Kaplan of Sandia National Laboratories for continued discussions and review throughout the course of this study. Interactions with our colleagues Karsten Pruess, Yvonne Tsang, and Chin Fu Tsang helped greatly in developing our models. The work was supported by the Sandia National Laboratories for the Yucca Mountain Site Characterization Project of the U.S. Department of Energy under contract DE-AC03-76SF00098.

References

Bauer, S. J., Preliminary Report on Yucca Mountain Fracture Characteristics, Memorandum to J. R. Tillerson dated March 27, 1986, Appendix D, Attachment 1 of the Site Characterization Plan Conceptual Design Report, SAND84-2641, compiled by H. R. MacDougall, L. W. Scully and J. R. Tillerson, Sandia National Laboratories, Albuquerque, NM, 1986.

Bloomsburg, G., R. E. Williams, and J. L. Osiensky, Distribution of Downward Flux in Unsaturated Heterogeneous Hydrogeology Environments, *Geol. Soc. Am. Bull.*, 101, 1623–1630, 1989.

Brooks, R. H. and A. T. Corey, Properties of Porous Media Affecting Fluid Flow, *J. Irrigation and Drainage Div., Proc. Am. Soc. Civ. Eng.*, 92, IR2, 61–88, 1966.

Brown, S. R., Fluid Flow Through Rock Joints: the Effect of Surface Roughness, *J. Geophys. Res.*, 92, 1337–1347, 1987.

DOE, Site Characterization Plan Public Handbook, DOE/RW-0206, Office of Civilian Radioactive Waste Management Program, U. S. Department of Energy, Washington, DC, 1989.

Eaton, R. R., and N. E. Bixler, Analysis of a Multiphase, Porous-Flow Imbibition Experiment in Fractured Volcanic Tuff, in *Flow and Transport through Unsaturated Fractured Rock*, Geophysical Monograph 42, American Geophysical Union, edited by D. D. Evans and T. J. Nicholson, 91–97, 1987.

Evans, D. D., and C. H. Huang, Role of Desaturation on Transport through Fractured Rock, *Role of the Unsaturated Zone in Radioactive and Hazardous Waste Disposal,* edited by J. Mercer, P. S. Rao and I. W. Marine, Ann Arbor Science Publisher, Ann Arbor, MI, pp. 165–178, 1983.

Fournier, A., D. Fussell and L. Carpenter, Computer Rendering of Stochastic Models, *Comm. Asso. Computing Machinery,* 25, 371–384, 1982.

Gentier, S., Morphologie et Comportement Hydromecanique d'une Fracture Naturalle dans un Granite Sours Contrainte Normale, Doctoral Thesis, Univ. d'Orl'eans, France, 1986.

Gvirtzman, H., M. Magaritz, Y. Kanfi, and I. Carmi, Matrix and Fissure Water Movement through Unsaturated Calcareous Sandstone, *Transport in Porous Media,* 3, 343–356, 1988.

Haldeman, W. R., Y. Chuang, T. C. Rasmussen, and D. D. Evans, Laboratory Analysis of Fluid Flow and Solute Transport through a Fracture Imbedded in Porous Tuff, *Water Resour. Res.*, 27(1), 53–66, 1991.

Harrold, P., C. C. Barton and P. Montazer, Statistical Analysis of Fracture Roughness Profiles in Volcanic Tuffs, Yucca Mountain, Nevada, *EOS, Trans. Amer. Geophys. Union,* 66 (46), p. 883, 1985.

Holtan, H. N., C. B. England, G. P. Lawless and G. A. Schumaker, Moisture-Tension Data for Selected Soils on Experimental Watersheds, ARS 41-144, Agricultural Research Service, U. S. Department of Agriculture, Beltsville, MD, 609 p, 1968.

Kaplan, P., E. Klavetter, and R. Peters, Approaches to Groundwater Travel Time, *Proc. Waste Manag. '89,* Tucson, AZ, edited by R. G. Post, v. I, pp. 493–495, 1989.

Kipp, K. L., Jr., Effect of Topography on Gas Flow in Unsaturated Fractured Rock: Numerical Simulation, in *Flow and Transport through Unsaturated Fractured Rock*, Geophysical Monograph 42, American Geophysical Union, edited by D. D. Evans and T. J. Nicholson, 171–176, 1987.

Klavetter, E. A. and R. R. Peters, An Evaluation of the Use of Mercury Porosimetry in Calculating Hydrologic Properties of Tuffs from Yucca Mountain, Nevada, SAND86-0286, Sandia National Laboratories, Albuquerque, NM, 1987.

Montazer, P. and W. E. Wilson, Conceptual Hydrologic Model of Flow in the Unsaturated Zone, Yucca Mountain, Nevada, USGS-WRI-84-4345, U. S. Geological Survey, Lakewood, CO, 55 p., 1984.

Narasimhan, T. N., Geometry-Imbedded Darcy's Law and Transient Subsurface Flow, *Water Resour. Res.*, 21, 1285–1292, 1985.

Narasimhan, T. N., and J. S. Y. Wang, Conceptual, Experimental and Computational Approaches to Support Performance Assessment of Hydrology and Chemical Transport at Yucca Mountain, SAND89-7018, Sandia National Laboratories, Albuquerque, NM, LBL-28613, Lawrence Berkeley Laboratory, Berkeley, CA, 1991.

Narasimhan, T. N., and P. A. Witherspoon, An Integrated Finite Difference Method for Analyzing Fluid Flow in Porous Media, *Water Resour. Res.,* 12, 57-64, 1976.

Narasimhan, T. N., P. A. Witherspoon and A. L. Edwards, Numerical Model for Saturated-Unsaturated Flow in Deformable Media, 2. The Algorithm, *Water Resour. Res.,* 14, 255–261, 1978.

Niemi, A., and G. S. Bodvarsson, Preliminary Capillary Hysteresis Simulations in Fractured Rocks, Yucca Mountain, Nevada, *J. Contaminant Hydro.,* 3, 277–291, 1988.

Nimick, F. B., S. J. Bauer and J. R. Tillerson, Recommended Matrix and Rock-Matrix Bulk, Mechanical and Thermal Properties for Thermomechanical Stratigraphy of Yucca Mountain, Appendix O of the Site Characterization Plan - Conceptual Design Report, SAND84-2641, compiled by H. R. MacDougall, L. W. Scully, and J. R. Tillerson, Sandia National Laboratories, Albuquerque, NM, 1984.

Nitao, J. J., and T. A. Buscheck, On the Infiltration of a Liquid Front in an Unsaturated, fractured porous medium, *Proc. Nuc. Waste Iso. Unsat. Zone, Focus '89,* Am. Nuc. Soc., pp. 381–397, 1989.

Ortiz, T. S., R. L. Williams, F. B. Nimick, B. C. Whittet and D. L. South, A Three-Dimensional Model of Reference Thermal/Mechanical and Hydrological Stratigraphy at Yucca Mountain, Southern Nevada, SAND84-1076, Sandia National Laboratories, Albuquerque, NM, 1984.

Panian, T. F., Unsaturated Flow Properties Data Catalog, Volume II, DOE/NV/10384-20, Desert Research Institute, University of Nevada, 493 p., 1987.

Peters, R. R. and E. A. Klavetter, A Continuum Model for Water Movement in an Unsaturated Fractured Rock Mass, *Water Resour. Res.,* 24, 416–430, 1988.

Peters, R. R., E. A. Klavetter, I. J. Hall, S. C. Blair, P. R. Heller and G. W. Gee, Fracture and Matrix Hydrologic Characteristics of Tuffaceous Materials from Yucca Mountain, Nye County, Nevada, SAND84-1471, Sandia National Laboratories, Albuquerque, NM, 188 p., 1984.

Peters, R. R., E. A. Klavetter, J. T. George and J. H. Gauthier, Measuring and Modeling Water Imbibition into Tuff, *Proc. Symp. Flow and Transport through Unsaturated Fractured Rock,* Geophysical Monograph 42, Am. Geophys. Union, edited by D. D. Evans and T. J. Nicholson, pp. 99–106, 1987.

Prindle, R. W., On a Sensitivity Analysis of Flow through Layered, Fractured Tuff: Implications for Performance Allocation and Performance-Assessment Modeling, *Proc. Nuc. Waste Iso. Unsat. Zone, Focus '89,* Am. Nuc. Soc., pp. 294-300, 1989.

Pruess, K. and T. N. Narasimhan, A Practical Method for Modeling Fluid and Heat Flow in Fractured Porous Media, *Soc. Pet. Eng. J.,* 25, 14–26, 1985.

Pruess, K., and Y. W. Tsang, On Two-Phase Relative Permeability and Capillary Pressure of Rough-Walled Rock Fractures, *Water Resour. Res.,* 26(9), 1915–1926, 1990.

Pruess, K., and J. S. Y. Wang, Numerical Modeling of Isothermal and Non-Isothermal Flow in Unsaturated Fractured Rock - a Review, in *Flow and Transport through Unsaturated Fractured Rock*, Geophysical Monograph 42, American Geophysical

Union, edited by D. D. Evans and T. J. Nicholson, 11–21, 1987.

Pruess, K., J. S. Y. Wang, and Y. W. Tsang, On Thermohydrological Conditions Near High-Level Nuclear Wastes Emplaced in Partially Saturated Fractured Tuff, 2. Effective Continuum Approximation, *Water Resour. Res.*, 26(6), 1249–1261, 1990.

Pruess, K., Y. W. Tsang and J. S. Y. Wang, Modeling of Strongly Heat-Driven Flow in Partially Saturated Fractured Porous Media, *Proc. Hydrogeology of Rocks of Low Permeability, Memoires 17*, Int. Asso. Hydrogeologists, pp. 486–497, 1985.

Reda, D. C., Influence of Transverse Microfractures on the Imbibition of Water into Initially Dry Tuffaceous Rock, in *Flow and Transport through Unsaturated Fractured Rock*, Geophysical Monograph 42, American Geophysical Union, edited by D. D. Evans and T. J. Nicholson, 83–90, 1987.

Roseboom Jr., E. H., Disposal of High-Level Nuclear Waste Above the Water Table in Arid Regions, Circular Number 903, U. S. Geological Survey, 1983.

Rulon, J., G. S. Bodvarsson and P. Montazer, Preliminary Numerical Simulations of Groundwater Flow in the Unsaturated Zone, Yucca Mountain, Nevada, LBL-20553, Lawrence Berkeley Laboratory, Berkeley, CA, 91 p., 1986.

Scott, R. B. and J. Bonk, Preliminary Geologic Map of Yucca Mountain, Nye County, Nevada, with Geologic Sections, USGS-OFR-84-494, U. S. Geological Survey, Denver, CO., 1984.

Scott, R. B., R. W. Spengler, S. Diehl, A. R. Lappin and M. P. Chornack, Geologic Character of Tuffs in the Unsaturated Zone at Yucca Mountain, Southern Nevada, in *Role of the Unsaturated Zone in Radioactive and Hazardous Waste Disposal,* edited by J. Mercer, P. S. Rao and I. W. Marine, Ann Arbor Science Publisher, Ann Arbor, MI, pp. 289–335, 1983.

SNL, The Nevada Nuclear Waste Storage Investigations Project Reference Information Base, Sandia National Laboratories, Albuquerque, NM, 1986.

Sinnock, S., Y. T. Lin, and J. P. Brannen, Preliminary Bounds on the Expected Postclosure Performance of the Yucca Mountain Repository Site, Southern Nevada, SAND84-1492, Sandia National Laboratories, Albuqueque, NM, *J. Geophys. Res.*, 92(B8), 7820–7842, 1987.

Spengler, R. W. and M. P. Chornack, Stratigraphic and Structural Characteristics of Volcanic Rocks in Core Hole USW-G4, Yucca Mountain, Nye County, Nevada, with a Section of Geophysical Logs by D. C. Muller and J. E. Kibler, USGS-OFR-84-789, U. S. Geological Survey, Denver, CO, 1984.

Thordarson, W., Geohydrologic Data and Test Results from Well J-13, Nevada Test Site, Nye County, Nevada, USGS-WRI-83-4171, U. S. Geological Survey, Denver, CO, 1983.

Travis, B. J., S. W. Hodson, H. E. Nuttall, T. L. Cook and R. S. Rundberg, Numerical Simulation of Flow and Transport in Fractured Tuff, *Proc. Scientific Basis for Nuclear Waste Management VII,* Mat. Res. Soc. Sym. Proc., 26, 1039–1046, 1984.

Tsang, Y. W., The Effect of Tortuosity on Fluid Flow Through a Single Fracture, *Water Resour. Res.,* 20, 1209–1215, 1984.

Tsang, Y. W., and K. Pruess, A Study of Thermally Induced Convection Near a High-Level Nuclear Waste Repository in Partially Saturated Fractured Tuff, *Water Resour. Res.,* 23(10), 1958–1966, 1987.

van Genuchten, M. Th., A Closed-Form Equation for Predicting Hydraulic Conductivity of Unsaturated Soils, *Soil Sci. Soc. Am. J.,* 44, 892–898, 1980.

Wang, J. S. Y., and T. N. Narasimhan, Fluid Flow in Partially Saturated, Welded-Nonwelded Tuff Units, *Geoderma,* 46(1-3), 155–168, 1990.

Wang, J. S. Y. and T. N. Narasimhan, Processes, Mechanisms, Parameters, and Modeling Approaches for Partially Saturated Flow in Soil and Rock Media, SAND88-7054, Sandia National Laboratories, Albuquerque, NM, LBL-26224, Lawrence Berkeley Laboratory, Berkeley, CA, 305 p., 1989.

Wang, J. S. Y. and T. N. Narasimhan, Hydrologic Modeling of Vertical and Lateral Movement of Partially Saturated Fluid Flow near a Fault Zone at Yucca Mountain, SAND87-7070, Sandia National Laboratories, Albuquerque, NM, LBL-23510, Lawrence Berkeley Laboratory, Berkeley, CA, 122 p., 1988.

Wang, J. S. Y. and T. N. Narasimhan, Hydrologic Mechanisms Governing Partially Saturated Fluid Flow in Fractured Welded Units and Porous Non-welded Units at Yucca Mountain, SAND85-7114, Sandia National Laboratories, Albuquerque, NM, LBL-21022, Lawrence Berkeley Laboratory, Berkeley, CA, 126 p., 1986.

Wang, J. S. Y. and T. N. Narasimhan, Hydrologic Mechanisms Governing Fluid Flow in a Partially Saturated, Fractured, Porous Tuff at Yucca Mountain, *Water Resour. Res.,* 21, 1861–1874, 1985.

Wang, J. S. Y. and T. N. Narasimhan, Hydrologic Mechanisms Governing Fluid Flow in a Partially Saturated, Fractured, Porous Tuff at Yucca Mountain, SAND84-7202, Sandia National Laboratories, Albuquerque, NM, LBL-18473, Lawrence Berkeley Laboratory, Berkeley, CA, 1984.

Wang, J. S. Y., T. N. Narasimhan and C. H. Scholz, Aperture Correlation of a Fractal Fracture, *J. Geophys. Res.* 93, 2216–2224, 1988.

Weeks, E. P., Effect of Topography on Gas Flow in Unsaturated Fractured Rock: Concepts and Observations, in *Flow and Transport through Unsaturated Fractured Rock*, Geophysical Monograph 42, American Geophysical Union, edited by D. D. Evans and T. J. Nicholson, 165–170, 1987.

Winograd, I. J., Radioactive Waste Disposal in Thick Unsaturated Zones, *Science,* 212 (4502), 1457–1464, 1981.

Zimmerman, R. W., G. S. Bodvarsson, and E. M. Kwicklis, Adsorption of Water into Porous Blocks of Various Shapes and Sizes, *Water Resour. Res.,* 26(11), 2797–2806, 1990.